

Space engineering

Space environment



Published by: ESA Publications Division

ESTEC, P.O. Box 299, 2200 AG Noordwijk, The Netherlands

ISSN: 1028-396X

Price: € 30

Printed in The Netherlands

Copyright 2000 $\ensuremath{^{\odot}}$ by the European Space Agency for the members of ECSS



Foreword

This Standard is one of the series of ECSS Standards intended to be applied together for the management, engineering and product assurance in space projects and applications. ECSS is a cooperative effort of the European Space Agency, national space agencies and European industry associations for the purpose of developing and maintaining common standards.

Requirements in this Standard are defined in terms of what shall be accomplished, rather than in terms of how to organize and perform the necessary work. This allows existing organizational structures and methods to be applied where they are effective, and for the structures and methods to evolve as necessary without rewriting the standards.

The formulation of this Standard takes into account the existing ISO 9000 family of documents.

This Standard has been prepared by the ECSS Working Group on ECSS-E-10-04 Space Environment Standard, reviewed by the ECSS Technical Panel and approved by the ECSS Steering Board.



(This page is intentionally left blank)



Introduction

This Standard is of level 3 in the ECSS hierarchy. It forms part of the System engineering branch (ECSS-E-10) of the Engineering area of the ECSS system (ECSS-E). As such it is intended to assist in the consistent application of space environment engineering to space products through specification of required or recommended methods, data and models to the problem of ensuring best performance, problem-avoidance or survivability of a product in the space environment.

The space environment can cause severe problems for space systems. Proper assessment of the potential effects is part of the system engineering process as defined in ECSS-E-10. This is performed in the early phases of a mission when consideration is given to e.g. orbit selection, mass budget, thermal protection, and component selection policy. As the design of a space system is developed, further engineering iteration is normally necessary with more detailed analysis.

In this Standard, each component of the space environment is treated separately, although synergies and cross-linking of models are specified. Extensive informative annexes are provided as explanatory background information associated with each clause.



 $(This\ page\ is\ intentionally\ left\ blank)$



Contents

For	eword	3
Intr	roduction	5
1	Scope	15
2	Normative references	17
3	Terms, definitions and abbreviated terms	19
3.1	Terms and definitions	19
3.2	Abbreviated terms	26
4	Gravitation	29
4.1	Introduction	29
4.2	Model presentation	32
4.3	Reference data	32
4.4	References	34
5	Geomagnetic fields	35
5.1	Introduction – Overview of the geomagnetic field and effects	35



5.2	Reference data on the geomagnetic field	36
5.3	Geomagnetic field models and analysis methods	36
5.4	Tailoring guidelines	41
5.5	Figures	42
5.6	References	43
6 Solai	and Earth electromagnetic radiation and indices	45
6.1	Introduction	45
6.2	Solar electromagnetic radiation	46
6.3	Earth electromagnetic radiation	47
6.4	Solar and geomagnetic indices	47
6.5	Figures	52
6.6	References	53
7 The	neutral Earth atmosphere	55
7.1	Introduction	55
7.2	Recommended reference model	55
7.3	Structure of the Earth atmosphere	55
7.4	Atmospheric state parameters	56
7.5	Temperature, composition, and density model of the Earth heterosphere .	57
7.6	Temperature, composition, and density model of the Earth homosphere	66
7.7	Reference model output	67
7.8	Wind model of the Earth homosphere and heterosphere	67
7.9	Simple density models of planetary atmospheres	68
7.10	Aerodynamics in the Earth atmosphere	69
7.11	Figures	71
7.12	References	77
8 Plasr	nas	79
8.1	Introduction	79
8.2	The ionosphere	80
8.3	The plasmasphere	83
8.4	The outer magnetosphere	84
8.5	The solar wind	86
8.6	Induced environments	87
8.7	Tailoring guidelines	89
8.8	References	90



9 Ene	ergetic particle radiation	91
9.1	Introduction – Overview of energetic particle radiation environment and	01
9.2	effects	91 93
9.3	Energetic particle radiation environment reference data, models and	70
7.0	analysis methods	94
9.4	Analysis methods for derived quantities	101
9.5	Tailoring guidelines: Orbital and mission regimes	104
9.6	Preparation of a radiation environment specification	105
9.7	Figures	106
9.8	References	121
10 Par	ticulates	123
10.1	Introduction	123
10.2	Analysis techniques	124
10.3	Model presentation	125
10.4	Reference data	128
10.5	Figures	133
10.6	References	137
11 Co	ntamination	139
11.1	Introduction	139
11.2	Molecular contamination	140
11.3	Particulate contamination	141
11.4	Effect of contamination	142
11.5	Models	142
11.6	References	146
Annex	A (informative)	147
Annex	B (informative) Gravitation	149
B. 1	Related tools	149
B.2	Effects	149
B.3	Gravitational field at the surface of a planet	151
B.4	Uncertainties	152
B.5	References	153



Annex	C (informative) Geomagnetic field	155
C.1	Description of magnetosphere	155
C.2	Derivation of dipole strength from field model coefficients	155
C.3	Incompatibilities and inconsistencies	156
C.4	IGRF model details and availability	156
C.5	References	157
Annex	D (informative) Solar and Earth electromagnetic radiation and	
	indices	159
D.1	Solar spectrum details	159
D.2	Albedo and infrared variability	159
D.3	Activity indices information	160
D.4	Radio noise	160
D.5	Solar radiation pressure	160
D.6	Figures	161
D.7	References	165
Annex	E (informative) The neutral Earth atmosphere	167
E.1	Overview of atmosphere models	167
E.2	Accessibility of the MSISE-90 model	168
E.3	References	168
Annex	F (informative) Plasma	169
F.1	Surface charging	169
F.2	Charging in LEO	170
F.3	NASCAP charging code	171
F.4	POLAR charging code	172
F.5	Other charging codes	173
F.6	NASA worst case charging environment	173
F.7	Ram and wake effects	173
F.8	Current collection effects	174
F.9	Sputtering	174
F.10		175
F.11	Availability of the IR195 model	175
F.12	References	176



Annex G	(informative) Radiation	177
G.1	Links with radiation testing	177
G.2	Future models	178
G.3	Sources of models	179
G.4	Internal electrostatic charging analysis tools	179
G.5	Further information	180
G.6	References	180
Annex H	(informative) Particulates	181
H.1	Space debris flux models	181
H.2	Model uncertainties	183
H.3	Damage assessment	184
H.4	Analysis tools	185
H.5	Lunar dust simulant	186
H.6	References	186
Annex I (informative) Contamination	187
l.1	Existing Tools	187
1.2	ESABASE: OUTGASSING, PLUME-PLUMFLOW and CONTAMINE modules	187
1.3	JMC3D	188
1.4	CONTAM 3.2 or CONTAM III	189
1.5	TRICONTAM	190
1.6	SOCRATES	190
1.7	SPACE II	191
1.8	MOLFLUX	191
1.9	ISEM	192
I.10	OPT	192
I.11	CAP	192
I.12	Databases	192
1.13	References	193
Figures		
Figure 1:	Geomagnetic field strength at 400 km altitude based on IGRF-1995	42
Figure 2:	Output from geomagnetic field models showing the diurnal distortion to the field and seasonal variations in the distortion [RD5.8]	9 42
Figure 3:	Variation of the geomagnetic field as a function of altitude	43
Figure 4:	Standard predictions of solar and geomagnetic activity during a cycle	52
Figure 5:	Variation of the MSISE-90 mean temperature with altitude for extremely low activities, for mean activities and for extremely high activities	71



Variation of the MSISE-90 mean air density with altitude for low activities, for mean activities and for extremely high activities	71
Variation of the MSISE-90 mean atomic oxygen with altitude for extremely low activities, for mean activities and for extremely high activities	v 72
Variation of the MSISE-90 mean concentration profile of the atmosphere constituents N2, O, O2, He, Ar, H, and N with altitude for mean activities	72
Diurnal (a) and seasonal-latitudinal (b) variations of the MSISE-90 local temperature at altitude $h=400\ km$	73
Diurnal (a) and seasonal-latitudinal (b) variations of the MSISE-90 air density at altitude $h=400\ km$ for mean atmospheric conditions	74
Diurnal (a) and seasonal latitudinal (b) variations of the MSISE-90 atomic oxyg concentration at altitude $h=400\ km$ for mean atmospheric conditions	jen 75
Diurnal (a) and seasonal-latitudinal (b) variations of wind magnitude and direction according to HWM-93 at altitude $h=400\ km$ for mean atmospheric conditions	c 76
Mean ranges of protons and electrons in aluminium	106
Contour plots of the electron and proton radiation belts	107
Electron (a) and proton (b) omnidirectional fluxes, integral in energy, on the geomagnetic equator for various energy thresholds	108
Integral omnidirectional fluxes of protons (>10 MeV) and electrons (>1 MeV) at 400 km altitude showing the inner radiation belt's "South Atlantic anomaly" and, in the case of electrons, the outer radiation belt encountered at high latitudes	,
The flux anisotropy in low Earth orbit averaged over an orbit of the space	110
Solar proton fluence spectra for various statistical confidence levels (99 %, 95 %, 90 %, 75 % and 50 %, from top to bottom in each panel) for various	111
Cosmic ray LET spectra for typical missions	113
SHIELDOSE dataset for computing doses for arbitrary spectra:	114
Annual doses behind 4 mm spherical shielding on circular equatorial orbits in the radiation belts, as a function of orbit height	117
Typical doses predicted for typical missions	118
Typical dose-depth curves for Earth-orbits	119
Quality factors for use in dose equivalent calculations for radio-biological effect purposes, as defined by the ICRP	120
The NIEL curve: (a) energy lost by protons in non-ionizing interactions (bulk, displacement damage); (b) NIEL relative to 10 MeV giving damage-equivalence of other energies	120
Time evolution of the number of trackable objects in orbit	133
Altitude distribution of trackable objects in LEO orbits	133
Distribution of trackable objects as function of their inclination	134
Cumulative number of impacts, N from 1 side to a randomly oriented plate for a range of minimum particle sizes	134
Activity ratio factor versus period of activity for major meteoroid streams 1	35
Schematic of the magnetosphere showing the current flows and magnetic field lines	156
	Variation of the MSISE-90 mean atomic oxygen with altitude for extremely low activities, for mean activities and for extremely high activities. Variation of the MSISE-90 mean concentration profile of the atmosphere constituents N2, O, O2, He, Ar, H, and N with altitude for mean activities. Diurnal (a) and seasonal-latitudinal (b) variations of the MSISE-90 local temperature at altitude h = 400 km. Diurnal (a) and seasonal-latitudinal (b) variations of the MSISE-90 air density at altitude h = 400 km for mean atmospheric conditions. Diurnal (a) and seasonal latitudinal (b) variations of the MSISE-90 atomic oxygencentration at altitude h = 400 km for mean atmospheric conditions. Diurnal (a) and seasonal latitudinal (b) variations of wind magnitude and direction according to HWM-93 at altitude h = 400 km for mean atmospheric conditions. Diurnal (a) and seasonal-latitudinal (b) variations of wind magnitude and direction according to HWM-93 at altitude h = 400 km for mean atmospheric conditions. Mean ranges of protons and electrons in aluminium. Contour plots of the electron and proton radiation belts. Electron (a) and proton (b) omnidirectional fluxes, integral in energy, on the geomagnetic equator for various energy thresholds. Integral omnidirectional fluxes of protons (> 10 MeV) and electrons (> 1 MeV) at 400 km altitude showing the inner radiation belt's "South Atlantic anomaly and, in the case of electrons, the outer radiation belt encountered at high latitudes. The flux anisotropy in low Earth orbit averaged over an orbit of the space station for protons > 100 MeV energy. Solar proton fluence spectra for various statistical confidence levels (99 %, 95 %, 90 %, 75 % and 50 %, from top to bottom in each panel) for various mission durations (data from JPL-1991 Model). Cosmic ray LET spectra for typical missions. SHIELDOSE dataset for computing doses for arbitrary spectra: In hard adoses behind 4 mm spherical shielding on circular equatorial orbits in the radiation belts, as a function of orbit heig



Figure D-1:	Normally incident solar radiation at sea level on very clear days, solar spectrification of solar spectral at 1 AU, and black body spectral	
E' D. O.		161
Figure D-2:	Daily solar and geomagnetic activity indices over the last two solar cycles.	
Figure D-3:	Monthly mean solar and geomagnetic activity indices over the last two sola cycles.	ır 163
Figure D-4:	Power flux levels for various frequency ranges of naturally occurring electromagnetic and plasma waves (from [RDD.2]).	164
Figure F-1:	Spectrograms showing electron and ion fluxes during a charging event	170
Figure F-2:	Satellite potential and electron integral number flux above 30 eV and 14 keV [RDF.1]	171
Figure F-3:	Surface potential vs. electron temperature for a number of materials	172
Tables		
Table 1:	Mandatory model parameters	32
Table 2:	Values of normalized coefficients Cnm from JGM-2 model to degree (n) and order (m) 9	d 33
Table 3:	Values of normalized coefficients Snm from JGM-2 model to degree (n) and order (m) 9	t 33
Table 4:	Predicted orbit error associated with use of the JGM-2 gravity model	33
Table 5:	Changes in dipole moments 1945-1995	36
Table 6:	The IGRF-95 Model: Coefficients and their secular variations to degree and order 3	38
Table 7:	Changes in dipole-terms and derived dipole moments of IGRF models	38
Table 8:	Sibeck et al. [RD5.17] Magnetopause model	41
Table 9:	High-energy solar electromagnetic flux	46
Table 10:	Conversion from Kp to ap	48
Table 11:	Maximum, mean, and minimum values of the 13-month smoothed 10,7 cn solar radio flux and geomagnetic activity index over the mean solar cycle	n 48
Table 12:	Reference index values	52
Table 13:	MSISE-90 altitude profiles of temperature T, total density r, pressure p, mean molecular weight M and density scale height H for low activities	60
Table 14:	MSISE-90 altitude profiles of temperature T, total density r, pressure p, mean molecular weight M and density scale height H for mean activities	62
Table 15:	MSISE-90 altitude profiles of temperature T, total density r, pressure p, mean molecular weight M and density scale height H for extremely high activities 64	
Table 16:	Main engineering concerns due to space plasmas	80
Table 17:	Parameters for the USAF diffuse aurora model	81
Table 18:	lonospheric electron density profiles derived from IRI95 [RD8.2]	82
Table 19:	Electron density vs. L-shell for the Carpenter and Anderson [RD8.7] model, ignoring seasonal and solar cycle effects	84
Table 20:	Typical plasma parameters at geostationary orbit	86
Table 21:	Standard worst-case bi-Maxwellian environment	86



Table 22:	Solar wind parameters (from RD8.14)	87
Table 23:	Typical magnetosheath plasma parameters (from RD8.14)	87
Table 24:	Some solar UV photoionization rates at 1 AU (from RD8.17)	89
Table 25:	Photoelectron sheath parameters	89
Table 26:	Examples of appropriate plasma environments for different missions	89
Table 27:	Parameters for quantification of radiation effects	93
Table 28:	Characteristics of typical radiation belt particles	94
Table 29:	Standard field models to be used with radiation-belt models	95
Table 30:	Fluence levels for energy, mission duration and confidence levels from the JPL-1991 model	97
Table 31:	Standard probability (confidence) levels to be applied for various mission durations	97
Table 32:	Cumulative number of impacts, N, from one side to a randomly oriented pla for a range of minimum particle sizes using the ORDEM 96 debris model . 1	
Table 33:	Cumulative number of impacts, N, from one side to a randomly oriented pla for a range of minimum particle sizes using the ORDEM 96 model	
Table 34:	Cumulative number of impacts, N, from 1 side to a randomly oriented plate for a range of minimum particle sizes using the MASTER debris model 1	131
Table B-1:	Planetary gravitational characteristics	52
Table B-2:	Covariance errors in normalized coefficients Cnm (units of 10-6) from JGM-2 model to degree (n) and order (m) 9	152
Table B-3:	Covariance errors in normalized coefficients Snm (units of 10-6) from JGM-2 model to degree (n) and order (m) 9	152
Table D-1:	Running mean (averaged over 90 minutes) albedo percentile data 1	159
Table D-2:	Running mean (averaged over 90 minutes) Earth infrared radiation percentile values in units of W/m2	e 160
Table F-1:	NASA worst-case environment	173
Table G-1:	Radiation tests	177
Table H-1:	Nominal and worst case debris model parameters and mass densities 1	182
Table H-2:	Uncertainty of 90 % confidence level for debris flux	184



1

Scope

This Standard applies to all product types which exist or operate in space and defines the natural environment for all space regimes. It also defines general models and rules for determining the local induced environment.

Project-specific or project-class-specific acceptance criteria, analysis methods or procedures are not defined.

The natural space environment of a given item is that set of environmental conditions defined by the external physical world for the given mission (e.g. atmosphere, meteoroids and energetic particle radiation). The induced space environment is that set of environmental conditions created or modified by the presence or operation of the item and its mission (e.g. contamination, secondary radiations and spacecraft charging). The space environment also contains elements which are induced by the execution of other space activities (e.g. debris and contamination).



 $(This\ page\ is\ intentionally\ left\ blank)$



Normative references

The following normative documents contain provisions which, through reference in this text, constitute provisions of this ECSS Standard. For dated references, subsequent amendments to, or revisions of any of these publications do not apply. However, parties to agreements based on this ECSS Standard are encouraged to investigate the possibility of applying the most recent editions of the normative documents indicated below. For undated references the latest edition of the publication referred to applies.

ECSS-P-001 Glossary of terms

ECSS-E-10 Space engineering - System engineering

ECSS-Q-70-01 ¹⁾ Space product assurance - Contamination and cleanliness

control

Normative references for the specific components of the space environment are provided in the respective component clauses.

NOTE Informative references for the specific components of the space environment are provided in the respective component clauses.

¹⁾ To be published.



 $(This\ page\ is\ intentionally\ left\ blank)$

Terms, definitions and abbreviated terms

3.1 Terms and definitions

The following terms and definitions are specific to this Standard in the sense that they are complementary or additional with respect to those contained in ECSS-P-001.

3.1.1

A_p , K_p indices

geomagnetic activity indices to describe fluctuations of the geomagnetic field

NOTE Values of A_p range from 0 to 400 and they are expressed in units of 2 nT (nanotesla). K_p is essentially the logarithm of A_p

3.1.2

absorbed dose

energy absorbed locally per unit mass as a result of radiation exposure which is transferred through ionization and excitation

NOTE A portion of the energy absorption can result in damage to the lattice structure of solids through displacement of atoms, and this is now commonly referred to as Non-Ionizing Energy Loss (NIEL).

3.1.3

accommodation coefficient

measure for the amount of energy transfer between a molecule and a surface

3.1.4

albedo

fraction of sunlight which is reflected off a planet

3.1.5

bremsstrahlung

high-energy electromagnetic radiation in the $X-\gamma$ energy range emitted by charged particles slowing down by scattering off atomic nuclei

NOIE The primary particle is ultimately absorbed while the bremsstrahlung can be highly penetrating. In space, the



most common source of bremsstrahlung is electron scattering.

3.1.6

contaminant

foreign (or unwanted) molecular or particulate matter that can affect or degrade the performance of any component when being in line of sight with that component or when residing onto that component

3.1.7

contaminant environment

molecular and particulate environment in the vicinity of and created by the presence of a spacecraft

3.1.8

current

often used in the discussion of radiation transport to refer to the rate of transport of particles through a boundary

NOTE In contrast to flux, current is dependent on the direction in which the particle crosses the boundary (it is a vector integral). An isotropic omnidirectional flux, f, incident on a plane gives rise to a current of $\frac{1}{4}f$ normally in each direction across the plane.

3.1.9

direct flux

free stream or outgassing molecules that directly impinge onto a critical surface, i.e. without prior collisions with other gas species or any other surface

3.1.10

distribution function f(x,v)

function describing the particle density of a plasma in 6-D space made up of the three spatial vectors and the three velocity vectors, with units $s^3 \, m^{-6}$

NOTE For distributions that are spatially uniform and isotropic, it is often quoted as f(v), a function of scalar velocity, with units s m⁻⁴, or f(E) a function of energy, with units J⁻¹ m⁻³. This can be converted to flux as follows:

$$Flux = \int v f(v) dv$$
 or

$$Flux = \int \frac{f(E)}{m} dE$$

where

v is the scalar velocity;

E is the energy;

m is the particle mass.

3.1.11

dose

quantity of radiation delivered at a position

NOTE In its broadest sense this can include the flux of particles, but in the context of space energetic particle radiation ef-



fects, it usually refers to the energy absorbed locally per unit mass as a result of radiation exposure.

3.1.12

dose equivalent

quantity normally applied to biological effects and includes scaling factors to account for the more severe effects of certain kinds of radiation

3.1.13

dust

particulates which have a direct relation to a specific solar system body and which are usually found close to the surface of this body (e.g. Lunar, Martian or Cometary dust)

3.1.14

Earth infrared

Earth emitted thermal radiation

NOTE It is also called outgoing long wave radiation.

3.1.15

energetic particle

particles which, in the context of space systems radiation effects, can penetrate outer surfaces of spacecraft

NOTE For electrons, this is typically above 100 keV, while for protons and other ions this is above 1 MeV. Neutrons, gamma rays and X-rays are also considered energetic particles in this context.

3.1.16

equivalent fluence

quantity which attempts to represent the damage at different energies and from different species

EXAMPLE For example, for solar cell degradation it is often taken that one 10 MeV proton is "equivalent" to 3000 1 MeV electrons. This concept also occurs in consideration of Non-ionizing Energy Loss effects (NIEL).

NOTE Damage coefficients are used to scale the effect caused by particles to the damage caused by a standard particle and energy.

3.1.17

exosphere

part of the Earth atmosphere above the thermosphere which extends into space

3.1.18

F_{10.7} flux

solar flux at a wavelength of 10,7 cm in units of 10^4 Jansky (one Jansky equals 10^{-26} W m⁻² Hz⁻¹)

3.1.19

fluence

time-integration of the flux



flux

amount of radiation crossing a surface per unit of time, often expressed in "integral form" as particles per unit area per unit time (e.g. electrons ${\rm cm}^{-2}~{\rm s}^{-1}$) above a certain threshold energy

NOIE The directional flux is the differential with respect to solid angle (e.g. particles cm⁻² steradian⁻¹ s⁻¹) while the "differential" flux is differential with respect to energy (e.g. particles cm⁻² MeV⁻¹ s⁻¹). In some cases fluxes are also treated as a differential with respect to Linear Energy Transfer (see 3.1.28).

3.1.21

free molecular flow regime

mean free path of a molecule is greater than compared to the dimensions of the volume of interest (characteristic length)

3.1.22

geocentric solar magnetospheric coordinates (GSM)

elements of a right-handed Cartesian coordinate system (X,Y,Z) with the origin at the centre of the Earth

NOTE X points towards the Sun; Z is perpendicular to X, lying in the plane containing the X and geomagnetic dipole axes; Y points perpendicular to X and Z and points approximately towards dusk magnetic local time (MLT).

3.1.23

heterosphere

Earth atmosphere above 105 km altitude where species-wise neutral concentration profiles are established due to a diffusive equilibrium, with N_2 dominance below 200 km, O dominance from 200 km to 600 km, and He dominance as of 600 km altitude

3.1.24

homosphere

Earth atmosphere below 105 km altitude where complete vertical mixing yields a near-homogeneous composition of about 78,1 % N_2 , 20,9 % O_2 , 0,9 % Ar, and 0,1 % CO_2 and trace constituents; the homopause (or turbopause) marks the ceiling of the homosphere

3.1.25

indirect flux

molecules impinging on a critical surface, after collision with, or collision and sojourn on other surfaces

3.1.26

isotropic

property of a distribution of particles where the flux is constant over all directions

3.1.27

L or L shell

parameter of the geomagnetic field, often used to describe positions in near-Earth space

NOTE L or L shell has a complicated derivation based on an invariant of the motion of charged particles in the terrestrial magnetic field (see clause 5). However, it is useful in defining plasma regimes within the magnetosphere because, for a dipole magnetic field, it is equal to the geocentric altitude in



Earth-radii of the local magnetic field line where it crosses the equator.

3.1.28

linear energy transfer (LET)

rate of energy deposit from a slowing energetic particle with distance travelled in matter, the energy being imparted to the material

NOTE Normally used to describe the ionization track caused by passage of an ion. LET is material-dependant and is also a function of particle energy. For ions involved in space radiation effects, it increases with decreasing energy (it also increases at high energies, beyond the minimum ionizing energy). LET allows different ions to be considered together by simply representing the ion environment as the summation of the fluxes of all ions as functions of their LETs. This simplifies single-event upset calculation. The rate of energy loss of a particle, which also includes emitted secondary radiations, is the stopping power.

3.1.29

magnetic local time (MLT)

parameter analogous to longitude, often used to describe positions in near-Earth space

NOTE Pressure from the solar wind distorts the Earth magnetic field into a comet-like shape. This structure remains fixed with its nose towards the Sun and the tail away from it as the Earth spins within it. Hence longitude, which rotates with the Earth, is not a useful way of describing position in the magnetosphere. Instead, magnetic local time is used. This has value 0 (midnight) in the anti-sunward direction, 12 (noon) in the sunward direction and 6 (dawn) and 18 (dusk) perpendicular to the sunward/anti-sunward line. This is basically an extension of the local solar time on Earth, projected vertically upwards into space although allowance is made for the tilt of the dipole.

3.1.30

mass flow rate

mass (g) of molecular species crossing a specified plane per unit time and unit area (g cm $^{-2}$ s $^{-1}$)

3.1.31

Maxwellian distribution

in thermal equilibrium, plasma distribution functions can be described in terms of scalar velocity, v, by the Maxwellian distribution below:

$$f(v) = 4\pi n \left(\frac{m}{2\pi kT}\right)^{3/2} v^2 \exp\left(-\frac{v^2 m}{2kT}\right)$$

where

n is the density;

k is the Boltzmann constant;

T is the temperature.

NOTE The complete distribution is therefore described by a pair of numbers for density and temperature. Even non-equilibrium distributions can often be usefully described by a combination of two Maxwellians.



meteoroids

particles in space which are of natural origin; nearly all meteoroids originate from asteroids or comets

3.1.33

molecular column density (MCD)

integral of the number density (number of molecules of a particular species per unit volume) along a specified line of sight originating from a (target, critical, measuring, reference) surface

3.1.34

molecular contaminant

contaminant without observable dimensions

3.1.35

omnidirectional flux

scalar integral of the flux over all directions

NOTE This implies that no consideration is taken of the directional distribution of the particles which can be non-isotropic. The flux at a point is the number of particles crossing a sphere of unit cross-sectional surface area (i.e. of radius $1/\sqrt{\pi}$). An omnidirectional flux is not to be confused with an isotropic flux.

3.1.36

outgassing rate

mass of molecular species evolving from a material per unit time and unit surface area $(g\ cm^{-2}\ s^{-1})$

NOTE Outgassing rates can also be given in other units, such as in relative mass unit per time unit: $(g s^{-1})$, $(\% s^{-1})$ or $(\% s^{-1} cm^{-2})$.

3.1.37

particulate contaminant

solid or liquid contaminant particles

3.1.38

permanent molecular deposition (PMD)

molecular matter that permanently sticks onto a surface (non-volatile under the given circumstances) as a result of reaction with surface material, UV-irradiation or residual atmosphere induced reactions (e.g. polymerization, formation of inorganic oxides)

3.1.39

plasma

partly or wholly ionized gas whose particles exhibit collective response to magnetic and electric fields

NOTE The collective motion is brought about by the electrostatic Coulomb force between charged particles. This causes the particles to rearrange themselves to counteract electric fields within a distance of the order of the Debye length. On spatial scales larger than the Debye length plasmas are electrically neutral.



radiation

transfer of energy by means of a particle (including photons)

NOTE In the context of this Standard, electromagnetic radiation below the X-ray band is excluded. This therefore excludes UV, visible, thermal, microwave and radio-wave radiation.

3.1.41

return flux

molecules returning to (in the direction of) the source or a surface not in direct view; the cause can be:

- collisions with other residual natural atmospheric species (ambient scatter) or with other identical or different contaminant species (self scatter) before reaching the critical surface;
- ionization or dissociative ionization of the molecules under radiation (e.g. UV or particles) and subsequent attraction to a charged surface

3.1.42

single-event upset (SEU), single-event effect (SEE), single-event latch-up (SEL)

these effects are the result of the highly localized deposition of energy by single particles or their reaction products: the energy deposition is sufficient to cause observable effects

3.1.43

space debris

man-made objects or parts thereof in space which do not serve any useful purpose

- NOTE 1 The term space debris is used here exclusively for manmade objects in space.
- NOTE 2 In some NASA documents these man-made particles are referred to as "orbital debris" and the term space debris is used to denote both, natural meteoroids and man-made objects.

3.1.44

solar constant

electromagnetic radiation from the Sun that falls on a unit area of surface normal to the line from the Sun, per unit time, outside the atmosphere, at one astronomical unit (1 AU = average Earth-Sun distance)

3.1.45

solar flare

emission of optical, UV and X-radiation from an energetic event on the Sun

NOTE There is some controversy about the causal relationship between solar flares and the arrival of large fluxes of energetic particles at Earth. Therefore, it is more consistent to refer to the latter as Solar Energetic Particle Events (SEPEs).

3.1.46

sticking coefficient

parameter defining the probability that a molecule, colliding with a surface, stays onto that surface for a time long compared to the phenomena under investigation

NOTE It is a function of parameters such as contamination/surface material pairing, temperature, photo-polymerization, reactive interaction with atomic oxygen.



surface accommodation

situation which occurs when a molecule becomes attached to a surface long enough to come into a thermal equilibrium with that surface

3.1.48

thermosphere

Earth atmosphere between 120 km and 250 km to 400 km (depending on the activity level), where temperature has an exponential increase up to a limiting value T_{∞} at the thermopause (where T_{∞} is the exospheric temperature)

3.1.49

VCM-test

screening thermal vacuum test to determine the outgassing properties of materials

NOIE The test is described in ECSS-Q-70-04 and ASTM-E595 [RD11.1, RD11.2]. The test results are:

- TML Total Mass Loss, measured ex-situ as a difference of mass before and after exposure to a vacuum under the conditions specified in the outgassing test, normally expressed in % of initial mass of material.
- CVCM Collected Volatile Condensable Material, measured ex-situ on a collector plate after exposure (to a vacuum) under the conditions specified in the outgassing test, normally expressed in % of initial mass of material.

3.2 Abbreviated terms

The following abbreviated terms are defined and used within this Standard.

Abbreviation	Meaning
ASTM	American Society for Testing and Materials
AE	auroral electrojet
AO	atomic oxygen
BIRA	Belgisch Instituut voor Ruimte-Aeronomie
CIRA	COSPAR International Reference Atmosphere
COSPAR	Committee on Space Research
CVCM	collected volatile condensable material
DISCOS	ESA's database and information system characterizing objects in space
DTM	density and temperature model
e.m.f.	electro-motive force
GCR	galactic cosmic ray
GEO	geostationary Earth orbit
GRAM	global reference atmosphere model
GSM	geocentric solar magnetospheric co-ordinates
HEO	high eccentric orbit
HWM	horizontal wind model
IASB	Institute d'Aeronomie Spatiale de Belgique
IDES	integrated debris evolution suite
IECM	in-flight experiment for contamination monitoring
LDEF	long duration exposure facility



LEO low Earth orbit

LET linear energy transfer

MAH model of the high atmosphere

MASTER meteoroid and space debris terrestrial environment refer-

ence model

MCD molecular column densityMEO medium (altitude) Earth orbit

MET Marshall engineering thermosphere model

MLT magnetic local time

MSIS mass spectrometer and incoherent scatter

NIEL non-ionizing energy loss

PMD permanent molecular deposition

R Sunspot number r.m.s. root-mean-square

RTG radioisotope thermo-electric generator

SEUsingle-event upsetSEEsingle-event effectSELsingle-event latch-upSEPssolar energetic particles

SEPE solar energetic particle events

SPE solar particle eventsSRP solar radiation pressure

TML total mass lossTD total density model

USSA US standard atmosphere
VCM volatile condensable material

VUV vacuum ultra violet



 $(This\ page\ is\ intentionally\ left\ blank)$



4

Gravitation

4.1 Introduction

4.1.1 Newton's law of gravitation

Gravity models are necessary to define the motion of a satellite in orbit about a central body. The gravitational field influences the motion both, of the centre of mass (trajectory), and about the centre of mass (attitude) of the satellite. Newton's Law of Gravitation states that any two bodies attract each other with a force proportional to the product of their masses, and inversely proportional to the square of the distance between them. This relationship is used to define the force of a central body acting on a satellite (and vice versa). This can be expressed as:

 $F = -\frac{GMm}{r^2}$

where

F is the gravitational force;

G is the factor of proportionality in Newton's Law of Gravitation, the

so-called universal gravitational constant;

m is the mass of the satellite;

M is the mass of the central body;

r is the distance between their centres of mass.

If the central body is spherical and isolated from other bodies, then in the absence of an atmosphere, the orbit of a satellite about this body is an ellipse of constant size and shape, in a plane whose direction remains fixed in space. The moment due to the gravitational force acting on the different mass elements of the satellite is termed the gravity gradient torque. In the absence of other disturbance torques, this moment causes the longitudinal axis of the satellite to align with the centre of the body. As its name implies, the gravity gradient torque decreases with the cube of the distance between the masses.



4.1.2 Departures from the point-mass model

The Earth is not a perfect sphere, nor is it isolated in space. Thus the motion of a satellite in orbit about the Earth departs from the simple behaviour described above. Depending upon the nature of the application, a more complex model of the Earth gravitational field can be required. For preliminary engineering analyses, simple analytic expressions exist which characterize the dominant perturbations to a satellite orbit due to Earth gravitational anomalies. These relations are derived from the more comprehensive spherical harmonic representations of the Earth gravitational field that are presented in subclause 4.3.1, but assume that the Earth is symmetric about its polar axis and consider only the dominant terms in the harmonic expansions. These expressions are given in annex B. Gravity gradient stabiliszation is normally used where only coarse Earth pointing accuracy is required (>1°) and thus the point-mass model given above is applicable for most applications. A comprehensive treatise on gravity gradient stabilization is given by Regan and Anandakrishnan [RD4.1] and Wiesel [RD4.2]. When considering the gravitational attraction for an Earth-orbiting satellite due to the Sun and Moon, point mass models are normally sufficient. Mass values for these bodies and the other planets within the solar system are presented in annex B.

4.1.3 Accurate representation of the geopotential

For orbit prediction or trajectory determination purposes an accurate representation of the gravity field of the Earth is necessary. As the Earth is not a perfect sphere it is necessary to represent the geopotential field in terms of a central force augmented by a series of spherical harmonics²⁾ satisfying Laplace's equation in empty space ($\nabla^2 U = 0$). The geopotential can be expressed as:

$$U(r,\phi, \lambda) = \frac{GM_{\oplus}}{\gamma} \left(1 + \sum_{n=2}^{\infty} \sum_{m=0}^{n} \left(\frac{\alpha}{r} \right)^{n} P_{nm}(\sin \phi) [C_{nm} \cos(m\lambda) + S_{nm} \sin(m\lambda)] \right)$$

where

G is the constant of gravitation;

 M_{\oplus} is the mass of the Earth;

r is the radial distance from the Earth's centre of mass;

a is the semimajor axis of the reference ellipsoid (normally taken as the

equatorial radius of the Earth, R_{\oplus});

n is the degree of the harmonic term;

m is the order of the harmonic term;

 ϕ is the geocentric latitude;

 λ is the geocentric longitude;

 C_{nm} , S_{nm} are spherical harmonic coefficients;

 $P_{nm}\left(\sin\phi\right)$ are associated Legendre functions of the first kind where:

$$P_{nm}(\sin \phi) = \frac{(\cos \phi)^m}{2^n n!} \frac{d^{n+m}(\sin^2 \phi - 1)^n}{d^{n+m}(\sin \phi)}$$

are Legendre polynomials.

²⁾ Other forms of the potential, expressed in terms of ellipsoidal coordinates have also been developed but result in a more complex representation requiring use of elliptic Legendre polynomials of the second kind. The development of the potential in terms of spherical harmonics is a natural one to adopt in the analysis of satellite orbits because the symmetry properties of the harmonics correspond to the division of the potential according to the type of change in the classical orbital elements.



For computational purposes these expressions and their corresponding coefficients are used in their normalized form \overline{P}_{nm} , \overline{C}_{nm} , and \overline{S}_{nm} where:

$$\overline{P}_{nm} = \left[\frac{(2n+1) k (n-m)!}{(n+m)!} \right]^{1/2} P_{nm}$$

$$\overline{C}_{nm} = \left[\frac{(n+m)!}{(2n+1) k (n-m)!} \right]^{1/2} C_{nm}$$

$$\overline{S}_{nm} = \left[\frac{(n+m)!}{(2n+1) k (n-m)!} \right]^{1/2} S_{nm}$$

where k = 1 when m = 0, k = 2 when $m \neq 0$.

Depending upon its degree n and order m a Legendre function is referred to as:

- 1. a *zonal* harmonic when m = 0
- 2. a *sectorial* harmonic when m = n
- 3. a *tesseral* harmonic when $m \neq n$.

A zonal harmonic corresponds geometrically to a particular shape of the geopotential surface [RD4.3]. The second zonal harmonic (m = 0, n = 2) which expresses the main effect of the Earth flattening, makes a north-south slice through the Earth appear elliptical; the third zonal harmonic (m = 0, n = 3) provides a profile with a tendency to a triangle; the fourth harmonic relating to a square, the fifth to a pentagon, and so on.

A similar representation can be envisaged for longitudinal variation. Thus at any fixed latitude ϕ , the variation of geoid height with longitude λ is a sinusoidal oscillation having a wavelength $2\pi/m$, e.g. each harmonic of order 15 produces bulges every $24^{\rm o}$ in longitude.

The evaluation of spherical harmonic coefficients is a non-trivial task. Models are based on analyses of satellite observations, either photographic, Doppler or laser in nature, together with terrestrial gravity measurements and data from satellite altimeters.

The development of gravity models and evaluation of the geopotential coefficients is a constantly evolving process [RD4.4]. The first gravity models were based on the analysis of Transit satellite Doppler tracking data and Baker-Nunn camera observations and were produced by John Hopkins University's Applied Physics Laboratory and the Smithsonian Astrophysical Observatory. These were complete to degree and order 8.

At the present time there are five contemporary gravity models being used within the astrodynamics community. These are WGS-84 developed by the United States of America's Department of Defence, TEG-2B developed by the University of Texas (UT), OSU-91A developed by Ohio State University (OSU), GRIM4 developed by the European community, and JGM-2 developed by NASA, UT, CNES, and OSU. All of the models provide metre-level accuracy for orbit computation purposes. Use of the JGM-2 model is recommended as it represents the best long wavelength representation of the Earth that is currently available, and can provide centimetre-level accuracy. The JGM-2 model comprises results from OSU-91A [RD4.5] and TEG-2B [RD4.6] in its formulation. The WGS-84 and GRIM4 models are discussed briefly in the annex. A new model EGM-96 has recently been developed by the National Imagery and Mapping Agency, Goddard Space Flight Center and OSU. Although not yet established within the community, this is a possible candidate for a future successor to JGM-2 as the ESA standard model (see annex B).



4.2 Model presentation

4.2.1 Model

JGM-2 (Joint Gravity Model) [RD4.7] was developed from a combination of satellite tracking data, surface gravimetry and satellite altimetry observations. It is complete to degree and order 70 in spherical harmonics.

4.2.2 Mandatory model parameters

Table 1: Mandatory model parameters

Parameter	Value	Units
Constant of Gravitation, G	$6,67259 \times 10^{-11}$	${ m m}^3{ m kg}^{-1}{ m s}^{-2}$
Earth equatorial radius, R_{\oplus}	6378136,3	m
Geocentric Mass, M_{\oplus}	$5,97370 \times 10^{24}$	kg
GM_{\oplus}	398600,4415	$\mathrm{km^3\ s^{-2}}$

4.2.3 Guidelines for use

Three models were developed within the JGM-2 family. JGM-2S contains only the satellite tracking data used in JGM-2. JGM-2S is complete to degree 70. A further version JGM-2G was developed to accommodate geophysicists. The principal cause of uncertainty in the JGM-2 model is the sparsity of tracking data from satellites in different inclination bands and the lack of precise tracking data for satellites in very low orbits. The portion of the model up to degree 70 is well known, due principally to tracking data from the LAGEOS satellite. The short wavelengths of the JGM-2 model were predominantly determined using altimeter and surface gravity data, and thus are inherently less accurate. However, the JGM-2 model is more than adequate for most astrodynamics and engineering applications, while oceanographers performing precise altimeter computations are advised to use the JGM-2G version of the model. The coefficients for all these models can be obtained over the Science Internet via anonymous file transfer protocol (ftp) from **geodesy@gsfc.nasa.gov**. If a truncated set of coefficients is used, validation of the data set should be established for the particular application.

4.3 Reference data

4.3.1 Model output

Tables 2 and 3 give the values of the normalized spherical harmonic coefficients \overline{C}_{nm} and \overline{S}_{nm} to degree and order 9. Their associated 1 σ errors are given in annex B

4.3.2 Results for typical missions

Table 4 provides an estimate of the predicted orbit error in the radial, cross-track and along-track directions for representative missions associated with use of the full JGM-2 gravity model.



Table 2: Values of normalized coefficients \overline{C}_{nm} from JGM-2 model to degree (n) and order (m) 9

	n								
		2	3	4	5	6	7	8	9
	0	-484,1654663	0,9571224	0,5401433	0,0684645	-0,1500030	0,0909460	0,0493049	0,0267036
	1	-0,0001870	2,0283997	-0,5363680	-0,0591214	-0,0761294	0,2758256	0,0232834	0,1462664
	2	2,4390838	0,9044086	0,3503493	0,6533875	0,0486483	0,3278766	0,0787560	0,0245294
	3		0,7211539	0,9902582	-0,4519017	0,0579537	0,2508965	-0,0208114	-0,1619243
m	4			-0,1884885	-0,2950801	-0,0862993	-0,2755462	-0,2448369	-0,0085254
	5				0,1749710	-0,2671890	0,0018128	-0,0251488	-0,0166623
	6					0,0098855	-0,3590382	-0,0651558	0,0626750
	7						0,0012547	0,0671575	-0,1184886
	8							-0,1238923	0,1884251
	9								-0,0481248

Units of 10⁻⁶

Table 3: Values of normalized coefficients \overline{S}_{nm} from JGM-2 model to degree (n) and order (m) 9

	(, () -								
n									
		2	3	4	5	6	7	8	9
	1	0,0011953	0,2488066	-0,4734226	-0,0955327	0,0265588	0,0967770	0,0591996	0,0206503
	2	-1,4001093	-0,6192306	0,6628689	-0,3237786	-0,3737880	0,0940337	0,0662488	-0,0337777
	3		1,4140369	-0,2010099	-0,2150966	0,0090304	-0,2166254	-0,0866613	-0,0751423
	4			0,3088453	0,0496700	-0,4716700	-0,1238634	0,0702875	0,0192064
m	5				-0,6696502	-0,5365234	0,0177164	0,0892490	-0,0543111
	6					-0,2370946	0,1517702	0,3092402	0,2224258
	7						0,0244337	0,0746269	-0,0965854
	8							0,1204626	-0,0031477
	9								0,0966002

Units of 10⁻⁶

Table 4: Predicted orbit error associated with use of the JGM-2 gravity model

	Semimajor		Inclination	nclination Predicted orbit error (cm)		ror (cm)
Satellite	axis (km)	Eccentricity	(°)	Radial	Cross-track	Along-track
ERS-1	7153	0,001	98,8	8,0	15,1	160,4
Ajisai	7870	0,001	50,0	2,6	3,6	13,2
Starlette	7331	0,020	49,8	5,2	7,2	16,1
GEOS 3	7226	0,001	114,9	6,6	9,6	72,5
GEOS 1	8075	0,073	59,3	2,3	3,0	45,1
GEOS 2	7711	0,031	105,8	3,3	5,1	63,8
Peole	7006	0,016	15,0	981,0	106,7	353,5
BE-C	7507	0,025	41,2	9,2	11,4	60,0
DI-C	7341	0,053	40,0	14,5	16,9	70,7
DI-D	7622	0,084	39,5	10,1	11,2	88,9
NOVA	7559	0,001	90,0	9,6	21,7	397,0



4.4 References

- RD4.1 Regan F.J. and S.M. Anandakrishnan, "Dynamics of Atmospheric Re-entry", ISBN 1-56347-048-9, 1993.
- RD4.2 Wiesel, W.E., "Space Dynamics", McGraw-Hill, Hightstown, NJ, 1989.
- RD4.3 King-Hele D.G., "Satellite Orbits in an Atmosphere", ISBN 0-216-92252-6, Published by Blackie and Son Ltd, Glasgow, 1987.
- RD4.4 "Recommended Practice: Astrodynamics Concepts, Terms, and Symbols Part 1", BSR/AIAA R-064-1994.
- RD4.5 Rapp, R.H., Y.M. Wang, and N.K. Pavlis, "The Ohio State 1991 Geopotential and Sea Surface Topography Harmonic Coefficient Models", Report 410, Depart of Geodetic Science and Surveying, Ohio State University, Columbus, Ohio, USA, 1991.
- RD4.6 Tapley, B.D., C.K. Shum, D.N. Yuan, J.C. Ries, R.J. Eanes, M.M. Watkins and B.E. Schutz, "The University of Texas Earth Gravity Model", Paper presented at IUGG XX General Assembly, IAG Symp. G3, Gravity Field Determination from Space and Airborne Measurements, Vienna, Austria, August 12–24, 1991.
- RD4.7 Nerem R.S., F.J. Lerch, J.A. Marshall, E.C. Pavlis, B.H. Putney, B.D. Tapley, R.J. Eanes, J.C. Ries, B.E. Schutz, C.K. Shum, M.M. Watkins, S.M. losko, J.C. Chan, S.B. Luthcke, G.B. Patel, N.K. Pavlis, R.G. Williamson, R.H. Rapp, R. Biancale, and F. Nouel, "Gravity Model Development for TOPEX/POSEIDEN: Joint Gravity Models 1 and 2", J. Geophys. Res., Vol. 99, No. c12, Pages 24,421–24,447, December 15, 1994.

5

Geomagnetic fields

5.1 Introduction – Overview of the geomagnetic field and effects

At low altitude, the Earth field is approximately that of a magnetic dipole while at high altitude it is strongly distorted by the interactions with the solar wind.

Models of the Earth magnetic field are required by models of trapped (radiation-belt), solar and cosmic ray particle environments. Trapped particle morphologies are described in terms of location in idealized geomagnetic dipole space $(B,\,L)$ coordinates), while the field is needed in order to include magnetic shielding effects for solar energetic particle and cosmic ray environments. Field models are also used for magnetospheric physics studies, such as tracing the trajectories of particles through the magnetosphere.

Spacecraft motion across the geomagnetic field results in an induced motional e.m.f. given by $\underline{E} = \underline{v} \times \underline{B}$ in the spacecraft. If a current path can be completed, a current flows through the spacecraft and the surrounding plasma. These phenomena can lead to generation of a few volts potential differences on large spacecraft in LEO. The effect is also used or studied in tethered satellite missions where the length of the tether perpendicular to \underline{B} can lead to large currents and potentials.

Interaction between the magnetic field and an on-board magnetic moment \underline{m} gives rise to a force:

$$F = (m.\nabla)B$$

which can be used for attitude control where an on-board magnetic torquer provides \underline{m} .

This clause deals largely with quasi-static geomagnetic fields, data which are needed for the most common applications. However, the magnetosphere is a dynamic system and, especially in the outer parts, is characterized by large fluctuations in plasma populations, electric fields and magnetic fields. It is through the induced disturbances to the main geomagnetic field that the onset of geomagnetic sub-storms at high altitude can be monitored. These disturbances are quantified by observations on the surface of the Earth of the familiar $K_{\rm p}, A_{\rm p}, D_{\rm st}$ and other geomagnetic indices (see clause 6 for more detail on geomagnetic activity indices). The disturbed plasma environment which often accompanies such sub-storms can lead to electrostatic charging (see clause 8 for details).



5.2 Reference data on the geomagnetic field

The total field strength in an ideal dipole is given by

$$B = MR^{-3}[1 + 3\sin^2\lambda]^{1/2}$$

where λ is the magnetic latitude and R is the radial coordinate (R,λ) constituting a polar coordinate system). M is the magnetic dipolar moment. In a dipole approximation for the Earth field, M currently has a value of about $7.9 \times 10^{30} \, \mathrm{nT.~cm^3}$ or $30400 \, \mathrm{nT.~R_E^3}$ where R_E is the mean radius of the Earth. The dipole which approximates the Earth field is both tilted and offset with respect to the Earth's rotation axis, so that the geomagnetic poles do not coincide with the geographic poles and the field strength is not independent of longitude. This configuration is called an eccentric dipole [RD5.1]. Furthermore, the geomagnetic field is slowly changing. The 1990 value for the displacement of the eccentric dipole is 515 km, increasing at 2,6 km per year in the direction of 15,6° N, 150,9° E. An eccentric dipole has axial poles but also dip poles where the field lines are normal to the Earth's surface [RD5.1]. The 1985 axial northern pole (geomagnetic south) was at 82,05° N, 270,2° E. Reference RD5.1 contains an extensive discussion of the geomagnetic dipole and its variations. Table 5 shows the slow decay in the dipole moment.

Table 5: Changes in dipole moments 1945-1995

Year	$M_{\rm E}~({ m nT}.R_{\rm E}^3)$	<i>M</i> (nT.cm ³)
1945	31259,7	$8,0844 \times 10^{30}$
1955	31125,9	$8,0498 \times 10^{30}$
1965	30951,6	$8,0047 \times 10^{30}$
1975	30696,4	$7,9387 \times 10^{30}$
1985	30438,0	$7,8719 \times 10^{30}$
1995	30207,7	$7,8123 \times 10^{30}$

5.3 Geomagnetic field models and analysis methods

5.3.1 Dipole model

Many scoping estimates of geomagnetic field effects can be made with the assumption of a dipole model for the Earth's field, as given above. However, account should be taken of the tilt and displacement of the dipole axis described in 5.2.

The radial and latitudinal components of the field are given in polar coordinates by:

$$B_R = -\frac{M}{R^3} 2 \sin \lambda$$

$$B_{\lambda} = \frac{M}{R^3} \cos \lambda$$

and in Cartesian coordinates by:

$$B_r = 3xz M R^{-5}$$

$$B_y = 3yz M R^{-5}$$

$$B_z = (3z^2 - R^2) M R^{-5}$$

where

M can be taken from the table above;

R is the radius of the location in units consistent with the units of M. The z axis is along the dipole axis.



5.3.2 Internal-source field models

Although to a first approximation the Earth internally-generated magnetic field is dipolar, the non-dipolar contributions are important and are best described by numerical models of the field which also account for the offset and tilt of the geomagnetic axis with respect to the Earth's rotation axis.

The standard numerical models of the geomagnetic field in general use describe the internal field and its secular variations by spherical harmonic expansions of the scalar potential V [RD5.2]:

$$\mathbf{B} = -\nabla \mathbf{V}$$

Although a number of geomagnetic field models are available, the main internationally accepted standard ones are those in the International Geomagnetic Reference Field (IGRF) series [RD5.3]. These shall be used as the standard expect for special reasons given elsewhere in this clause and in clause 9. The potential expansion is:

$$V = a \sum_{n=1}^{k} \left\{ \left(\frac{\underline{a}}{R} \right)^{n+1} \sum_{m=0}^{n} \left[g_n^m \cos(m\phi) + h_n^m \sin(m\phi) \right] P_n^m(\cos\theta) \right\}$$
 (5.1)

where a is the radius of a reference sphere and has a value of 6371,2 km for the IGRF models, corresponding to the mean Earth radius. The position of a point of interest is specified with R, θ and ϕ , the geocentric distance, co-latitude (measured from the geographic north pole) and longitude respectively; g_n^m and h_n^m are the model coefficients and P_n^m are Schmidt normalised associated Legendre functions.

The IGRF models released since 1960 have had 120 spherical harmonic coefficients (to degree and order 10) and a further 80 (to degree and order 8) describing the secular variations of the corresponding main field coefficients in a linear fashion.

5.3.3 Eccentric dipole model

For the IGRF-95 model [RD5.4], the first 15 coefficients and their secular variations are shown in Table 6 below. Note that the first 3 terms represent contributions to a centred (tilted) dipole from dipoles along the three Cartesian axes while the first 8 terms define an eccentric (offset and tilted) dipole. Fraser-Smith [RD5.1] describes how the eccentricity, tilt and axial poles can be computed from these terms.

Figure 1 shows the total field strength at an altitude of 400 km super-imposed on a world-map.

As described in annex C, the total dipole strength (moment) can be derived from the first three terms as follows:

$$M = \alpha^{3} [(g_{1}^{0})^{2} + (g_{1}^{1})^{2} + (h_{1}^{1})^{2}]^{1/2}$$

So given field model, it is possible to extract a value of dipole moment which includes, through the secular variations to g and h, changes with time. Table 7 shows how the first 3 model coefficients of the IGRF series models have been changed with time, and the consequent changes in geomagnetic dipole moment.



Table 6: The IGRF-95 Model: Coefficients and their secular variations to degree and order 3

			Coefficient	Secular variation
	m	n	(nT)	(nT/y)
g	0	1	-29682	17,6
g	1	1	-1789	13,0
h	1	1	5318	-18,3
g	0	2	-2197	-13,2
g	1	2	3074	3,7
h	1	2	-2356	-15,0
g	2	2	1685	-0,8
h	2	2	-425	-8,8
g	0	3	1329	1,5
g	1	3	-2268	-6,4
h	1	3	-263	4,1
g	2	3	1249	-0,2
h	2	3	302	2,2
g	3	3	769	-8,1
h	3	3	-406	-12,1

Table 7: Changes in dipole-terms and derived dipole moments of IGRF models

	Mod	lel coefficie	ents		
IGRF	_	_	_	$M_{ m E}$	M
model	\boldsymbol{g}_{0}^{1}	\boldsymbol{g}_{1}^{1}	$m{h}_{1}^{1}$	$(\mathbf{nT}.R_{\mathrm{E}}^{3})$	(nT.cm ³)
1945	-30634,	-2240,	5806,	31259,7	$8,0844 \times 10^{30}$
1955	-30507,	-2134,	5796,	31125,9	$8,0498 \times 10^{30}$
1965	-30334,	-2119,	5776,	30951,6	$8,0047 \times 10^{30}$
1975	-30100,	-2013,	5675,	30696,4	$7,9387 \times 10^{30}$
1985	-29877,	-1903,	5497,	30438,0	$7,8719 \times 10^{30}$
1990	-29775,	-1851,	5411,	30319,2	$7,8412 \times 10^{30}$
1995	-29682,	-1789,	5318,	30207,7	$7,8123 \times 10^{30}$

5.3.4 Geomagnetic coordinates -B and L

Geomagnetic coordinates are useful or necessary for a number of applications where charged particle morphology or behaviour needs to be described in the magnetosphere. The most important application is in models of the Earth radiation-belt environment (see clause 9). These particle models give fluxes of trapped energetic particles as functions of particle energy and of McIlwain's geomagnetic co-ordinates L and B/B_0 . L is the radial distance of the field line from the axis at the geomagnetic equator in an ideal dipole field and B is the magnetic field strength, determining the position along a field line from the minimum B_0 at the geomagnetic equator. For many applications the pair B, L (or equivalently, B/B_0 , L) is sufficient to define a location in the field because of its azimuthal symmetry and the azimuthal symmetry in particle populations.



In the true geomagnetic field, which is only quasi-dipolar, L is formally defined by means of a function of the adiabatic integral invariant I [RD5.5]:

$$I = \int_{l_1}^{l_2} \left(1 - \frac{B}{B_m}\right)^{1/2} dl$$

where the integral is evaluated along the field line between the two conjugate mirror points l_1 and l_2 and B_m is the field at the mirror points. I is a constant on a field line or drift shell. The definition of L is then written as [RD5.5, RD5.6]:

$$L^{3}\left(\frac{B}{M}\right) = f\left(\frac{I^{3}B}{M}\right) \tag{5.2}$$

where M is the geodipole moment (McIlwain used a constant value M = 31165,3 nT.R_E). The function f is evaluated using values for I and B derived from the true geomagnetic field via a model. Hilton [RD5.7] provided a simple approximation for the function f:

$$f(x) = 1 + a_1 x^{1/3} + a_2 x^{2/3} + a_3 x (5.3)$$

where

x = I^3B/M ; a_1 = 1,35047; a_2 = 0,456376; a_3 = 0,0475455.

L is found to be nearly constant on a field-line or "drift shell". A charged particle in the geomagnetic field has three basic components of motion: a gyration about field-lines, a bouncing motion between magnetic mirrors at higher-field parts of the field-lines and an azimuthal drift around the Earth, tracing out a drift shell. By transforming orbital locations into the B,L coordinate system and accessing the radiation environment models throughout the orbit, predictions can be made of satellite radiation exposures (see clause 9).

It is clear from this that computation of L at a point involves an integration along a field line, making use of a magnetic field model. It is important that the method of integration and the parameters M and a_1, a_2, a_3 are consistent when preparing particle environment models and accessing them. For the purposes of radiation belt models, McIlwain's value was used, un-updated for magnetic moment changes, and this value shall be used in access routines for the AE-8 and AP-8 models specified in clause 9. Furthermore, only the magnetic field models specified in clause 9 shall be used for the generation of B, L coordinates for employing these particle models.

At the geomagnetic equator, which corresponds to the position on a field line with the minimum B,

$$B = B_0 = ML^{-3}$$

where M is the geomagnetic dipole moment.

Polar coordinates in idealized dipole space are related to B and L by:

$$R = L \cos^2 \lambda$$

and the field strength given by

$$B = \frac{M}{R^3} (1 + 3\sin^2 \lambda)^{1/2}$$

where λ is the magnetic latitude and R is the radial coordinate which clearly has a value $R_0 = L$ at the magnetic equator.



5.3.5 External-source field models

The models described above only describe the field generated by processes within the Earth. At high altitudes most of the higher-order terms become negligible and the dipole approximation is often adequate to describe this contribution. However, the solar wind causes large diurnal distortions of the field at high altitude (see Figure 2 [RD5.8]). This effect, together with the ring current from azimuthally drifting particles, and other current systems means that the internal field is a poor representation of the total field. The effects of the other current systems are to introduce diurnal variations into the magnetic field and a perturbation from the external current systems varying with solar and geomagnetic activity (solar wind pressure, ring current intensity, K_P variations).

Various models for the external contributions to the field have been developed by Tsyganenko [RD5.9, RD5.10], Olsen and Pfitzer [RD5.11] and Mead and Fairfield [RD5.12]. No internationally recognized standard has yet appeared although progress is being made in that direction [RD5.13]. Since these models include the diurnal asymmetry of the field and depend on geomagnetic activity indices, they are attractive for use in mapping energetic particle fluxes and their responses to activity variations. The post-flight data analysis programme for the CRRES mission makes use of external field models [RD5.14]. However, the effect of the high-altitude distortions is to make the equatorial radius of the drift-shell of a particle dependent on the particle's pitch-angle, so that populations are separated and merged azimuthally in a way that complicates the modelling of their morphologies.

External-source models should not be used in conjunction with current standard radiation-belt environment models described in clause 9.

No particular external source model is required as standard.

The field magnitudes involved in the external sources are very small and it is emphasized that only in special circumstances do they need to be considered. Bass and Jordan [RD5.15] inter-compared various models and show the magnitudes of the errors with various models and also compared with CRRES magnetometer data can be large, but it should be re-emphasized that the fields are themselves relatively weak here.

One of the areas where an external model of the geomagnetic field is useful is for improved B,L coordinate calculation for trapped radiation-belt models. Using an internal-only field results in an error compared to an internal-plus-external model of up to one Earth-radius at high altitudes. Such improved methods shall be consistently applied as mentioned previously: the model generation and access routines shall use the same methods for B and L calculation.

The field at geostationary orbit is of approximately 100 nT strength with an approximately 50 % modulation due to the diurnal asymmetry. During severe geomagnetic storm events, the field strength can completely reverse and reach -200 nT. In the geomagnetic tail (anti-sunward direction) the direction of the field can be far from parallel to the Earth geomagnetic or rotation axes. Data on magnetic field fluctuations at geostationary orbit are available from the GOES satellite space environment data archive [RD5.16].

Figure 3 shows the variation of the total geomagnetic field as a function of altitude, as derived from a combined internal and external source model. Various local time and activity conditions are shown. The error bar at geostationary altitude qualitatively represents the variability.



5.3.6 Magnetospheric boundaries

Some simple expressions can be used to estimate basic locations of magnetospheric boundaries for mission planning. The stand-off radial distance of the magnetopause in the sunward direction is given by:

$$L_{mp} = 107,4 (n_{sw} u_{sw}^2)^{-1/6}$$

where L_{mp} is in units of Earth-radii, n_{sw} , the solar wind proton number density is in units of cm⁻³ and the solar wind bulk velocity is in units of km/s. Typical values for n_{sw} and u_{sw} are 8 cm⁻³ and 450 km/s respectively, leading to a stand-off distance of about 10 Earth-radii.

For modelling the full magnetopause position, the following model of Sibeck et al. [RD5.17] shall be used. This represents the magnetopause position as the function:

$$R^2 + A x^2 + B x + C = 0$$

where

 $R^2 = y^2 + z^2;$

x, y, and z are GSM coordinates, in Earth-radii;

A, B and C are fit parameters dependent on the solar wind pressure as given in Table 8.

Solar wind pressure range (nPa)	A	В	C	Sub-solar point $(R_{ m E})$	Dawn meridian $(R_{ m E})$
0,54-0,87	0,19	19,3	-272,4	12,6	16,5
0,87-1,47	0,19	19,7	-243,9	11,7	15,6
1,47-2,60	0,14	18,2	-217,2	11,0	14,7
2,60-4,90	0,15	17,3	-187,4	10,0	13,7
4.90-9.90	0.18	14.2	-139.2	8.8	11.8

Table 8: Sibeck et al. [RD5.17] Magnetopause model

5.4 Tailoring guidelines

As has already been mentioned, careful consideration should be given to application needs before selecting a model. A low-fidelity dipole model (aligned, eccentric or tilted dipoles) can suffice for many engineering applications. Most engineering applications never have need of the external-source model augmentation. These can only be necessary for mission planning for magnetospheric missions or if data on high latitude or high altitude variability of the fields with respect to local time and solar-geomagnetic activity is required. They can also be necessary where magnetic torquing is used at high altitudes such as in geostationary orbit, although the dynamic variability of the field at high altitudes shall be taken in to account.

For radiation belt modelling applications consistence shall be assured between the model's construction field model and the users access field model (e.g. Jensen-Cain and GSFC models for AE and AP series models – see clause 9).



5.5 Figures

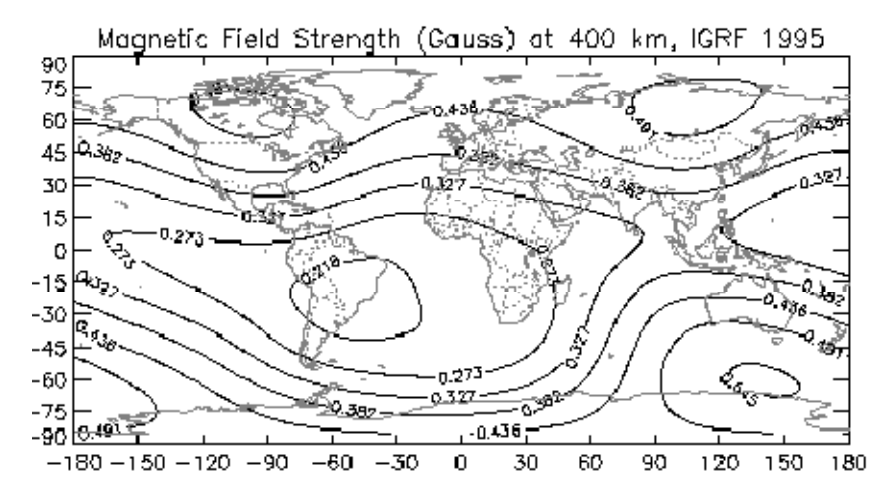


Figure 1: Geomagnetic field strength at 400 km altitude based on IGRF-1995

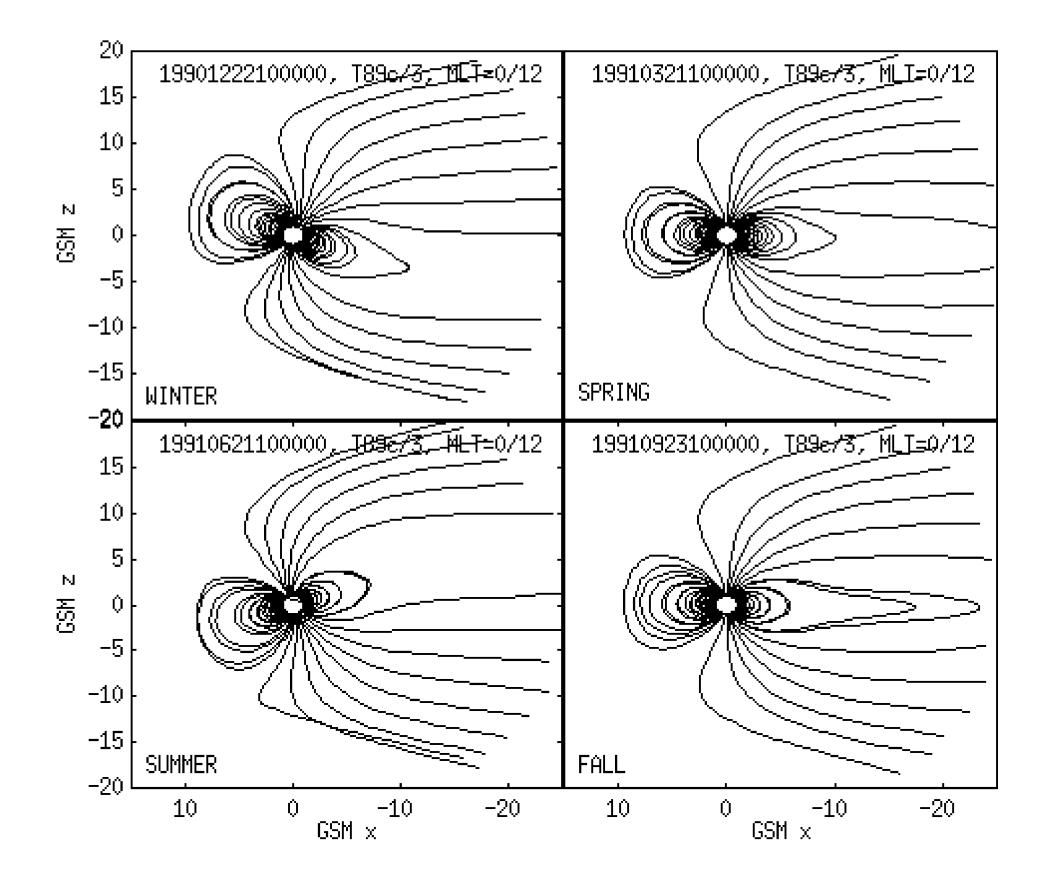
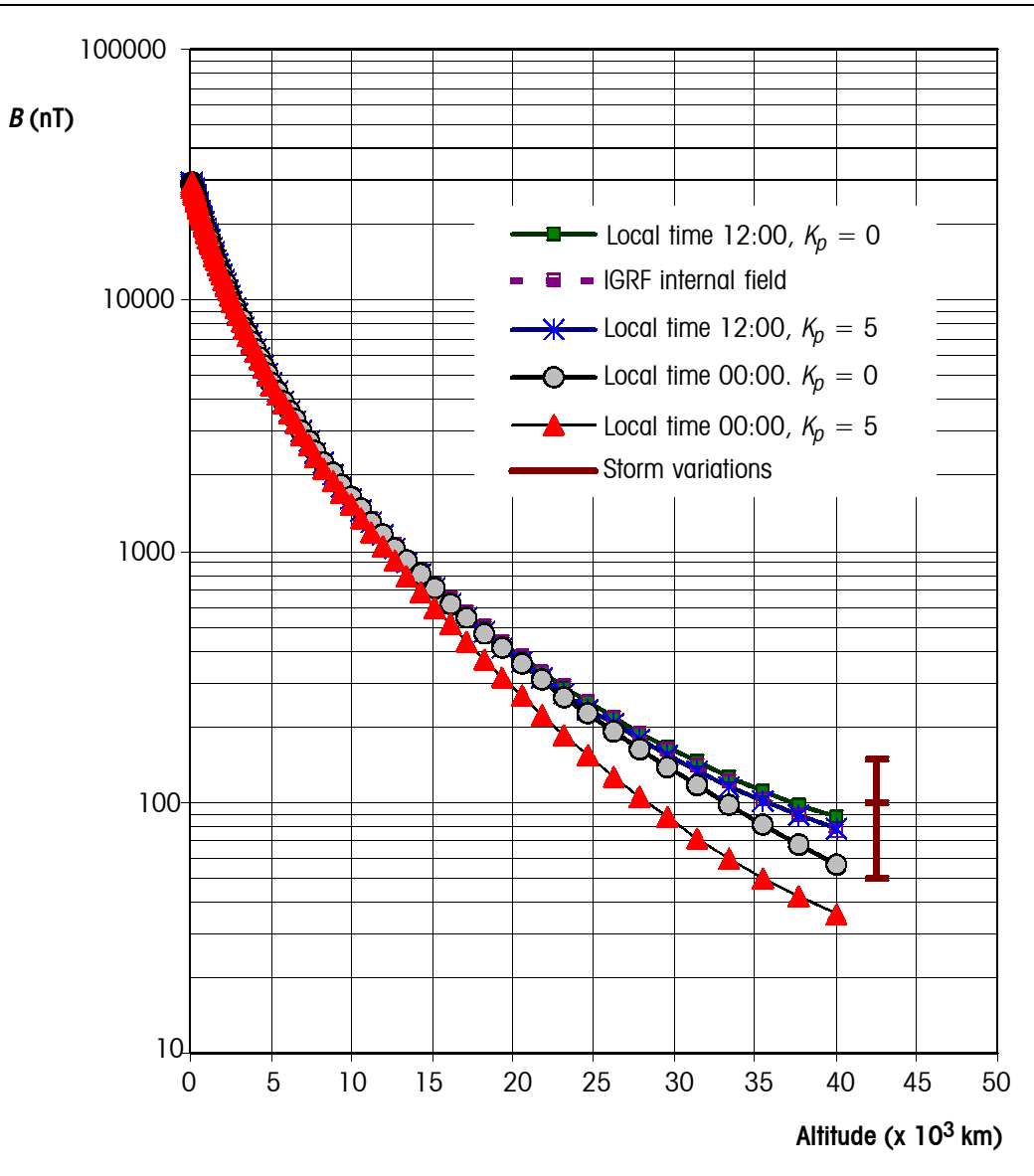


Figure 2: Output from geomagnetic field models showing the diurnal distortion to the field and seasonal variations in the distortion [RD5.8]





Field models include internal-only (IGRF) and external-source models for various conditions. Also shown is the typical dynamic variation at geostationary orbit during disturbed periods.

Figure 3: Variation of the geomagnetic field as a function of altitude

5.6 References

RD5.1 Fraser-Smith, A.C., "Centered and Eccentric Geomagnetic Dipoles and Their Poles, 1600-1985", Rev. Geophys., 25, 1-16, 1987. **RD5.2** Stern D. "Representation of Magnetic Fields in Space", Rev. Geophys. and Space Phys. 14, 199, 1976. RD5.3 Peddie, N.W., "International Geomagnetic Reference Field: The Third Generation", J. Geomag. Geoelectr. 34, 309-326, 1982. **RD5.4** Barton C.E., "Revision of International Geomagnetic Reference Field Released", EOS Transactions of the AGU 77, 16, April 16, 1996. **RD5.5** Hess W.N., "The Radiation Belt and the Magnetosphere", Blaisdell Publ. Co. New York, 1968. **RD5.6** McIlwain C.E., "Co-ordinates for Mapping the Distribution of Geomagnetically Trapped Particles", J. Geophys. Res., 66, 3681, 1961. Hilton H.H., "L Parameter - A New Approximation", J. Geophys. **RD5.7**

Res., 76, 6952, 1971. (Note that this paper contains a typographical error in its expression for a3 of Equation 5.3).



- RD5.8 Rasinkangas R., K. Mursula, T. Ulich, and J. Kangas, "Magnetic field models" in "Space Physics Textbook", http://www.oulu.fi/~spaceweb/textbook/bmodels.html, Oulu University, 1998.
- RD5.9 Tsyganenko N.A., "A Magnetospheric Magnetic Field Model with a Warped Tail Current Sheet", Planet. Space Sci. 37, 5-20, 1989.
- RD5.10 Tsyganenko N.A. and D.P. Stern, "Modeling the Global Magnetic Field of the Large-Scale Birkeland Current Systems", J. Geophys. Res., 101, 27187-27198, 1996.
- RD5.11 Olsen W.P. and K.A. Pfitzer, "A Quantitative Model of the Magnetospheric Magnetic Field", J. Geophys. Res., 79, 3739, 1974.
- RD5.12 Mead G.D. and D.H. Fairfield, "Magnetospheric Mapping with a Quantitative Geomagnetic Field Model", J. Geophys. Res. 80, 523, 1975.
- RD5.13 Stern D.P. and N.A. Tsyganenko, "Uses and Limitations of the Tsyganenko Magnetic Field Models", EOS, Transactions, American Geophysical Union, 73, no. 46, 489, 17 November 1992.
- RD5.14 Pfitzer K.A., "Improved Models of the Inner and Outer Radiation Belts", Phillips Lab Scientific Report PL-TR-91-2187, US Air Force Systems Command, PLGD, Hanscom AFB, Ma., 1991.
- RD5.15 Bass, J.N. and C.E. Jordan, "Models of the External Source Contribution to Magnetospheric Magnetic Fields for CRRES Data Analysis, Scientific Report No. 2", GL-TR-90-0009, Geophysics Laboratory, AFSC, 1990.
- RD5.16 National Geophysical Data Center, "Space Environment Data from NOAA's GOES Satellites", National Geophysical Data Center, Code E/GC2, Dept. 946, 325 Broadway Boulder Co 80303 3328 USA., also Space Physics Interactive Data Resource at http://www.ngdc.noaa.gov:8080/.
- RD5.17 Sibeck D.G., R.E.Lopez and E.C.Roelof, "Solar Wind Control of the Magnetopause Shape, Location and Motion", J. Geophys. Res, 96, p. 5489, 1991.



6

Solar and Earth electromagnetic radiation and indices

6.1 Introduction

A spacecraft in LEO receives electromagnetic radiation from three primary external sources. The largest source is the direct solar flux. The mean value of this solar flux at the mean Sun-Earth distance is called the "solar constant". It is not really a constant but varies by about 3,4 % during each year because of the slightly elliptical orbit of the Earth about the Sun. In addition the amount of radiation emitted by the Sun varies slightly (by about $\pm 0,1$ %) throughout the 11-year solar cycle.

The fraction of incident sunlight that is reflected off a planet is termed albedo. For an orbiting spacecraft the albedo value depends mainly on the sunlit part of the Earth which it can see. Albedo radiation has approximately the same spectral distribution as the Sun and in this Standard albedo refers to the total solar spectrum albedo. Albedo is highly variable across the globe and depends on surface properties and cloud cover. It also depends on the solar zenith angle.

The third source is the Earth infrared radiation. The Earth-emitted thermal radiation has a spectrum of a black body with a characteristic average temperature of 288 K. The Earth infrared radiation also varies across the globe but less than the albedo. It also shows a diurnal variation which is small over the ocean but can amount to $20\,\%$ for desert areas.

Solar and geomagnetic activities are often described by indices. The UV radiation of the Sun, which strongly effects the Earth atmosphere, cannot be directly measured from the ground. But it was found to be strongly correlated with e.g. the sunspot number and the cm wavelength Sun radiation. The widely used 10,7 cm radio flux index $(F_{10,7})$ gives a good measure of the solar UV radiation output which is highly variable over a solar cycle.

Geomagnetic indices typically describe the variation of the geomagnetic field over a certain time period. They provide a measure of the disturbance of the magnetosphere which has direct consequences for the charged particle space environment.

Solar and geomagnetic indices are required as input for upper atmosphere and other models of the near Earth space environment. They are provided for short durations or as long time averages. Predictions for future index values are



usually provided at different confidence levels and they are available for complete solar cycles.

The given data are mainly average values. For detailed thermal analyses or certain special applications more detailed data and models are required which are outside the scope of this Standard. Requirements for thermal analyses are specified in ECSS-E-30: part 1 [RD6.1].

6.2 Solar electromagnetic radiation

6.2.1 Solar constant

The solar constant is defined as the radiation that falls on a unit area of surface normal to the line from the Sun, per unit time, outside the atmosphere, at one astronomical unit (1 AU = average Earth-Sun distance).

The solar constant has an uncertainty of about $\pm 10 \, \text{W/m}^2$ [RD6.2]. The following values for the electromagnetic radiation shall be used:

Solar constant at 1 AU 1371 W/m²

Maximum solar energy flux (winter solstice) 1428 W/m²

Minimum solar energy flux (summer solstice) 1316 W/m²

Solar radiation pressure (100 % reflecting plate) $9.02 \times 10^{-6} \text{ N/m}^2$.

6.2.2 Solar spectrum

The solar spectrum shall be approximated by a black body curve with a characteristic temperature of 5762 K. A space sink temperature of 3 K shall be assumed.

The UV portion (wavelength, λ < 300 nm) of the electromagnetic spectrum is of particular importance in determining effects of solar radiation on the upper atmosphere and on material properties. The integrated irradiance of the near UV electromagnetic radiation flux (180 nm < λ < 400 nm) is approximately 118 W/m². The far UV portion (λ < 180 nm) contributes about 0,023 W/m².

The solar constant changes by only about ± 0.1 % around the mean value over one solar cycle [RD6.3] and is largest during the period of maximum solar activity.

Certain parts of the spectrum are much more variable, both, over the 27-day solar rotation period and over the 11-year solar cycle. This variation ranges from about 50~% for the near UV part to a factor 2 for the UV and far UV portions and can reach orders of magnitude for flare X-rays.

Average and worst case irradiance levels for the high-energy spectrum are summarized in Table 9. The average values were taken from RD6.2.

For design purposes the worst case values of Table 9 shall be used. The fluxes given for flare X-rays are peak values of large flares. For design, one such X-ray flare per week, lasting one hour, shall be assumed.

Annex D contains more details on the solar spectrum.

Table 9: High-energy solar electromagnetic flux

Туре	Wavelength (nm)	Average flux (W/m ²)	$\begin{array}{c} \text{Worst-case} & \text{flux} \\ (\text{W/m}^2) & \end{array}$
Near UV	180-400	118	177
UV	< 180	$2,3 \times 10^{-2}$	$4,6 \times 10^{-2}$
UV	100-150	7.5×10^{-3}	$1,5 \times 10^{-2}$
EUV	10-100	2×10^{-3}	4×10^{-3}
X-rays	1-10	$5 imes 10^{-5}$	1×10^{-4}
Flare X-rays	0,1-1	1×10^{-4}	1×10^{-3}



6.3 Earth electromagnetic radiation

6.3.1 Earth albedo

Albedo is the fraction of sunlight which is reflected off a planet.

The average albedo of the Earth is about 0,3. For short periods the albedo can vary considerably between about 0,05 and 0,6.

For albedo radiation the same spectral shape as for sunlight shall be assumed.

Albedo values are only applicable when a portion of the Earth that is seen by the satellite is sunlit. Albedo values vary with solar zenith angle. The sunlit part of the Earth and the solar zenith angle shall be considered for albedo analyses.

Average albedo values have sometimes to be used with care, e.g. for short duration analyses or for Sun-synchronous orbits where albedo is from specific local times.

Additional information on the variability of the albedo is given in annex D.

6.3.2 Earth infrared

The Earth-emitted thermal radiation is also called "Earth infrared" or "outgoing long wave radiation".

For the Earth infrared radiation a black body spectrum with a characteristic temperature of 288 K shall be assumed.

The average infrared radiation emitted by Earth is $230~W/m^2$. On a short time scale it can vary between $150~W/m^2$ to $350~W/m^2$.

The diurnal variations can amount to about 20~% over desert areas while it is small over oceans.

Additional information on the variability of the Earth infrared radiation is given in annex D.

6.4 Solar and geomagnetic indices

6.4.1 General

Solar and geomagnetic indices are used to describe the activity levels of the Sun and the disturbance of the geomagnetic field. Most activity indices are given for short periods and as long duration averages. They are also used for long range predictions of solar activities. Many space environment models require activity index values as input parameters.

6.4.2 Description of indices

6.4.2.1 Solar activity indices

The most frequently used solar activity indices are the sunspot number, R, and the 10,7 cm wavelength radio flux, $F_{10,7}$. These values, which can be measured at the ground, were found to have a strong correlation with the UV radiation of the Sun, which has a strong influence on the Earth atmosphere.

The $F_{10,7}$ solar activity index gives the flux at a wavelength of 10,7 cm in units of 10^4 Jansky (one Jansky equals 10^{-26} W m⁻² Hz⁻¹).

The $F_{10,7}$ index and the sunspot number, R, are correlated. Averaged (over one month or longer) values can be converted by the following expression:

$$F_{10.7} = 63.7 + 0.728 R + 8.9 \cdot 10^{-4} R^2$$
.



6.4.2.2 Geomagnetic activity indices

Geomagnetic activity indices are used to describe fluctuations of the geomagnetic field. Most widely used planetary indices are K_p and a_p . They are based on 3-hour measurements from 12 ground stations. Values of a_p range from 0 to 400 and they are expressed in units of 2 nT. K_p is essentially the logarithm of a_p . The conversion from K_p to a_p is given in Table 10 (taken from RD6.4). A daily index, A_p , is obtained by averaging the eight values of a_p for each day.

Besides K_p and α_p several other activity indices are used to describe different aspects of the geomagnetic field activity. An overview of the various activity indices and their definitions is given in RD6.5.

Table 10: Conversion from K_p to a_p

K_p	0	0+	1-	10	1+	2-	20	2+	3	30	3+	4-	40	4+
a_p	0	2	3	4	5	6	7	9	12	15	18	22	27	32
Kp	5-	50	5+	6-	60	6+	7-	70	7+	8-	80	8+	9-	90
a_p	39	48	56	67	80	94	111	132	154	179	207	236	300	400

6.4.3 Solar cycle dependence

Table 11 lists the minimum, mean and maximum 13-month smoothed values for $F_{10,7}$ and A_p throughout a mean 11-year solar cycle. These values are taken from RD6.2. The minimum and maximum values are the historical extremes for each point in the cycle and were obtained after the data have been 13-month smoothed and constrained to the mean duration cycle. The standard deviation of the mean cycle length is 1,23 years over the historical record. Figure 4 shows these data graphically.

Table 11: Maximum, mean, and minimum values of the 13-month smoothed 10,7 cm solar radio flux and geomagnetic activity index over the mean solar cycle

Month of		$F_{10,7}$			A_p	
cycle	Max	Mean	Min	Max	Mean	Min
1	73,3	69,6	67,0	11,5	9,5	7,6
2	73,4	69,7	67,0	11,7	9,6	7,7
3	74,0	70,0	67,0	11,8	9,7	7,7
4	74,5	70,4	67,0	11,9	9,7	7,6
5	74,9	70,7	67,0	11,9	9,7	7,4
6	76,2	71,1	67,1	12,2	9,9	7,3
7	78,4	71,6	67,2	12,5	10,0	7,2
8	79,8	72,2	67,3	12,9	10,3	7,2
9	81,5	72,8	67,4	13,3	10,6	7,8
10	84,1	73,6	67,5	14,1	10,9	8,1
11	87,7	74,5	67,7	15,1	11,2	8,2
12	93,4	75,7	67,9	15,7	11,5	8,3
13	97,9	77,0	68,0	15,9	11,8	8,3
14	101,7	78,4	68,0	16,4	12,0	8,3
15	107,7	80,1	68,0	17,4	12,3	8,5
16	114,5	82,0	68,0	18,4	12,7	8,4
17	121,1	84,0	68,1	18,7	12,9	8,5



Table 11: Maximum, mean, and minimum values of the 13-month smoothed 10,7 cm solar radio flux and geomagnetic activity index over the mean solar cycle (continued)

Month of		$F_{10,7}$			A_p	
cycle	Max	Mean	Min	Max	Mean	Min
18	129,1	86,2	68,4	18,8	13,1	8,7
19	137,6	88,5	68,5	18,6	13,2	9,0
20	143,4	91,0	68,6	18,3	13,2	9,3
21	147,6	93,7	68,8	18,1	13,2	9,7
22	151,7	96,3	68,7	18,4	13,4	9,5
23	155,7	98,9	68,8	18,4	13,5	9,3
24	160,1	101,6	69,2	17,6	13,5	9,1
25	164,8	104,4	69,7	17,1	13,6	9,0
26	169,1	107,2	70,1	17,4	13,6	9,1
27	173,0	110,2	70,6	17,4	13,6	9,4
28	177,1	113,2	70,7	18,5	13,8	9,8
29	186,1	116,2	71,3	19,9	14,0	10,0
30	191,5	119,3	72,2	19,9	14,1	10,0
31	194,3	122,0	72,6	19,9	14,1	10,1
32	196,9	124,3	73,3	20,1	14,1	10,4
33	199,6	126,5	73,9	20,4	14,2	10,2
34	204,2	128,6	74,1	20,8	14,2	10,3
35	210,6	131,0	74,4	20,9	14,1	10,6
36	214,8	133,3	74,5	21,0	14,0	10,6
37	217,2	135,6	74,6	21,2	14,0	10,5
38	221,6	137,6	74,5	21,6	14,1	10,4
39	226,9	139,6	74,1	22,1	14,1	10,6
40	229,9	141,4	73,6	$22,\!2$	14,0	10,8
41	231,7	143,2	73,5	21,0	13,7	10,7
42	233,7	144,6	73,6	20,1	13,4	10,4
43	235,6	145,6	74,0	19,8	13,3	10,5
44	238,8	146,7	75,1	19,3	13,3	10,7
45	242,8	147,2	75,8	19,2	13,3	10,8
46	245,2	147,7	76,5	19,0	13,4	11,0
47	244,5	148,1	78,1	18,8	13,3	10,7
48	243,3	148,4	80,1	18,6	13,4	10,8
49	244,7	148,7	82,5	18,6	13,4	10,6
50	245,7	148,2	84,0	18,3	13,4	10,2
51	243,3	146,8	85,5	18,2	13,5	10,6
52	239,4	145,7	87,9	18,7	13,8	11,3
53	235,0	145,1	89,5	19,2	14,1	11,4
54	232,9	144,9	92,2	19,6	14,2	11,3
55	233,3	144,9	93,8	20,3	14,4	11,3
56	233,1	144,7	94,9	21,0	14,6	11,5
57	231,2	144,2	95,0	21,4	14,8	11,6
58	229,1	143,5	94,7	21,2	14,8	11,6
59	228,1	142,7	94,9	20,4	14,7	11,8



Table 11: Maximum, mean, and minimum values of the 13-month smoothed 10,7 cm solar radio flux and geomagnetic activity index over the mean solar cycle (continued)

Month		$F_{10,7}$			A_p	
of cycle	Max	Mean	Min	Max	Mean	Min
60	227,6	142,3	96,5	20,7	14,8	12,1
61	226,7	142,1	97,3	21,9	15,1	12,2
62	225,6	141,3	96,8	22,7	15,2	12,0
63	223,0	140,1	96,0	22,7	15,1	11,6
64	218,6	138,4	96,0	22,3	15,1	11,2
65	215,3	136,8	96,6	21,7	15,1	11,2
66	212,0	135,5	96,7	21,5	15,1	11,2
67	206,9	134,3	95,1	22,1	15,1	11,2
68	204,0	133,0	95,0	23,1	15,5	11,3
69	203,6	131,6	96,3	23,5	15,6	11,3
70	200,4	129,8	96,5	23,4	15,6	11,2
71	196,8	128,3	94,7	23,3	15,7	11,1
72	195,7	127,3	93,6	23,1	15,5	10,8
73	194,8	126,5	93,5	22,2	15,7	10,9
74	191,5	125,1	91,9	22,1	15,6	11,1
75	187,4	123,5	88,7	$22,\!2$	15,6	11,7
76	182,9	122,3	86,6	22,5	15,8	11,6
77	178,6	121,5	87,8	22,6	15,9	11,5
78	176,3	120,5	86,5	$22,\!5$	15,8	11,3
79	174,9	119,5	85,9	21,6	15,7	11,3
80	171,1	117,9	85,0	21,0	15,4	11,3
81	164,5	116,3	83,6	21,1	15,2	11,2
82	158,1	114,6	82,3	21,6	15,2	11,2
83	154,4	112,9	81,6	$22,\!2$	15,4	11,4
84	152,7	111,1	81,5	22,0	15,3	11,3
85	150,8	109,5	81,9	22,0	15,2	11,4
86	148,1	108,0	81,6	22,2	15,0	11,3
87	145,0	106,4	81,4	22,5	14,9	11,3
88	141,1	104,9	80,2	22,8	14,7	11,2
89	137,0	103,4	80,3	23,5	14,7	11,1
90	132,4	101,9	80,0	24,2	14,7	11,0
91	125,4	100,3	78,9	24,7	14,8	11,3
92	119,5	98,9	77,6	25,0	14,8	11,3
93	118,4	97,7	76,6	24,9	14,8	11,2
94	118,7	96,6	74,8	24,5	14,8	11,4
95	119,4	95,6	74,0	23,6	14,7	11,6
96	119,8	94,8	73,4	22,8	14,7	11,3
97	119,0	93,9	73,2	22,1	14,7	11,1
98	117,7	92,8	73,1	21,8	14,8	11,1
99	116,4	91,8	72,7	21,4	14,8	11,2
100	114,6	90,6	71,7	21,1	14,8	11,2
101	110,8	89,6	71,1	20,5	14,7	10,5



Table 11: Maximum, mean, and minimum values of the 13-month smoothed 10,7 cm solar radio flux and geomagnetic activity index over the mean solar cycle (continued)

Month		$F_{10,7}$			A_p	
of cycle	Max	Mean	Min	Max	Mean	Min
102	105,4	88,4	70,6	19,7	14,4	9,9
103	103,2	87,3	70,1	19,7	14,3	9,5
104	102,0	86,5	69,9	19,8	14,1	9,2
105	100,0	85,7	70,0	19,5	14,0	9,0
106	98,2	84,8	69,9	19,1	13,8	8,9
107	96,6	83,6	69,7	18,6	13,8	8,8
108	94,6	82,5	69,5	17,9	13,8	8,7
109	93,8	81,8	69,4	17,0	13,7	8,7
110	92,7	81,1	69,3	16,5	13,6	8,8
111	92,0	80,3	69,0	16,7	13,5	8,9
112	91,8	79,6	68,8	16,9	13,4	9,0
113	91,4	78,9	68,5	17,1	13,3	9,0
114	90,8	78,2	68,2	17,4	13,3	9,0
115	90,1	77,5	68,2	17,4	13,1	9,0
116	89,1	76,9	68,2	17,6	12,9	9,2
117	88,2	76,4	68,2	17,4	12,7	9,3
118	87,0	75,9	68,3	16,9	12,5	9,2
119	85,4	75,3	68,3	16,1	12,2	9,1
120	83,2	74,8	68,3	14,7	11,8	9,1
121	80,5	74,2	68,3	13,6	11,5	9,1
122	78,5	73,5	67,9	13,7	11,2	8,9
123	77,6	72,9	67,6	13,4	10,9	8,5
124	77,1	72,3	67,4	13,0	10,6	8,1
125	76,9	72,0	67,4	12,7	10,5	8,0
126	76,7	71,6	67,2	12,4	10,3	8,0
127	76,5	71,3	67,1	11,7	10,1	8,0
128	76,2	70,9	67,0	11,2	9,9	8,0
129	75,2	70,6	67,0	11,0	9,8	7,9
130	74,2	70,3	67,0	10,9	9,1	7,2
131	74,0	70,1	67,0	11,1	9,2	7,4
132	73,5	69,9	67,0	11,4	9,4	7,6

6.4.4 Reference index values

The reference index values shown in Table 12 for low, mean and high solar and geomagnetic activities shall be used. The long-term values apply for monthly mean or longer term averaged values. They shall also be used for periods between 1 day and 1 month.

The short duration high values apply for periods of 1 day or less. They shall be used to assess the maximum short-term variations of environmental properties (e.g. atmospheric density fluctuations). Annex D contains some historical data on the variability of these indices.



Table 12: Reference index values

		Long-term		Short-term
	Low	Mean	High	High
$F_{10,7}$	70	140	250	380
A_{p}	0	15	25	300

6.4.5 Tailoring guidelines

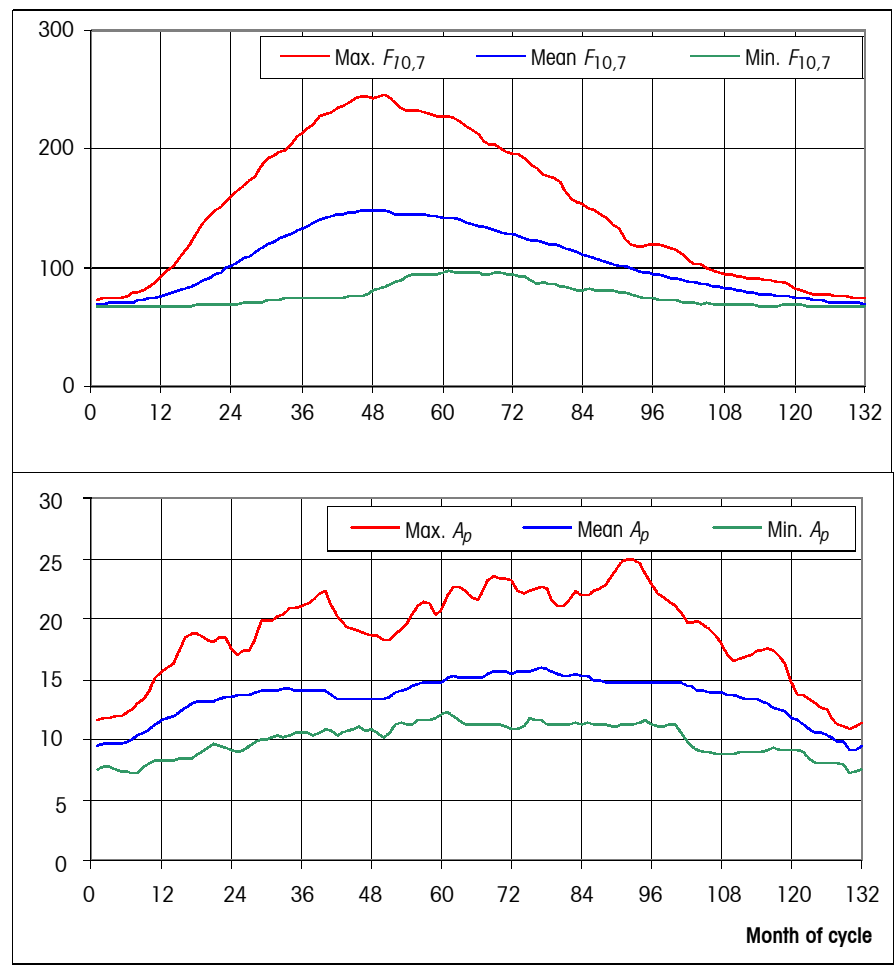
For design purposes the worst case activity values shall be used. These can be the high or low values, depending on the effect to be studied.

Depending on the case to be analysed either the constant reference data in subclause 6.4.4 (to get a typical or maximum value) or the solar cycle data in 6.4.3 (to analyse a longer mission or to obtain the activity prediction for a specific future date) shall be used.

The solar cycle activity in Table 11 can be extended by repetition of the 11-year cycle.

August 1996 shall be assumed as start of cycle 23 (month 1 of Table 11).

6.5 Figures



See description in text.

Figure 4: Standard predictions of solar and geomagnetic activity during a cycle



6.6 References

- RD6.1 "European Cooperation for Space Standardization, Mechanical Engineering Thermal Control", ECSS-E-30 part 1.
- RD6.2 "Natural Orbital Environment Guidelines for Use in Aerospace Vehicle Development", B.J. Anderson, editor and R.E. Smith, compiler; NASA TM 4527, chapters 6 and 9, June 1994.
- RD6.3 Willson R.C. and H.S. Hudson, "The Sun's luminosity over a complete solar cycle", Nature, Vol. 351, pp 42-44, May 1991.
- RD6.4 Menvielle M. and A. Berthelier, "The K-derived Planetary Indices: Description and Availability", Rev. Geophys., 29, 3, pp 415-432, August 1991.
- RD6.5 "SESC Glossary of Solar-Terrestrial Terms", NOAA-USAF Space Environment Services Center, Boulder, 1988 (revised 1992).



 $(This\ page\ is\ intentionally\ left\ blank)$

7

The neutral Earth atmosphere

7.1 Introduction

A good knowledge of temperature, total density, concentrations of gas constituents, and pressure can be important for many space missions in the low-Earth orbit regime (LEO), below 1000 km altitude. Aerodynamic forces due to the orbital motion of a satellite through a rarefied gas with superimposed winds are required to be known for orbit maintenance planning, for sizing of the propulsion system, for attitude controller design, and for the estimation of accelerations acting on sensitive payloads.

Also surface corrosion due to atomic oxygen impingement shall be assessed to predict the degradation of sensitive coatings. Atomic oxygen reactions around a spacecraft can also lead to "vehicle glow".

7.2 Recommended reference model

Due to the large underlying set of supporting measurement data, the large temporal and spatial distribution of these data, the good fit of these data, and the flexible mathematical formulation of the model, the MSISE-90 atmosphere [RD7.1] shall be adopted as reference (corresponding to CIRA-86, the COSPAR International Reference Atmosphere, described in RD7.2 for altitudes above 120 km).

MSISE-90 determines temperature, density, and number concentrations of the major constituents from ground to exospheric altitudes as a function of seven atmospheric state parameters. Other current and historic atmosphere models are mentioned in the informative annex. For horizontal winds the HWM-93 model shall be adopted (Horizontal Wind Model 1993, based on RD7.3). It provides north and east wind components as a function of the same parameters used by MSISE-90.

Annex E contains information on other models.

7.3 Structure of the Earth atmosphere

The Earth atmosphere can be broadly divided into three distinct regimes:

- the homosphere which comprises the troposphere (0 km to 12 km altitude), the stratosphere (12 km to 50 km), and the mesosphere (50 km to 90 km);
- the thermosphere which extends from about 90 km altitude to 250 km or 400 km (depending on solar and geomagnetic activity levels);
- the exosphere which begins at the top of the thermosphere and extends into space.



The homosphere, due to vertical winds and turbulent mixing, has a nearly uniform composition of about $78,1~\%~N_2,\,20,9~\%~O_2,\,$ and 0,9~%~Ar. Its temperature profile shows alternating gradients with a local minimum at the tropopause (218 K), a local maximum at the stratopause (280 K), and another local minimum at the mesopause ($\approx 150~\rm K$).

In the thermosphere, starting at the turbopause near 105 km, vertical mixing processes become less significant, and diffusion under the influence of gravitation and temperature gradients determines the concentration profiles with altitude of the major constituents N2, N, O2, O, He, H, and Ar. The thermospheric temperature profile starts off with a nearly constant value at the turbopause and attains an asymptotic limit T_{∞} at the thermopause (between 250 km and 400 km). Both the thermopause altitude and the thermospheric temperature T_{∞} are depending on the energy input into the heterosphere. These inputs are primarily due to EUV radiation from the Sun and its absorption by atomic oxygen, due to Joule heating caused by charged particles which precipitate into the atmosphere at auroral zones, due to photo dissociation, and due to re-combination processes. Locally, T_{∞} can attain values between 600 K and 2000 K for extremely low and extremely high solar activity levels. Upwards from 400 km the mean free path length of molecules increases to a level at which the light constituent H (which is a major contributor at these altitudes) may exceed the Earth escape velocity and exit the system (hence the term "exosphere").

7.4 Atmospheric state parameters

Satellite drag data from orbit determinations, on-orbit mass spectrometers, accelerometers, sounding rockets, and ground-based incoherent scatter radars provide a wealth of information on the composition, temperature, and variability of the heterosphere, particularly between 150 km and 700 km altitude. Measurement data reveal that temperature, composition, pressure, and total density of the Earth atmosphere change with the following parameters:

- *h*, in km, geodetic altitude;
- ϕ , in ° or rad, geodetic latitude;
- t_{ls} , in h, local solar time;
- t_{ut} , in h, universal time, or alternatively θ , in $^{\circ}$ or rad, geographic longitude;
- t_d , in d, day of the current year (counting from Jan. 1);
- $F_{10,7}$, in 10^{-22} W m⁻² Hz⁻¹ (= 10^4 Jansky) the daily 10,7 cm solar flux index (mostly used from the previous day);
- $(F_{10,7})_{avg}$, in 10^{-22} W m⁻² Hz⁻¹, a mean solar flux index (mostly a running mean over the previous three rotations of the Sun, corresponding to 81 days);
- $A_p \in [0, 400]$, daily mean geomagnetic index, or alternatively $K_p \in [0, 10]$, quasi-logarithmic daily mean geomagnetic index, or alternatively

 $k_p \in [0, 10]$, 3-hourly quasi-logarithmic geomagnetic indices for one day.

The parameters t_{ls} , t_{ut} , and θ are interrelated. In order to be consistent, they shall obey the relation

$$\theta$$
 (°) = 15 × [t_{ls} (h) - t_{ut} (h)].

The solar activity in terms of the 10,7 cm radio flux $F_{10,7}$ and the corresponding Sun-spot number (R) follow a long-periodic 11-year solar cycle with a superimposed 27-day cycle due to the rotation of the Sun. Data histories of solar and geomagnetic activities are shown in clause 6 and annex D. The forecast of the actual level of the daily $F_{10,7}$ and geomagnetic A_p index is difficult and associated with considerable uncertainties.



If the atmospheric state parameters are well known, then the total air density, comprising activity dependent variations (with $(F_{10,7})_{avg}$, $F_{10,7}$ and A_p or k_p), diurnal variations (with t_{ls} and ϕ), longitudinal-latitudinal variations (with t_{ut} and ϕ) and seasonal-latitudinal variations (with t_d and ϕ) of the heterosphere can be modelled with an r.m.s. accuracy of $\pm 10~\%$ to 15 % for the MSISE-90 atmosphere model [RD7.1] which shall be the adopted ECSS reference for both homospheric and heterospheric altitudes.

7.5 Temperature, composition, and density model of the Earth heterosphere

In the heterosphere, well above 90 km, one can assume that the constituents are in diffusive equilibrium with no vertical mixing, and that concentration profiles develop for each constituent independently under the influence of the Earth gravity and thermal diffusion.

$$\frac{1}{n_i}\frac{dn_i}{dh} + \frac{1}{H_i} + \frac{1 + \alpha_i}{T}\frac{dT}{dh} = 0$$
 (7.1)

where

 $i = 1, \dots, 7 \text{ refers to } N_2, O_2, Ar, O, He, H, \text{ and } N;$

h is the geodetic altitude, km;

T is the local atmospheric temperature, K;

 n_i is the particle concentration (number density) of species i, $1/m^3$;

 H_i is the concentration scale height of species i, km;

 α_i is the thermal diffusion coefficient for species i ($\alpha_i = -0.4$ for H and He, and 0.0 otherwise).

The altitude profile of the temperature T(h), which is required in equation (7.1), can be well approximated by an exponential function which reaches an asymptotic limit T_{∞} (exospheric temperature) at the thermopause.

$$T = T_{\infty} - (T_{\infty} - T_{120}) \exp[-s(h - h_{120})]$$
 (7.2)

where

() $_{\infty}$ are the conditions at the thermopause (start of the exosphere);

()₁₂₀ are the conditions at geodetic altitude 120 km;

s is the temperature gradient parameter, 1/km.

Using expansions in the parameter c, equations (7.1) and (7.2) can be rewritten as explicit, analytical approximations of the altitude profiles in terms of the following expressions.

$$n_{i} = n_{i, 120} \exp(-\sigma \gamma_{i} z) \left[\frac{(1-c)}{(1-c \exp(-\sigma z))} \right]^{1+a_{i}+\gamma_{i}}$$
 (7.3)

$$T = T_{\infty}[1 - c \exp(-\sigma z)] \tag{7.4}$$

where

 $z = (h - h_{120})(R_E + h_{120})/(R_E + h)$, geopotential altitude parameter, km;

 $c = 1 - T_{120}/T$;

 $T_{\infty} = T_{\infty}(h, \phi, t_{ls}, t_{ut}, t_d, (F_{10,7})_{avg}, F_{10,7}, A_p);$

 $T_{120} = T_{120}(h, \phi, t_{ls}, t_{ut}, t_d, (F_{10,7})_{avg}, F_{10,7}, A_p);$

 $n_{i,\,120} = n_{i,120}\,(h,\phi,\,t_{ls},\,t_{ut},\,t_{d},\,(F_{10,7})_{avg},\,F_{10,7},\,A_{p});$

 $\sigma = s + (R_E + h_{120})^{-1}$, temperature gradient parameter, 1/km;

 $s = s(h, \phi, t_{ls}, t_{ut}, t_d, (F_{10,7})_{avg}, F_{10,7}, A_p);$

 γ_i = 1/($H_i \sigma$), dimensionless diffusion parameter;



 H_i = $RT/(M_ig)$, the concentration scale height of species i, m;

 M_i = 28, 32, 40, 16, 4, 1, and 14 for N_2 , O_2 , Ar, O, He, H and N, molar masses, respectively, kg/kmol;

 R_E = 6357 km, normalizing Earth radius;

g = 9,806 m/s², reference gravity acceleration constant;

 $R = 8314 \text{ J kmol}^{-1}\text{K}^{-1}$, the universal gas constant.

The air density is then determined from the mass-weighted, normalized concentrations, and the total pressure can be expressed as the sum of the partial pressures of the constituents.

$$\rho = \frac{1}{N_A} \sum_{i=1}^{7} n_i M_i \tag{7.5}$$

$$p = \sum_{i=1}^{7} p_i = kT \sum_{i=1}^{7} n_i \tag{7.6}$$

where

 ρ is the total density, kg/m³;

p is the pressure, N/m^2 ;

 $k = 1,3807 \times 10^{-23} \text{ J/K}, \text{ the Boltzmann constant;}$

 $N_A = \approx 6,022 \times 10^{23} \,\mathrm{mol}^{-1}$, Avogadro's number.

For aerodynamic calculations in a rarefied gas, in particular below altitudes of 200 km, the mean free path length, the speed of sound, and the dynamic viscosity are important. They can be approximated with good accuracy from

$$\frac{1}{L} = \sqrt{2}\pi d_{avg}^2 \frac{p}{kT} \tag{7.7}$$

$$a = \sqrt{\kappa \frac{p}{\rho}} \tag{7.8}$$

$$\mu = \frac{2}{3} L \rho a \sqrt{\frac{2}{\pi \kappa}} \tag{7.9}$$

where

L is the mean free path of a molecule, m;

 μ is the dynamic viscosity, kg s⁻¹ m⁻¹;

a is the speed of sound, m/s;

 κ = 1,44, the ratio of specific heats (in an N_2 dominated environment);

 d_{ans} = 3,62 × 10⁻¹⁰ m, the mean collision diameter (for N_2).

All quantities on the right-hand sides of equations (7.3) and (7.4) are functions of the above listed seven atmospheric state parameters, with model coefficients which need to be fitted to measurement data. For the quality of a model it is essential that an adequate spatial and temporal distribution of measurement data is available in order to fit altitude profiles and their variation with daily, seasonal, and solar cycle periods. Due to sparse measurement data atmosphere models tend to be less reliable at altitudes below 150 km, above 700 km, and for extreme excursions of solar and geomagnetic activities.

According to equations (7.1) and (7.3), the changes of the number densities n_i with altitude are mainly driven by the hydrostatic equation which yields an exponential decrease. The logarithmic slope of this decrease, which is described by H_i^{-1} , becomes steeper with higher molar masses M_i and lower exospheric temperatures T_{∞} (see Figure 8). The dominant constituents with increasing altitude are consequently N_2 , O, He, and H, with varying altitude regions of dominance



according to activity levels (which mainly determine T_{∞}). Also the position of the diurnal density maximum is governed by the molar masses. Maxima occur near the sub-solar position with a time lag of 3,5 hrs for N_2 and O, and with a time lag of up to 12 hrs for the light weight species He and H. Due to the maximum EUV absorption by atomic oxygen, the diurnal density variation reaches its highest amplitudes of $\rho_{max}(h)/\rho_{min}(h)\approx 10$ near h=600 km, where O is the dominant species. At these altitudes the density variation with solar activity also attains its maximum amplitude with changes by up to two orders of magnitude between extremes of the solar cycle (see Tables 13 to 15 and Figures 5 to 7, discussed later).



Table 13: MSISE-90 altitude profiles of temperature T, total density ρ , pressure p, mean molecular weight M and density scale height H for low activities

	ř		747	in alla acilis	ity scare	ileigiit i	delisity scale lieight it for low activities	activiti	2	-	-	
h (km)	T (K)	$ ho ({f kg/m^3})$	$p(\mathrm{N/m^3})$	M (kg/mol)	H (km)	$\mathbf{n}_{N_2}~(/\mathbf{m}^3)$	$\mathbf{n}_o~(/\mathbf{m}^3)$	\mathbf{n}_{o_2} $(/\mathbf{m}^3)$ \mathbf{n}_{He} $(/\mathbf{m}^3)$		$\left \mathbf{n}_{Ar} \; (/\mathbf{m}^3) \right \mathbf{n}_H \; (/\mathbf{m}^3)$	$\mathbf{n}_{H} \; (/\mathbf{m}^{3})$	$\mathbf{n}_N \; (/\mathbf{m}^3)$
0	300,2511	1,17E+00	1,01E+05	28,9502	11,4737	1,90E+25	1	5,09E+24	1,27E+20	2,27E+23	ı	1
20	206,2085	9,48E-02	5,62E+03	28,9502	5,5843	1,54E+24	ı	4,14E+23	1,03E+19	1,84E+22	1	1
40	257,6979	4,07E-03	3,01E+02	28,9502	7,2030	6,62E+22	ı	1,78E+22	4,44E+17	7,91E+20	1	1
09	244,1212	3,31E-04	2,32E+01	28,9502	8,1940	5,38E+21	1	1,44E+21	3,61E+16	6,44E+19	ı	•
80	203,1065	1,69E-05	9,81E-01	29,1353	6,1010	2,62E+20	3,93E+18	7,04E+19	7,21E+13	1,36E+19	1,27E+12	1,20E+16
100	168,7219	5,77E-07	2,89E-02	28,0036	5,0095	1,00E+19	6,58E+17	1,64E+18	4,92E+13	1,18E+17	1,25E+12	2,57E+15
120	356,8669	1,70E-08	1,92E-03	26,3948	7,9781	2,92E+17	6,34E+16	3,22E+16	2,11E+13	1,05E+15	7,23E+11	3,02E+14
140	545,8594	2,96E-09	5,37E-04	25,0665	15,2801	4,79E+16	1,88E+16	4,33E+15	1,34E+13	9,48E+13	5,33E+11	9,88E+13
160	630,0652	9,65E-10	2,13E-04	23,7884	20,2988	1,44E+16	8,89E+15	1,12E+15	1,06E+13	1,80E+13	4,71E+11	5,03E+13
180	667,8662	3,90E-10	9,62E-05	22,5037	23,7416	5,19E+15	4,85E+15	3,52E+14	8,91E+12	4,32E+12	4,39E+11	2,94E+13
200	684,9187	1,75E-10	4,70E-05	21,2516	26,3234	2,02E+15	2,80E+15	1,20E+14	7,70E+12	1,14E+12	4,19E+11	1,81E+13
220	692,6487	8,47E-11	2,43E-05	20,0935	28,6112	8,17E+14	1,66E+15	4,28E+13	6,73E+12	3,13E+11	4,03E+11	1,15E+13
240	696,1697	4,31E-11	1,31E-05	19,0789	30,7226	3,36E+14	9,97E+14	1,55E+13	5,91E+12	8,82E+10	3,89E+11	7,33E+12
260	697,7811	2,30E-11	7,31E-06	18,2300	32,6731	1,40E+14	6,03E+14	5,70E+12	5,21E+12	2,52E+10	3,77E+11	4,72E+12
280	698,5220	1,27E-11	4,20E-06	17,5402	34,6129	5,87E+13	3,67E+14	2,11E+12	4,60E+12	7,29E+09	3,65E+11	3,06E+12
300	698,8644	7,22E-12	2,47E-06	16,9830	36,3499	2,48E+13	2,24E+14	7,88E+11	4,07E+12	2,13E+09	3,54E+11	1,99E+12
320	699,0233	4,21E-12	1,48E-06	16,5214	37,6859	1,05E+13	1,37E+14	2,96E+11	3,60E+12	6,26E+08	3,43E+11	1,29E+12
340	699,0973	2,50E-12	9,01E-07	16,1147	39,0274	4,49E+12	8,44E+13	1,12E+11	3,19E+12	1,85E+08	3,33E+11	8,45E+11
360	699,1320	1,51E-12	5,57E-07	15,7219	40,0512	1,92E+12	5,20E+13	4,25E+10	2,82E+12	5,53E+07	3,23E+11	5,53E+11
380	699,1483	9,20E-13	3,50E-07	15,3028	40,9778	8,30E+11	3,22E+13	1,63E+10	2,50E+12	1,66E+07	3,13E+11	3,63E+11
400	699,1561	5,68E-13	2,23E-07	14,8185	41,9519	3,60E+11	2,00E+13	6,25E+09	2,22E+12	5,04E+06	3,04E+11	2,39E+11
420	699,1597	3,54E-13	1,45E-07	14,2332	42,8975	1,57E+11	1,24E+13	2,42E+09	1,97E+12	1,54E+06	2,95E+11	1,58E+11
440	699,1615	2,23E-13	9,61E-08	13,5181	43,8193	6,86E+10	7,74E+12	9,40E+08	1,75E+12	4,72E+05	2,87E+11	1,04E+11
460	699,1623	1,42E-13	6,54E-08	12,6581	45,1370	3,02E+10	4,84E+12	3,68E+08	1,56E+12	1,46E+05	2,78E+11	6,92E+10
480	699,1627	9,20E-14	4,59E-08	11,6594	46,6954	1,33E+10	3,04E+12	1,45E+08	1,39E+12	4,55E+04	2,70E+11	4,60E+10
200	699,1629	6,03E-14	3,32E-08	10,5547	48,3084	5,92E+09	1,91E+12	5,72E+07	1,24E+12	1,43E+04	2,63E+11	3,07E+10
* Concer	* Concentrations of no	nrı	and ny are computed for	$\frac{1}{2}$ And $\frac{1}{2}$ by $\frac{1}{2}$	ű						=	

* Concentrations of n_0 , n_H , and n_N are computed for $h \ge 80 \text{ km}$



Table 13: MSISE-90 altitude profiles of temperature T, total density ρ , pressure p, mean molecular weight Mand density scale height H for low activities (continued)

				٠,)		j					
<i>h</i> (km)	T (K)	$ ho (kg/m^3)$	$p(N/m^3)$	M (kg/mol)	H (km)	$\mathbf{n}_{N_2}~(/\mathbf{m}^3)$	$\mathbf{n}_o~(/\mathbf{m}^3)$	$\mathbf{n}_{o_2}~(/\mathbf{m}^3)$	$\mathbf{n}_{He} \ (/\mathbf{m}^3)$	$\left \mathbf{n}_{o_2}^{}\left(/\mathbf{m}^3\right)\right _{\mathbf{n}_{He}^{}\left(/\mathbf{m}^3\right)}\right _{\mathbf{n}_{Ar}^{}\left(/\mathbf{m}^3\right)}\left \mathbf{n}_{H}^{}\left(/\mathbf{m}^3\right)\right _{\mathbf{n}_{H}^{}\left(/\mathbf{m}^3\right)}$	$\mathbf{n}_{H} \; (/\mathbf{m}^{3})$	$\mathbf{n}_N \ (/\mathbf{m}^3)$
520	699,1630	4,03E-14	2,49E-08	9,4006	50,8992	2,64E+09	1,20E+12	2,27E+07	1,10E+12	4,50E+03	2,55E+11	2,05E+10
540	699,1630	2,75E-14	1,94E-08	8,2657	53,8186	1,18E+09	7,61E+11	9,09E+06	9,82E+11	1,43E+03	2,48E+11	1,37E+10
260	699,1631	1,93E-14	1,55E-08	7,2141	58,2364	5,33E+08	4,83E+11	3,65E+06	8,76E+11	4,58E+02	2,41E+11	9,21E+09
580	699,1631	1,39E-14	1,28E-08	6,2904	63,5906	2,41E+08	3,07E+11	1,48E+06	7,82E+11	1,48E+02	2,34E+11	6,19E+09
009	699,1631	1,03E-14	1,09E-08	5,5149	71,0934	1,10E+08	1,95E+11	5,99E+05	6,99E+11	4,78E+01	2,28E+11	4,18E+09
620	699,1631	7,90E-15	9,40E-09	4,8864	79,7750	5,01E+07	1,25E+11	2,45E+05	6,25E+11	1,56E+01	2,22E+11	2,82E+09
640	699,1631	6,24E-15	8,27E-09	4,3891	90,0817	2,30E+07	8,00E+10	1,00E+05	5,59E+11	5,12E+00	2,15E+11	1,91E+09
099	699,1631	5,06E-15	7,36E-09	4,0012	102,0265	1,06E+07	5,14E+10	4,14E+04	5,00E+11	1,69E+00	2,10E+11	1,30E+09
089	699,1631	4,21E-15	6,62E-09	3,6999	115,2614	4,89E+06	3,31E+10	1,72E+04	4,48E+11	5,63E-01	2,04E+11	8,82E+08
200	699,1631	3,58E-15	6,00E-09	3,4648	129,9408	2,27E+06	2,13E+10	7,15E+03	4,02E+11	1,89E-01	1,98E+11	6,01E+08
720	699,1631	3,09E-15	5,48E-09	3,2789	142,8583	1,06E+06	1,38E+10	2,99E+03	3,60E+11	6,35E-02	1,93E+11	4,11E+08
740	699,1631	2,70E-15	5,02E-09	3,1289	156,2294	4,98E+05	8,96E+09	1,26E+03	3,23E+11	2,15E-02	1,88E+11	2,81E+08
092	699,1631	2,39E-15	4,63E-09	3,0049	168,9813	2,34E+05	5,82E+09	5,32E+02	2,90E+11	7,33E-03	1,83E+11	1,93E+08
780	699,1631	2,13E-15	4,28E-09	2,8996	181,3580	1,11E+05	3,80E+09	2,26E+02	2,61E+11	2,52E-03	1,78E+11	1,33E+08
800	699,1631	1,91E-15	3,96E-09	2,8075	188,1991	5,26E+04	2,48E+09	9,65E+01	2,35E+11	8,68E-04	1,73E+11	9,15E+07
820	699,1631	1,73E-15	3,68E-09	2,7249	199,7376	2,51E+04	1,62E+09	4,14E+01	2,11E+11	3,01E-04	1,69E+11	6,32E+07
840	699,1631	1,56E-15	3,43E-09	2,6492	208,2405	1,20E+04	1,07E+09	1,78E+01	1,90E+11	1,05E-04	1,65E+11	4,37E+07
098	699,1631	1,42E-15	3,21E-09	2,5784	212,0086	5,77E+03	7,02E+08	7,72E+00	1,71E+11	3,69E-05	1,60E+11	3,03E+07
880	699,1631	1,30E-15	3,00E-09	2,5113	221,2246	2,79E+03	4,63E+08	3,36E+00	1,54E+11	1,31E-05	1,56E+11	2,11E+07
006	699,1631	1,18E-15	2,81E-09	2,4470	223,6053	1,35E+03	3,06E+08	1,47E+00	1,39E+11	4,64E-06	1,52E+11	1,47E+07
*	* Concentrations of n	2	ond no one one	2d for h = 20 lzw	3							

^{*} Concentrations of n_O, n_H, and n_N are computed for $h \ge 80 \text{ km}$



Table 14: MSISE-90 altitude profiles of temperature T, total density ρ , pressure p, mean molecular weight M and density scale height H for mean activities

			2 747	n and density scale neight n for mean activities	ry scare.	neigne 11	ioi illea	II activit	ICS			
h (km)	T (K)	$ ho ({ m kg/m^3})$	p (N/m ³)	M (kg/mol)	H (km)	$\left.\mathbf{n}_{N_2}^{} \; \left(/\mathbf{m}^3 \right) \right _{\mathbf{n}_O}^{} \; \left(/\mathbf{m}^3 \right)^{}$	$\mathbf{n}_o~(/\mathbf{m}^3)$	$\left \mathbf{n}_{o_2}^{}\left(/\mathbf{m}^3\right)\right _{\mathbf{n}_{He}^{}\left(/\mathbf{m}^3\right)}$	$\mathbf{n}_{He} (/\mathbf{m}^3)$	$\mathbf{n}_{Ar} \ (/\mathbf{m}^3) \left \mathbf{n}_H \ (/\mathbf{m}^3) \right $		$\mathbf{n}_N \ (/\mathbf{m}^3)$
0	300,2511	1,17E+00	1,01E+05	28,9502	11,4721	1,90E+25	1	5,09E+24	1,27E+20	2,27E+23	ı	1
20	206,2085	9,49E-02	5,62E+03	28,9502	5,5842	1,54E+24	1	4,14E+23	1,04E+19	1,85E+22	ı	1
40	257,6979	4,07E-03	3,02E+02	28,9502	7,2029	6,62E+22	1	1,78E+22	4,44E+17	7,92E+20	1	1
09	244,1212	3,31E-04	2,32E+01	28,9502	8,1933	5,38E+21	1	1,44E+21	3,61E+16	6,44E+19	ı	1
80	196,3636	1,68E-05	9,45E-01	29,0175	6,1281	2,66E+20	5,36E+18	6,30E+19	9,51E+13	1,40E+19	4,65E+11	2,81E+16
100	184,0160	5,08E-07	2,81E-02	27,7137	5,3926	8,87E+18	7,88E+17	1,28E+18	6,02E+13	1,05E+17	4,27E+11	5,30E+15
120	374,9715	1,80E-08	2,17E-03	25,8745	7,7281	3,02E+17	8,43E+16	2,98E+16	2,69E+13	1,14E+15	2,53E+11	6,86E+14
140	635,5703	3,26E-09	7,03E-04	24,5349	16,3411	5,12E+16	2,44E+16	4,22E+15	1,64E+13	1,13E+14	1,76E+11	2,17E+14
160	787,5532	1,18E-09	3,31E-04	23,4225	23,3363	1,72E+16	1,19E+16	1,25E+15	1,27E+13	2,61E+13	1,50E+11	1,13E+14
180	877,6729	5,51E-10	1,80E-04	22,4106	29,0312	7,29E+15	6,97E+15	4,76E+14	1,07E+13	8,04E+12	1,37E+11	6,96E+13
200	931,2806	2,91E-10	1,05E-04	21,4734	33,5804	3,46E+15	4,44E+15	2,05E+14	9,36E+12	2,85E+12	1,29E+11	4,66E+13
220	963,2701	1,66E-10	6,44E-05	20,6108	37,3389	1,75E+15	2,96E+15	9,42E+13	8,35E+12	1,09E+12	1,24E+11	3,25E+13
240	982,4191	9,91E-11	4,09E-05	19,8292	40,5638	9,12E+14	2,02E+15	4,50E+13	7,55E+12	4,33E+11	1,20E+11	2,33E+13
260	993,9173	6,16E-11	2,66E-05	19,1337	43,3273	4,87E+14	1,41E+15	2,20E+13	6,86E+12	1,78E+11	1,16E+11	1,69E+13
280	1000,8427	3,94E-11	1,77E-05	18,5256	45,9808	2,63E+14	9,87E+14	1,09E+13	6,26E+12	7,40E+10	1,13E+11	1,24E+13
300	1005,0267	2,58E-11	1,20E-05	18,0015	48,3416	1,44E+14	6,97E+14	5,46E+12	5,74E+12	3,13E+10	1,10E+11	9,14E+12
320	1007,5620	1,72E-11	8,20E-06	17,5537	50,2822	7,91E+13	4,95E+14	2,76E+12	5,26E+12	1,33E+10	1,08E+11	6,77E+12
340	1009,1030	1,16E-11	5,69E-06	17,1721	52,2731	4,38E+13	3,53E+14	1,40E+12	4,83E+12	5,73E+09	1,06E+11	5,03E+12
360	1010,0423	7,99E-12	3,98E-06	16,8449	53,9613	2,43E+13	2,52E+14	7,18E+11	4,44E+12	2,48E+09	1,03E+11	3,75E+12
380	1010,6166	5,55E-12	2,81E-06	16,5597	55,6560	1,36E+13	1,81E+14	3,69E+11	4,08E+12	1,08E+09	1,01E+11	2,80E+12
400	1010,9688	3,89E-12	2,01E-06	16,3044	57,1177	7,62E+12	1,30E+14	1,90E+11	3,76E+12	4,72E+08	9,91E+10	2,10E+12
420	1011,1853	2,75E-12	1,44E-06	16,0669	58,4012	4,29E+12	9,35E+13	9,87E+10	3,46E+12	2,08E+08	9,71E+10	1,57E+12
440	1011,3188	1,96E-12	1,04E-06	15,8360	59,4317	2,42E+12	6,74E+13	5,14E+10	3,19E+12	9,18E+07	9,51E+10	1,18E+12
460	1011,4014	1,40E-12	7,55E-07	15,6008	60,4864	1,37E+12	4,87E+13	2,69E+10	2,94E+12	4,08E+07	9,32E+10	8,90E+11
480	1011,4526	1,01E-12	5,53E-07	15,3508	61,5528	7,80E+11	3,53E+13	1,41E+10	2,71E+12	1,82E+07	9,13E+10	6,71E+11
ζ,		r	-	. 01								

* Concentrations of n_O , n_H , and n_N are computed for $h \ge 80 \text{ km}$



Table 14: MSISE-90 altitude profiles of temperature T, total density ρ , pressure p, mean molecular weight M and density scale height H for mean activities (continued)

		'			Q ->>							
h (km)	$T(\mathbf{K})$	$ ho (kg/m^3)$	p (N/m ³)	M (kg/mol)	<i>H</i> (km)	\mathbf{n}_{N_2} $(/\mathbf{m}^3)$	\mathbf{n}_o $(/\mathbf{m}^3)$	\mathbf{n}_{o_2} (/ \mathbf{m}^3)	$\mathbf{n}_{He} (/\mathbf{m}^3)$	\mathbf{n}_{He} $(/\mathbf{m}^3)$ \mathbf{n}_{Ar} $(/\mathbf{m}^3)$ \mathbf{n}_H $(/\mathbf{m}^3)$		$\mathbf{n}_N \ (/\mathbf{m}^3)$
200	1011,4845	7,30E-13	4,07E-07	15,0760	62,4024	4,45E+11	2,56E+13	7,42E+09	2,51E+12	8,16E+06	8,95E+10	5,07E+11
520	1011,5043	5,31E-13	3,03E-07	14,7669	63,4137	2,55E+11	1,86E+13	3,92E+09	2,31E+12	3,68E+06	8,77E+10	3,83E+11
540	1011,5168	3,88E-13	2,27E-07	14,4148	63,9820	1,46E+11	1,36E+13	2,08E+09	2,14E+12	1,67E+06	8,60E+10	2,91E+11
260	1011,5245	2,85E-13	1,71E-07	14,0125	65,3319	8,43E+10	9,90E+12	1,11E+09	1,98E+12	7,58E+05	8,43E+10	2,21E+11
580	1011,5294	2,11E-13	1,31E-07	13,5547	66,4024	4,88E+10	7,24E+12	5,92E+08	1,83E+12	3,46E+05	8,27E+10	1,68E+11
009	1011,5325	1,56E-13	1,01E-07	13,0389	68,1361	2,83E+10	5,30E+12	3,18E+08	1,69E+12	1,59E+05	8,11E+10	1,28E+11
620	1011,5345	1,17E-13	7,89E-08	12,4665	69,7510	1,64E+10	3,89E+12	1,71E+08	1,56E+12	7,33E+04	7,96E+10	9,74E+10
640	1011,5357	8,79E-14	6,24E-08	11,8428	70,9524	9,59E+09	2,86E+12	9,24E+07	1,45E+12	3,40E+04	7,80E+10	7,44E+10
099	1011,5365	6,65E-14	5,01E-08	11,1779	72,9834	5,61E+09	2,11E+12	5,01E+07	1,34E+12	1,58E+04	7,66E+10	5,69E+10
089	1011,5370	5,08E-14	4,07E-08	10,4854	74,8578	3,30E+09	1,55E+12	2,72E+07	1,24E+12	7,38E+03	7,51E+10	4,36E+10
200	1011,5374	3,91E-14	3,36E-08	9,7818	78,5188	1,94E+09	1,15E+12	1,49E+07	1,15E+12	3,46E+03	7,37E+10	3,35E+10
720	1011,5375	3,04E-14	2,82E-08	9,0847	81,5376	1,15E+09	8,49E+11	8,15E+06	1,07E+12	1,63E+03	7,23E+10	2,57E+10
740	1011,5377	2,39E-14	2,39E-08	8,4111	84,7760	6,79E+08	6,30E+11	4,48E+06	9,92E+11	7,73E+02	7,10E+10	1,98E+10
160	1011,5377	1,90E-14	2,06E-08	7,7753	89,4495	4,03E+08	4,68E+11	2,47E+06	9,21E+11	3,67E+02	6,97E+10	1,53E+10
780	1011,5378	1,53E-14	1,79E-08	7,1884	95,5420	2,40E+08	3,48E+11	1,37E+06	8,55E+11	1,75E+02	6,84E+10	1,18E+10
800	1011,5378	1,25E-14	1,58E-08	6,6572	101,1751	1,44E+08	2,59E+11	7,59E+05	7,94E+11	8,40E+01	6,72E+10	9,10E+09
820	1011,5378	1,03E-14	1,40E-08	6,1849	108,3571	8,61E+07	1,93E+11	4,23E+05	7,38E+11	4,04E+01	6,59E+10	7,05E+09
840	1011,5379	8,64E-15	1,26E-08	5,7711	117,4539	5,17E+07	1,45E+11	2,36E+05	6,87E+11	1,95E+01	6,48E+10	5,46E+09
860	1011,5379	7,32E-15	1,14E-08	5,4132	126,1862	3,12E+07	1,08E+11	1,32E+05	6,39E+11	9,48E+00	6,36E+10	4,24E+09
880	1011,5379	6,28E-15	1,04E-08	5,1066	135,5045	1,89E+07	8,12E+10	7,45E+04	5,94E+11	4,62E+00	6,25E+10	3,30E+09
006	1011,5379	5,46E-15	9,47E-09	4,8460	146,5578	1,14E+07	6,10E+10	4,20E+04	5,53E+11	2,26E+00	6,14E+10	2,57E+09
7		п	1-	100 1								Ī

* Concentrations of n_O, n_H, and n_N are computed for $h \ge 80 \text{ km}$



Table 15: MSISE-90 altitude profiles of temperature T, total density ρ , pressure p, mean molecular weight M and density scale height H for extremely high activities

			n aua M	In and density scale height n for extremely high activities	le neigr	10 H 10F 6	xrremer	y nign ac	cuvines			
<i>h</i> (km)	$T\left(\mathbf{K}\right)$	$ ho ({f kg/m^3})$	p (N/m ³)	M (kg/mol)	H (km)	$\left.\mathbf{n}_{N_2}^{}\left(/\mathbf{m}^3\right)\right \mathbf{n}_{o}^{}$	(\mathbf{m}^3)	\mathbf{n}_{o_2} $(/\mathbf{m}^3)$	$\mathbf{n}_{He}~(/\mathbf{m}^3)$	$\mathbf{n}_{Ar}~(/\mathbf{m}^3)$	(m/) n _H	$\mathbf{n}_N \ (/\mathbf{m}^3)$
0	300,2511	1,16E+00	9,98E+04	28,9502	11,4728	1,88E+25	1	5,05E+24	1,26E+20	2,25E+23	ı	1
20	206,2085	9,41E-02	5,57E+03	28,9502	5,5843	1,53E+24	1	4,10E+23	1,03E+19	1,83E+22	ı	1
40	257,6979	4,04E-03	2,99E+02	28,9502	7,2035	6,56E+22	ı	1,76E+22	4,40E+17	7,85E+20	1	1
09	244,1212	3,28E-04	2,30E+01	28,9502	8,1920	5,34E+21	1	1,43E+21	3,58E+16	6,38E+19	1	•
80	172,2146	1,68E-05	8,42E-01	28,5290	6,1265	2,80E+20	1,43E+19	4,32E+19	2,20E+14	1,62E+19	1,38E+10	5,75E+17
100	297,3338	2,78E-07	2,63E-02	26,1997	7,3856	4,74E+18	1,10E+18	4,42E+17	9,58E+13	6,03E+16	8,77E+09	5,69E+16
120	430,8385	2,34E-08	3,55E-03	23,6456	6,5809	3,48E+17	2,11E+17	2,35E+16	5,57E+13	1,69E+15	6,48E+09	1,28E+16
140	875,9174	4,93E-09	1,61E-03	22,3209	20,0481	6,52E+16	5,98E+16	3,84E+15	3,17E+13	2,10E+14	4,09E+09	3,89E+15
160	1143,5426	2,23E-09	9,90E-04	21,4577	31,2463	2,69E+16	3,22E+16	1,45E+15	2,47E+13	6,63E+13	3,41E+09	2,19E+15
180	1314,3427	1,28E-09	6,76E-04	20,7706	41,2666	1,41E+16	2,09E+16	7,07E+14	2,12E+13	2,80E+13	3,08E+09	1,48E+15
200	1423,6469	8,28E-10	4,86E-04	20,1836	49,7766	8,27E+15	1,49E+16	3,89E+14	1,89E+13	1,35E+13	2,89E+09	1,09E+15
220	1493,7864	5,69E-10	3,60E-04	19,6664	56,8205	5,16E+15	1,12E+16	2,29E+14	1,73E+13	7,05E+12	2,76E+09	8,38E+14
240	1538,9154	4,08E-10	2,72E-04	19,2046	62,8153	3,35E+15	8,61E+15	1,40E+14	1,60E+13	3,84E+12	2,68E+09	6,65E+14
260	1568,0294	3,00E-10	2,08E-04	18,7901	67,5214	2,22E+15	6,75E+15	8,77E+13	1,50E+13	2,15E+12	2,61E+09	5,36E+14
280	1586,8613	2,25E-10	1,61E-04	18,4178	71,6228	1,49E+15	5,36E+15	5,59E+13	1,41E+13	1,23E+12	2,56E+09	4,37E+14
300	1599,0743	1,71E-10	1,26E-04	18,0839	75,3036	1,02E+15	4,29E+15	3,60E+13	1,33E+13	7,11E+11	2,51E+09	3,59E+14
320	1607,0154	1,32E-10	9,93E-05	17,7852	78,1849	6,95E+14	3,45E+15	2,34E+13	1,26E+13	4,15E+11	2,47E+09	2,97E+14
340	1612,1920	1,03E-10	7,86E-05	17,5186	80,8340	4,79E+14	2,78E+15	1,53E+13	1,19E+13	2,44E+11	2,43E+09	2,46E+14
360	1615,5751	8,05E-11	6,26E-05	17,2812	83,4085	3,31E+14	2,25E+15	1,00E+13	1,13E+13	1,44E+11	2,40E+09	2,04E+14
380	1617,7916	6,35E-11	5,01E-05	17,0699	85,6516	2,30E+14	1,83E+15	6,61E+12	1,07E+13	8,56E+10	2,36E+09	1,70E+14
400	1619,2476	5,04E-11	4,02E-05	16,8818	87,5157	1,60E+14	1,48E+15	4,37E+12	1,01E+13	5,11E+10	2,33E+09	1,42E+14
420	1620,2062	4,02E-11	3,25E-05	16,7142	89,5633	1,12E+14	1,21E+15	2,90E+12	9,63E+12	3,06E+10	2,30E+09	1,18E+14
440	1620,8390	3,23E-11	2,63E-05	16,5643	90,8765	7,82E+13	9,85E+14	1,93E+12	9,15E+12	1,84E+10	2,27E+09	9,91E+13
460	1621,2577	2,60E-11	2,13E-05	16,4297	92,6589	5,49E+13	8,04E+14	1,29E+12	8,70E+12	1,11E+10	2,24E+09	8,30E+13
480	1621,5354	2,10E-11	1,73E-05	16,3079	94,5872	3,86E+13	6,57E+14	8,59E+11	8,27E+12	6,69E+09	2,22E+09	6,96E+13
200	1621,7200	1,70E-11	1,42E-05	16,1967	96,3381	2,72E+13	5,38E+14	5,76E+11	7,87E+12	4,06E+09	2,19E+09	5,84E+13
* Conce	ntrations of n	O. nH. and nw	are compute	* Concentrations of n_0 , n_H , and n_N are computed for $h > 80$ km	n u							

Concentrations of n_O, n_H, and n_N are computed for $h \ge 80 \text{ km}$



Table 15: MSISE-90 altitude profiles of temperature T, total density ρ , pressure p, mean molecular weight M and density scale height H for extremely high activities (continued)

			3		0		0			,		
h (km)	$T\left(\mathbf{K}\right)$	$ ho (kg/m^3)$	p (N/m ³)	M (kg/mol)	H (km)	$\mathbf{n}_{N_2}~(/\mathbf{m}^3)$	$\left.\mathbf{n}_{N_2}\right.(/\mathbf{m}^3)$	$\mathbf{n}_{o_2}~(/\mathbf{m}^3)$	$\left.\mathbf{n}_{He} \ \ (/\mathbf{m}^3) \right _{\mathbf{n}_{Ar}} \ \ (/\mathbf{m}^3) \ \left.\mathbf{n}_{H} \ \ (/\mathbf{m}^3)$	$\mathbf{n}_{Ar} \ (/\mathbf{m}^3)$	$\mathbf{n}_{H} \; (/\mathbf{m}^{3})$	$\mathbf{n}_N \ (/\mathbf{m}^3)$
520	1621,8430	1,38E-11	1,16E-05	16,0940	97,6136	1,92E+13	4,41E+14	3,87E+11	7,49E+12	2,47E+09	2,16E+09	4,91E+13
540	1621,9253	1,13E-11	9,50E-06	15,9980	98,0937	1,36E+13	3,62E+14	2,61E+11	7,13E+12	1,51E+09	2,13E+09	4,13E+13
260	1621,9803	9,21E-12	7,81E-06	15,9067	99,3060	9,63E+12	2,97E+14	1,76E+11	6,78E+12	9,22E+08	2,11E+09	3,47E+13
580	1622,0172	7,55E-12	6,44E-06	15,8187	100,6720	6,84E+12	2,45E+14	1,19E+11	6,46E+12	5,66E+08	2,08E+09	2,93E+13
009	1622,0421	6,20E-12	5,31E-06	15,7321	102,6271	4,87E+12	2,01E+14	8,07E+10	6,15E+12	3,48E+08	2,06E+09	2,47E+13
620	1622,0588	5,10E-12	4,40E-06	15,6457	103,0355	3,47E+12	1,66E+14	5,49E+10	5,86E+12	2,15E+08	2,03E+09	2,09E+13
640	1622,0702	4,20E-12	3,65E-06	15,5578	104,1285	2,48E+12	1,37E+14	3,74E+10	5,59E+12	1,33E+08	2,01E+09	1,76E+13
099	1622,0778	3,47E-12	3,03E-06	15,4672	104,9730	1,78E+12	1,13E+14	2,55E+10	5,33E+12	8,24E+07	1,99E+09	1,49E+13
089	1622,0830	2,88E-12	2,52E-06	15,3725	106,0742	1,28E+12	9,37E+13	1,75E+10	5,08E+12	5,13E+07	1,96E+09	1,26E+13
200	1622,0865	2,38E-12	2,11E-06	15,2723	108,0038	9,16E+11	7,76E+13	1,20E+10	4,85E+12	3,20E+07	1,94E+09	1,07E+13
720	1622,0890	1,98E-12	1,76E-06	15,1653	108,4682	6,60E+11	6,43E+13	8,22E+09	4,63E+12	2,00E+07	1,92E+09	9,09E+12
740	1622,0906	1,65E-12	1,48E-06	15,0503	108,7983	4,76E+11	5,33E+13	5,66E+09	4,41E+12	1,26E+07	1,89E+09	7,72E+12
160	1622,0918	1,37E-12	1,24E-06	14,9260	110,3542	3,44E+11	4,43E+13	3,91E+09	4,21E+12	7,90E+06	1,87E+09	6,57E+12
780	1622,0925	1,15E-12	1,05E-06	14,7912	112,2861	2,49E+11	3,68E+13	2,70E+09	4,02E+12	4,98E+06	1,85E+09	5,59E+12
800	1622,0930	9,59E-13	8,84E-07	14,6447	111,8358	1,81E+11	3,07E+13	1,87E+09	3,84E+12	3,15E+06	1,83E+09	4,76E+12
820	1622,0934	8,04E-13	7,48E-07	14,4854	113,5786	1,31E+11	2,56E+13	1,30E+09	3,67E+12	1,99E+06	1,81E+09	4,06E+12
840	1622,0936	6,74E-13	6,36E-07	14,3123	115,0666	9,56E+10	2,13E+13	9,04E+08	3,51E+12	1,27E+06	1,79E+09	3,46E+12
860	1622,0939	5,67E-13	5,42E-07	14,1244	115,8021	6,97E+10	1,78E+13	6,30E+08	3,36E+12	8,07E+05	1,77E+09	2,96E+12
880	1622,0940	4,77E-13	4,63E-07	13,9210	117,5788	5,09E+10	1,49E+13	4,40E+08	3,21E+12	5,16E+05	1,75E+09	2,53E+12
006	1622,0940	4,03E-13	3,97E-07	13,7015	118,1314	3,73E+10	1,24E+13	3,08E+08	3,07E+12	3,30E+05	1,73E+09	2,16E+12
ر ج		F		100 1								

^{*} Concentrations of n_0 , n_H , and n_N are computed for $h \ge 80 \text{ km}$



7.6 Temperature, composition, and density model of the Earth homosphere

At altitudes below about 85 km the Earth atmosphere can be assumed of uniform composition (78,1 % N_2 , 20,9 % O_2 , 0,9 % Ar, and 0,1 % CO_2 and trace constituents), at equilibrium conditions, with properties of a perfect gas. For each constituent i altitude profiles of partial pressures p_i evolve according to the law of hydrostatic equilibrium.

$$\frac{dp_i}{p_i} = -\frac{gM_i}{RT}dh\tag{7.10}$$

 p_i can be integrated from equation (7.10) for piecewise linear temperature profile segments.

The US Standard Atmosphere 1976 (USSA-76 [RD7.4]) defines the homospheric temperature as a function of altitude:

```
starting from T_0 = T (h=0) = 288,15 K,
with dT/dh = -6.5 °/km for h \in [0 \text{ km}, 11 \text{ km}],
0.0 °/km for h \in [11 \text{ km}, 20 \text{ km}],
+1.0 °/km for h \in [20 \text{ km}, 32 \text{ km}],
+2.8 °/km for h \in [32 \text{ km}, 47 \text{ km}],
0.0 °/km for h \in [47 \text{ km}, 51 \text{ km}],
-2.8 °/km for h \in [51 \text{ km}, 71 \text{ km}], and
-2.0 °/km for h \in [71 \text{ km}, 85 \text{ km}].
```

For a given temperature T(h) the partial pressures p_i translate into number densities according to

$$n_i = \frac{p_i}{kT} \tag{7.11}$$

Based on the known quantities p_i , n_i , and T, the total density ρ , total pressure p, mean free path length L, and speed of sound a can be computed as outlined in equations (7.5) to (7.9).

At altitudes below about 85 km, for objects of diameters larger than or similar to the mean free path length (d > L) the dynamic viscosity and kinematic viscosity of the ambient gas is given by the following semi-empirical relations:

$$\mu = \beta \frac{T^{3/2}}{T + S} \tag{7.12}$$

$$\eta = \frac{\mu}{\rho} \tag{7.13}$$

where

 μ is the dynamic viscosity, kg s⁻¹ m⁻¹; η is the kinematic viscosity, s⁻¹ m²; β = 1,458 × 10⁻⁶ kg s⁻¹ m⁻¹ K^{-1/2}; S = 110,4 K, Sutherland constant.

Non-static homosphere models, such as MSISE-90, allow for variations of temperature profiles and resulting densities with diurnal, longitudinal-latitudinal, seasonal-latitudinal, and solar/geomagnetic activity effects. The activity influence, however, diminishes with decreasing altitude below the turbopause. MSISE-90 and the underlying MAP 16 model [RD7.5] consider activity related effects only down to 90 km and diurnal effects only down to 72 km altitude.

Variations in total density according to MSISE-90 can have amplitudes of \pm 40 % due to seasonal-latitudinal effects (with maxima at 50 km and 110 km in June and December).



7.7 Reference model output

MSISE-90 altitude profiles of temperature, number densities (concentrations), pressure, total density, mean molecular weight, and density scale height are listed in Tables 13, 14, and 15 for low activity levels $(F_{10,7}=(F_{10,7})_{avg}=70,A_p=0)$, mean activities $(F_{10,7}=(F_{10,7})_{avg}=140,A_p=15)$, and extremely high activity levels $(F_{10,7}=(F_{10,7})_{avg}=380,A_p=300)$, respectively. The tables cover both homospheric and heterospheric altitudes from ground level up to 900 km, averaged over diurnal and seasonal latitudinal variations. Figures 5 through 7 illustrate the corresponding altitude profiles of temperature, total density, and atomic oxygen number density at minimum, maximum, and mean activity conditions. For mean activity levels Figure 8 shows the logarithmic number concentration profiles of the main atmospheric constituents. Figures 9 through 11 display diurnal and seasonal latitudinal variations of temperature, total density, and atomic oxygen concentrations at 400 km altitude. Local minima/maxima can be lower/higher than indicated here.

MSISE-90, the recommended ECSS standard atmosphere model, determines total densities at thermospheric altitudes with an r.m.s. accuracy of $\pm 10~\%$ to $\pm 15~\%$ at mean activity conditions. Especially for very high solar or geomagnetic activities these uncertainties can considerably increase due to the lack of corresponding measurement data.

For its homosphere part (below 90 km) MSISE-90 determines densities with an rms error well below 5 %. Standard deviations in temperature and pressure are on the order of 3 K and 2 %, respectively. The MSISE-90 homosphere temperature and concentration profiles are merged with those of the lower thermosphere to obtain smooth transitions in the vicinity of the turbopause (between 85 km and 120 km).

7.8 Wind model of the Earth homosphere and heterosphere

The knowledge of wind patterns in the Earth atmosphere is largely based on satellite data (mainly AE–E and DE–2), providing wind and temperature spectrometry (WATS), and Fabry-Perot interferometry (FPI). At lower altitudes ground-based incoherent scatter radar, FPI data, and meteor observations prevail in the data set.

Existing wind models, including the recommended standard HWM-93 (Horizontal Wind Model 1993, based on RD7.3) as well as GRAM-88 (Global Reference Atmosphere Model 1988 [RD7.6]) and MAH-96 (High Atmosphere Model 1996 [RD7.7]), mainly restrict themselves to a prediction of the meridional component Vx (positive towards north) and zonal component Vy (positive towards East) of the horizontal motion. The mean wind velocity in the vertical direction Vz is generally less than 1 cm/s, and can be neglected for most applications.

Much of the horizontal wind can be attributed to the flow due to the local pressure gradient, under the influence of the Coriolis acceleration. These geostrophic winds can be determined from

$$V_x = \frac{1}{2\rho\omega_e \sin\phi} \frac{\partial p}{\partial x} \tag{7.14}$$

$$V_{y} = \frac{1}{2\rho\omega_{e}\sin\phi} \frac{\partial p}{\partial y} \tag{7.15}$$

where

p is the local pressure, N/m^2 ;

 $V_{\rm r}$ is the northward meridional wind component, m/s;

 V_{ν} is the eastward zonal wind component, m/s;

 ρ is the local air density, kg/m³;



 ω_e = 7,292 × 10⁻⁵ rad/s, Earth rotation rate;

 ϕ is the geodetic latitude, ° (degrees).

In equatorial regions (i.e. for $\phi \in [-15^{\circ}, +15^{\circ}]$) these assumptions are not valid, and results for such latitudes should be determined from linear interpolation between $\phi = \pm 15^{\circ}$. The concept of geostrophic winds is applied by GRAM-88 in the altitude range 0 km to 20 km and above 90 km. MAH-96 uses geostrophic winds from underlying MSISE-90 pressure gradients over its entire altitude range from 0 km to 120 km.

Considering its close relationship with the MSISE-90 atmosphere model and its compatibility with the stochastic MAH-96 wind model, HWM-93 is adopted as deterministic horizontal wind model for homospheric and heterospheric altitudes. Below 120 km, for the analysis of small scale perturbation spectra, the MSISE-90 based MAH-96 model [RD7.7] is recommended.

An empirical horizontal wind model in terms of vector spherical harmonic expansions is used by HWM-93 for altitudes from 0 km to 2000 km. The HWM 93 model has a similar structure and the same parameters as the atmosphere model MSISE-90, with equally unconstrained applicability from ground level to exospheric altitudes. Geostrophic wind contributions are embedded in the harmonic expansions of HWM-93. The horizontal wind directions and magnitudes are found to change with a diurnal period at thermospheric altitudes and with a semidiurnal period in the homosphere. The effect of solar activity indices (though included in the model) is small. Apart from (semi-)diurnal variations, mainly seasonal-latitudinal effects dominate, with amplitudes which are largely driven by geomagnetic activity. Since A_p effects focus on the vicinity of the magnetic poles, and since the related dynamics is not totally predictable, wind models tend to be most reliable at moderate and low latitudes. The wind directions and velocities provided by HWM-93 closely correlate with pressure distributions according to MSISE-90. Hence, highest velocities are noted along the dawn-dusk region, especially towards the night hemisphere across the poles. Here, wind speeds of up to 1 km/s can be reached at moderate thermospheric altitudes (e.g. around 300 km). Diurnal and seasonal-latitudinal variation patterns of HWM-93 winds in 400 km altitude at mean activity conditions are shown in Figures 12(a) and 12(b).

7.9 Simple density models of planetary atmospheres

For the major planets and for the Saturn moon Titan (the largest moon in the solar system) simple atmosphere models are available, which mostly restrict themselves to uniform, mean density profiles based on the hydrostatic equilibrium of an isothermal atmosphere.

The planetary atmosphere densities as a function of altitude can be approximated as:

$$\rho(h) = \rho_0 \exp \left[\frac{-(h - h_0)}{H_0} \right]$$
 (7.16)

with model parameters selected according to the following list:

Venus (C. Sagan et al., 1971, [RD7.8])

 h_0 = 285 km, reference altitude

 ρ_0 = 7,1 × 10⁻⁹ kg/m³, reference density H_0 = 44,8 km, reference density scale height

Mars (A. Seiff and D.B. Kirk, 1977, [RD7.9])

 h_0 = 140,0 km, reference altitude ρ_0 = 7,25 × 10⁻¹⁰ kg/m³, reference density H_0 = 11,127 km, reference density scale height



Jupiter (R.J. Newburn and S. Gulkis, 1973, [RD7.10])

 h_0 = 314,4 km, reference altitude

 ho_0 = 3,86 × 10⁻⁸ kg/m³, reference density H_0 = 21,0 km, reference density scale height

Saturn (R.J. Newburn and S. Gulkis, 1973, [RD7.10])

 h_0 = 536,1 km, reference altitude

 $ho_0 = 2.32 \times 10^{-8} \text{ kg/m}^3$, reference density $H_0 = 40.0 \text{ km}$, reference density scale height

Titan (R.J. Newburn and S. Gulkis, 1973, [RD7.10])

 h_0 = 0,0 km, reference altitude ρ_0 = 5,53 kg/m³, reference density

 H_0 = 24,3 km, reference density scale height

More detailed constituent-wise models and day/night hemisphere models are available for some planets.

For rough calculations equation (7.16) can also be applied to model the Earth atmosphere. The density scale height H_0 shall then be obtained from Tables 13, 14, or 15 (depending on the activity level), for an altitude of interest h_0 .

7.10 Aerodynamics in the Earth atmosphere

The aerodynamic perturbation acting on a spacecraft during its orbital motion or atmospheric descent can be described by the drag component (D) and lift component (L) of the aerodynamic force.

$$a_D = \frac{1}{2}\rho \frac{A}{m}V^2 c_D \tag{7.17}$$

$$\alpha_L = \frac{1}{2}\rho \frac{A}{m} V^2 c_L \tag{7.18}$$

where

 a_D is the aerodynamic drag, parallel to free-stream velocity, m/s²;

 a_L is the aerodynamic lift, perpendicular to free-stream velocity, m/s²;

 c_D is the drag coefficient, dimensionless;

 c_L is the lift coefficient, dimensionless;

V is the free-stream aerodynamic velocity, m/s;

 ρ is the local air density, kg/m³;

A is the aerodynamic reference cross-section, m²;

m is the spacecraft mass, kg.

Due to the energy dissipating character of the drag deceleration, natural orbital motion below altitudes of 120 km cannot be sustained in the Earth atmosphere.

The values of the drag and lift coefficient are depending on the spacecraft shape and dimensions, and on the flow conditions which can be characterized by the dimensionless Mach number M_a , Reynolds number R_e , and Knudsen number K_n .

$$M_a = \frac{V}{a} \tag{7.19}$$

$$R_e = \frac{\rho V d}{\mu} \tag{7.20}$$

$$K_n = \frac{L}{d} \tag{7.21}$$

where

a is the speed of sound, m/s;

d is the characteristic spacecraft dimension, m;



 μ is the dynamic viscosity, kg s⁻¹m⁻¹;

L is the mean free path length of molecules, m.

The relevant aerodynamic theories to be used to derive c_D and c_L depend on the flow regimes which are identified via the Mach and Reynolds number. Three main regimes can be distinguished:

 $M_a/R_e > 3$: free molecular flow

 $M_a/R_e < 3$ and $M_a/R_e > 0.01$: transitional flow

 $M_a/R_e < 0.01$: continuum flow.

Within the free molecular regime the incident flow is undisturbed by the body moving through it. This is also referred to as a collisionless flow. The momentum exchange is dominated by the gas-surface interaction mechanisms. Closed form analytical solutions exist in this regime, particularly for simple, convex body shapes. For simplified engineering analyses it is often adequate to use $c_D = 2,2$ and $c_L = 0,0$ (assuming the cross-section A to be the projected body surface perpendicular to the flow).

The transitional flow regime is not well understood, and no closed form solutions exist which cover the conditions from free-molecular flow to intermolecular collision flow. Numerical DSMC (Direct Simulation Monte Carlo) Methods can closely simulate the transitional flow conditions, but they are computationally intensive. For most engineering applications bridging methods are used to join the easily obtainable results of the free-molecular regime (above altitudes of transitional flow), and the continuum regime (below altitudes of transitional flow).

$$\frac{(c_D - c_{D,c})}{(c_{D,f} - c_{D,c})} = f_D(K_n) \tag{7.22}$$

$$\frac{(c_L - c_{L,c})}{(c_{L,f} - c_{L,c})} = f_L(K_n) \tag{7.23}$$

where

 $()_c$ are the continuum flow results;

 $()_f$ are the free-molecular flow results;

 $f_{D,L}$ are the bridging function for drag and lift coefficient, dimensionless.

The continuum regime dominates the aerodynamic characteristics of re-entry vehicles. It can be categorized as follows:

 $M_a \leq 0.3$: incompressible flow

 $0.3 < M_a < 1.0$: compressible flow

 $0.8 < M_a < 1.2$: transonic flow

 $M_a > 1.0$: supersonic flow

 $M_a > 5.0$: hypersonic flow.

In the most general case, complete solutions of the Navier-Stokes equations shall be used to characterize the aerodynamic behaviour of a vehicle in the continuum regime. For simplified engineering applications, however, a constrained Newtonian solution can be applied (assuming only pressure, but no shear stress forces acting on the vehicle). In this case, for simple, convex bodies, analytical expressions can be derived which depend on the body shape and on the angle of attack. For a sphere the continuum drag coefficient results in $c_D = 1,0$.



7.11 Figures

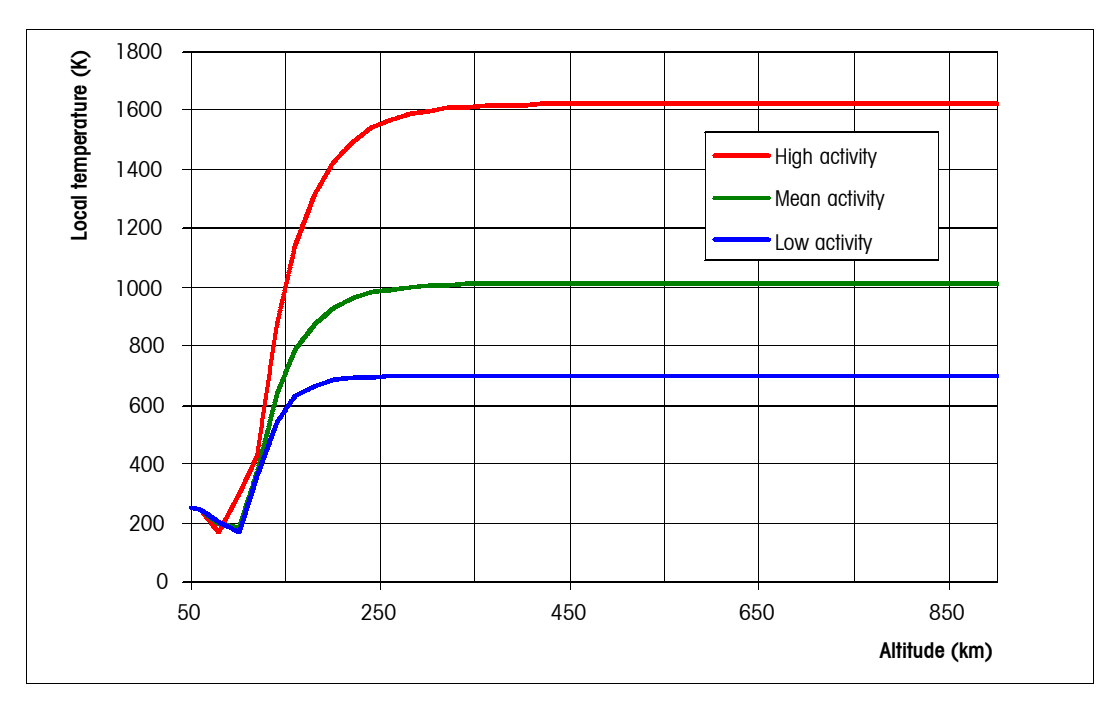


Figure 5: Variation of the MSISE-90 mean temperature with altitude for extremely low activities, for mean activities and for extremely high activities

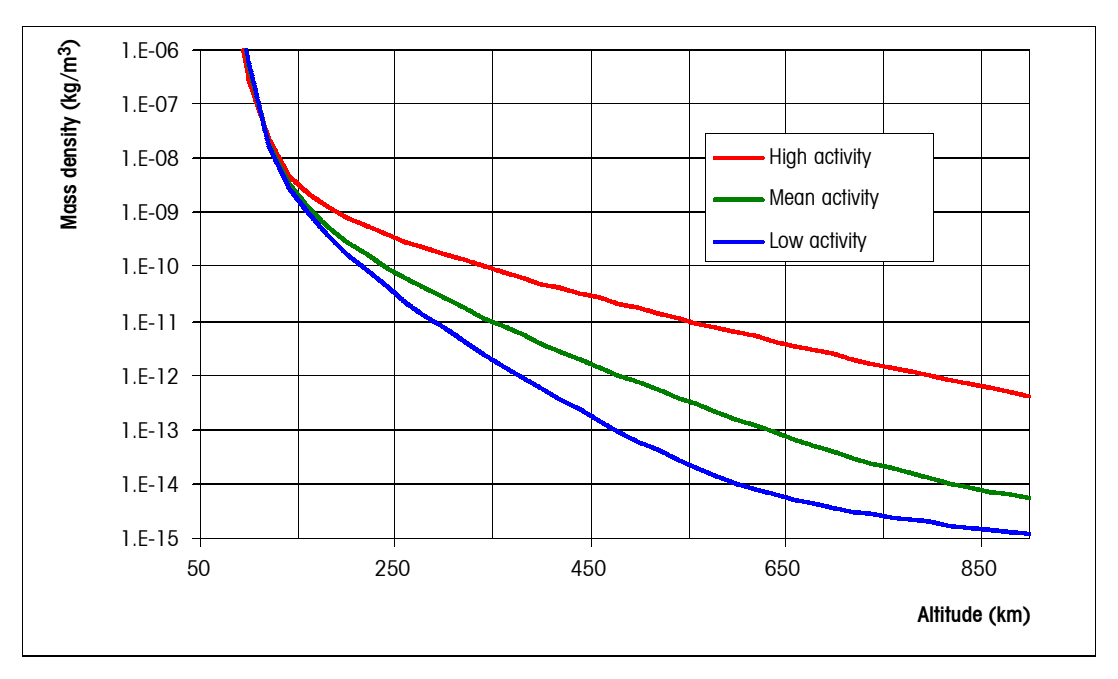


Figure 6: Variation of the MSISE-90 mean air density with altitude for low activities, for mean activities and for extremely high activities



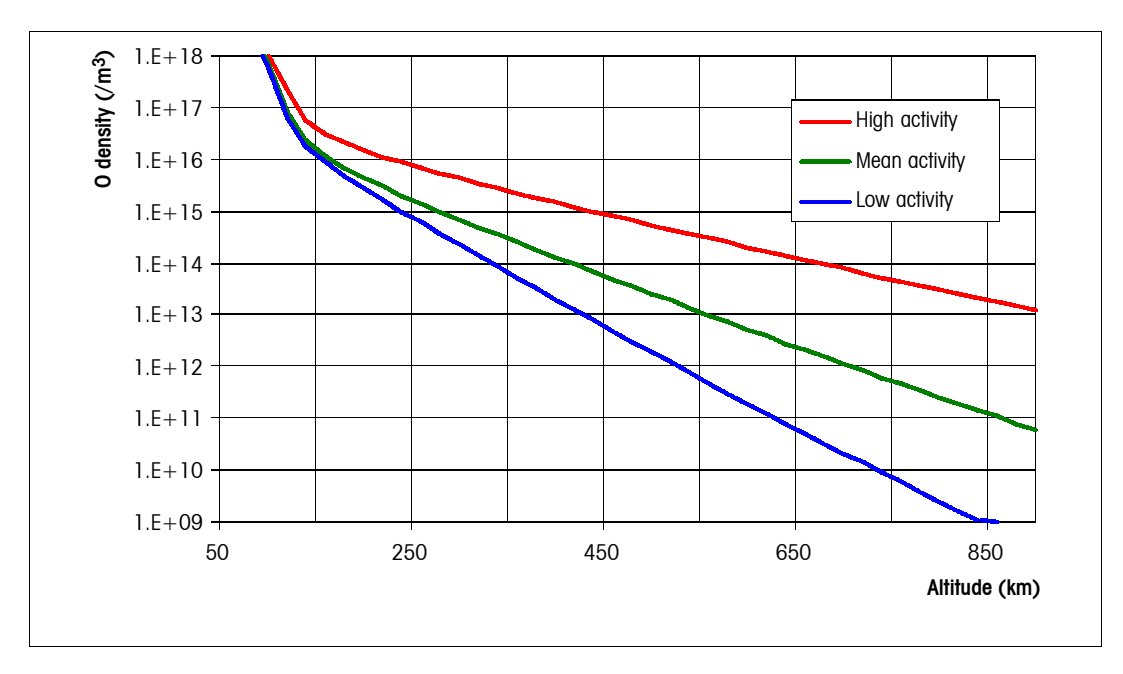


Figure 7: Variation of the MSISE-90 mean atomic oxygen with altitude for extremely low activities, for mean activities and for extremely high activities

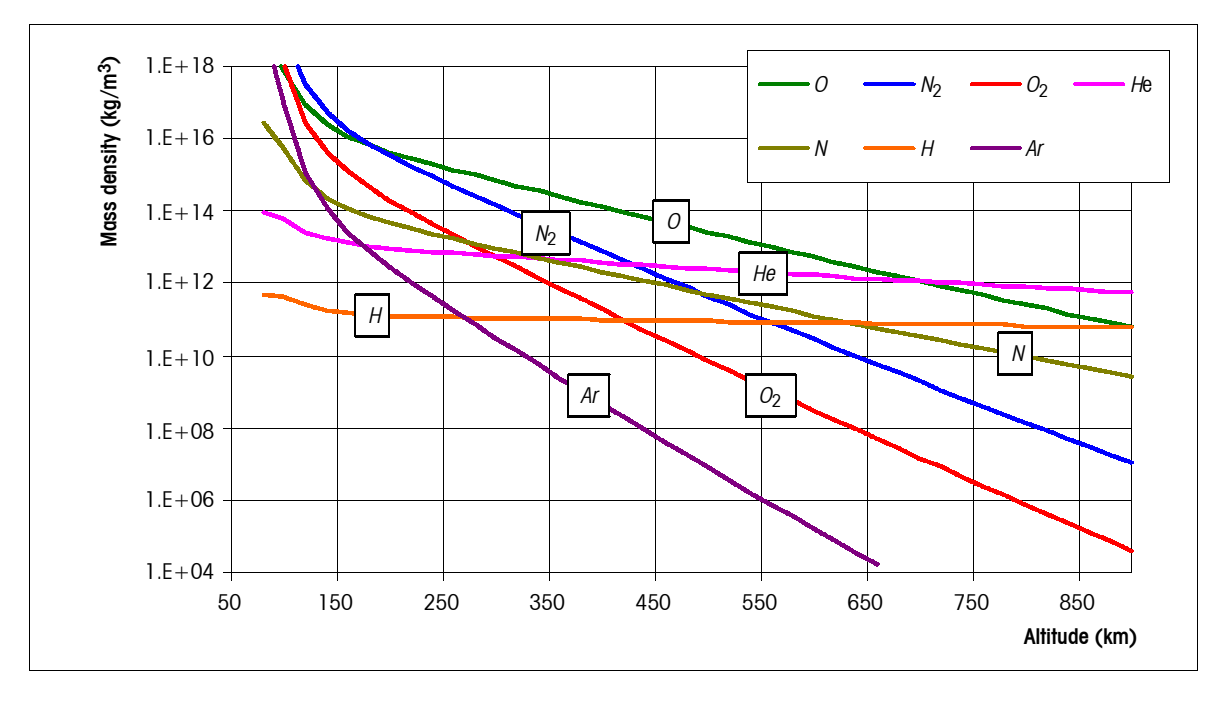
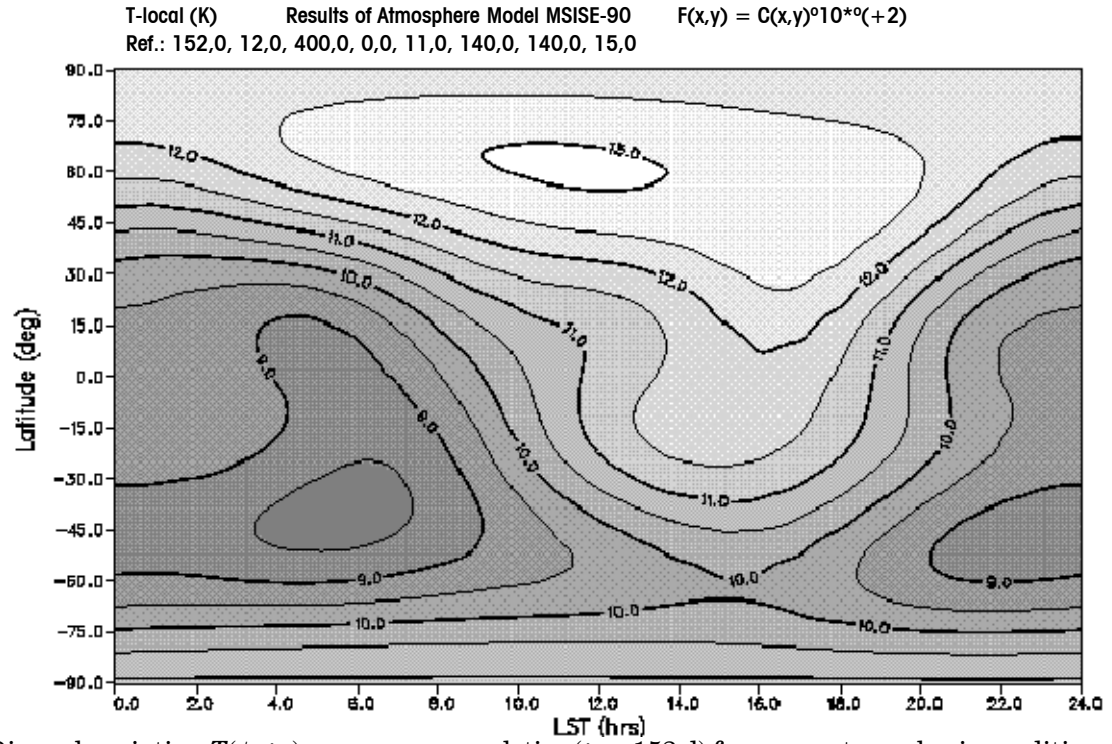


Figure 8: Variation of the MSISE-90 mean concentration profile of the atmosphere constituents N_2 , O, O_2 , He, Ar, H, and N with altitude for mean activities

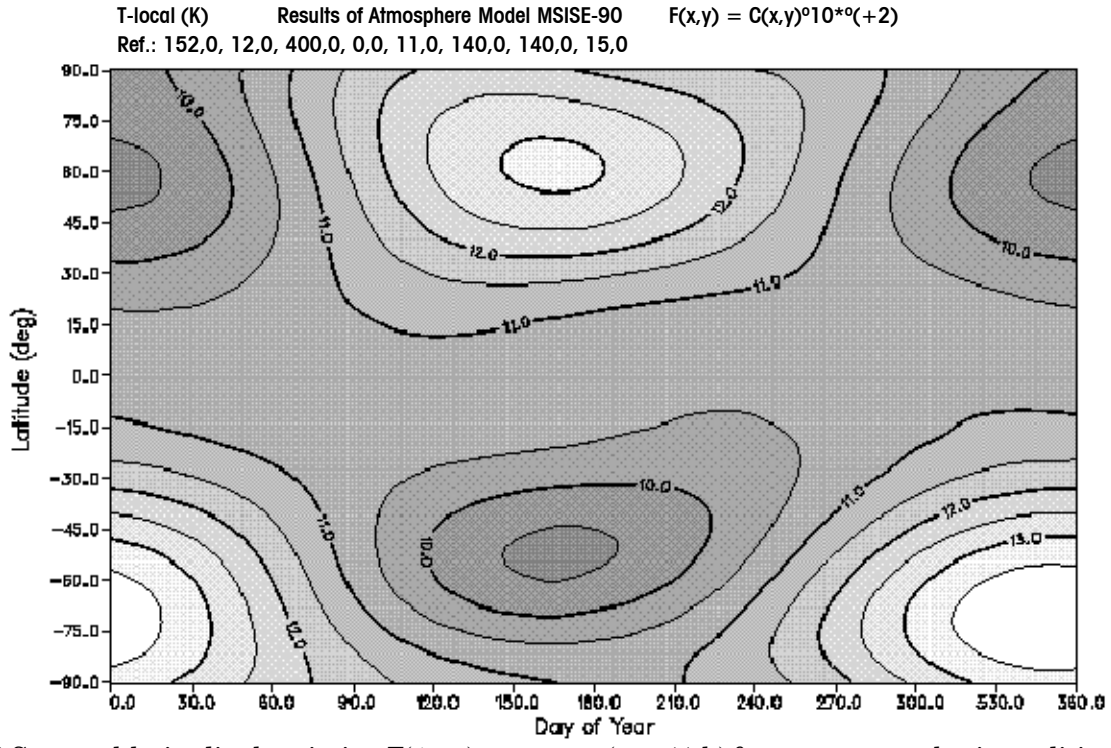


T-local (K)



Results of Atmosphere Model MSISE-90

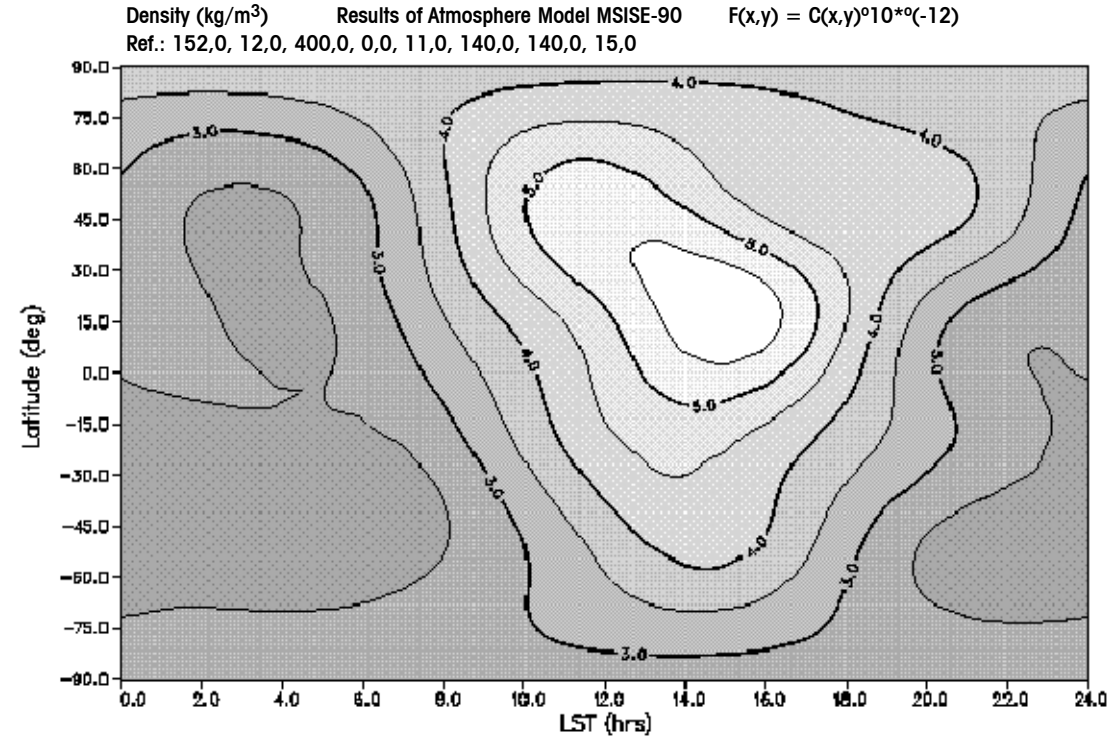
(a) Diurnal variation $T(\phi, t_{ls})$ near summer solstice ($t_d = 152$ d) for mean atmospheric conditions. The level lines indicate temperatures *T* in units of 100 K.



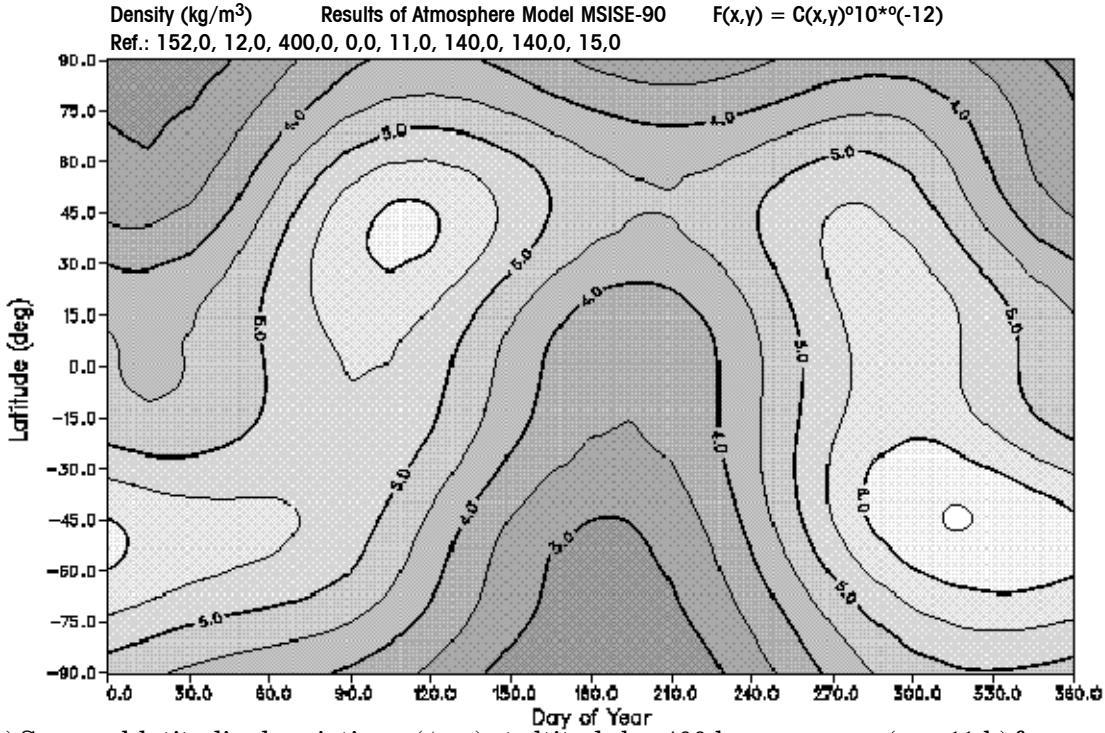
(b) Seasonal-latitudinal variation $T(\phi, t_{ls})$ near noon ($t_{ls} = 11 \text{ h}$) for mean atmospheric conditions. The level lines indicate temperatures T in units of 100 K.

Figure 9: Diurnal (a) and seasonal-latitudinal (b) variations of the MSISE-90 local temperature at altitude h = 400 km





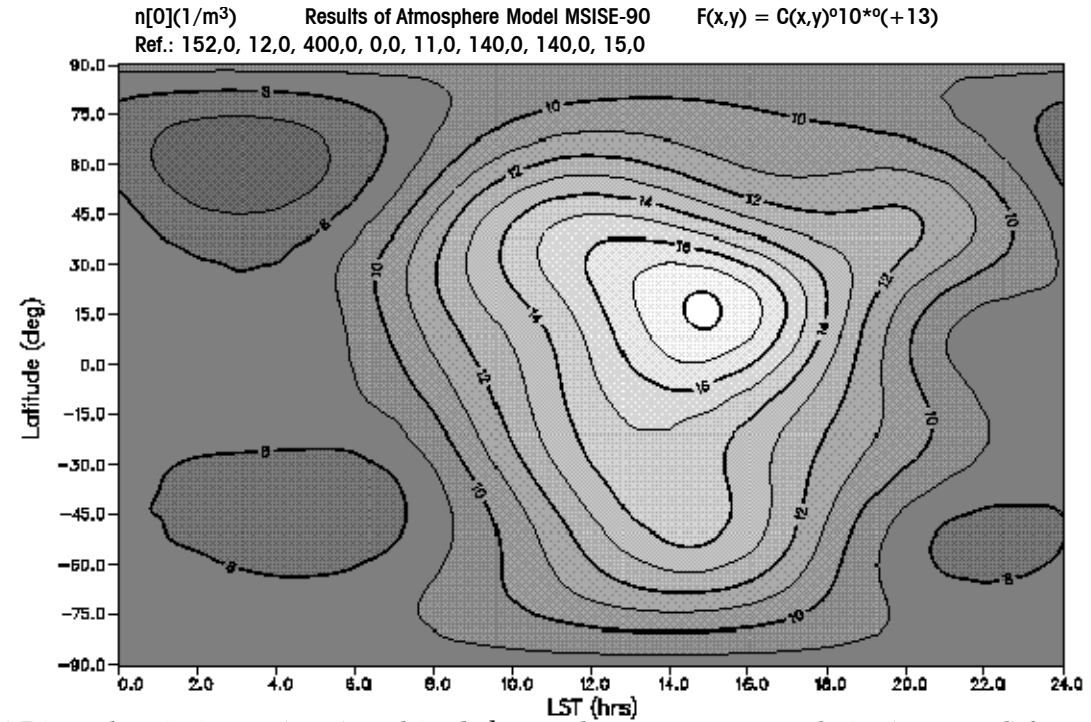
(a) Diurnal variation ρ (ϕ , t_{ls}) at altitude h = 400 km near summer solstice (t_d = 152 d) for mean atmospheric conditions. The level lines indicate air densities in units of 10^{-12} kg/m³.



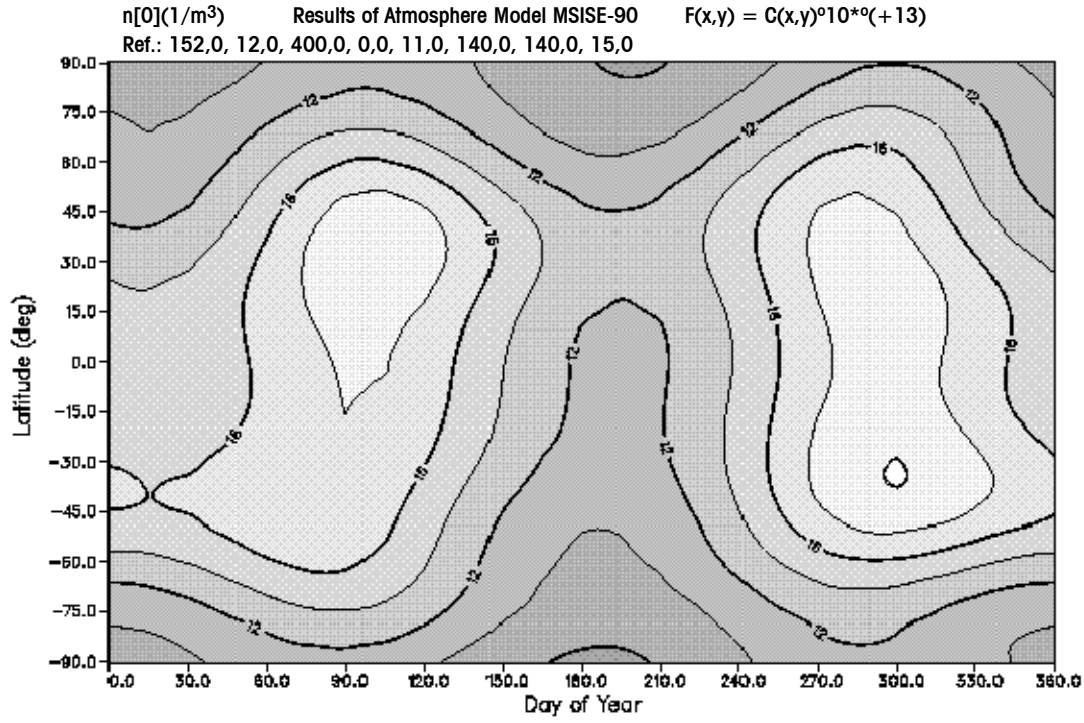
Day of Year (b) Seasonal-latitudinal variation ρ (ϕ , t_d) at altitude h = 400 km near noon (t_{ls} = 11 h) for mean atmospheric conditions. The level lines indicate air densities in units of 10^{-12} kg/m³.

Figure 10: Diurnal (a) and seasonal-latitudinal (b) variations of the MSISE-90 air density at altitude $h=400~\rm km$ for mean atmospheric conditions





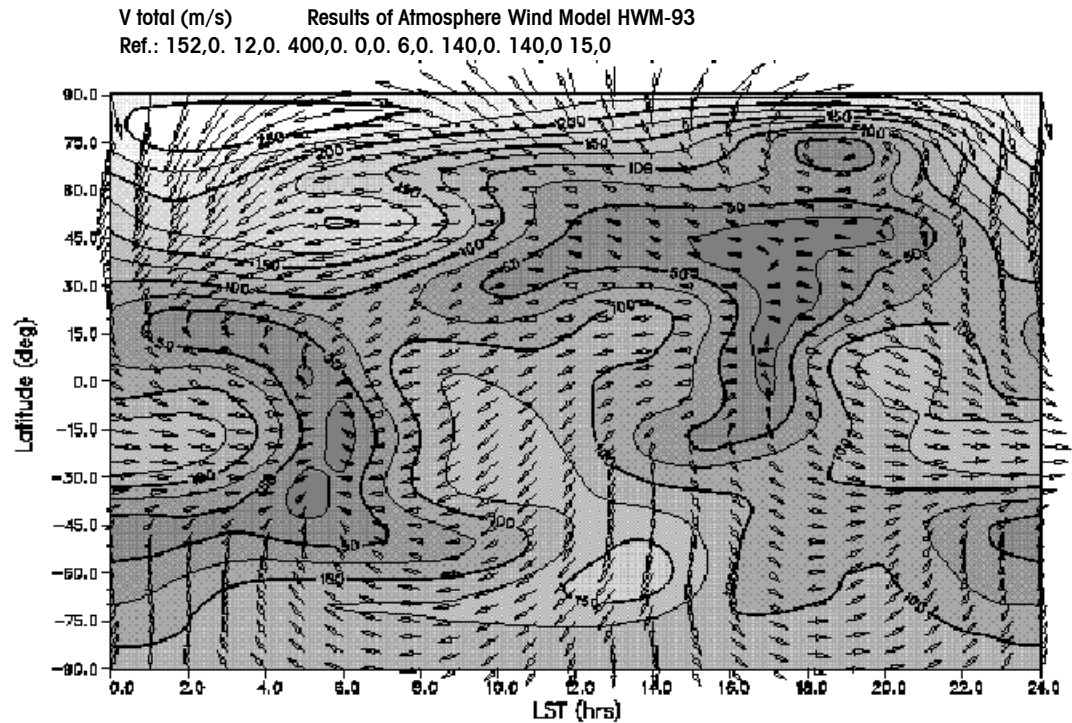
(a) Diurnal variation $n_O(\phi, t_{ls})$ at altitude h = 400 km near summer solstice (t_d = 152 d) for mean atmospheric conditions. The level lines indicate atomic oxygen concentrations n_O in units of $10^{+13} \ 1/\text{m}^3$.



(b) Seasonal latitudinal variation $n_O(\phi, t_d)$ at altitude h = 400 km near noon ($t_{ls} = 11$ h) for mean atmospheric conditions. The level lines indicate atomic oxygen concentrations n_O in units of 10^{+13} 1/m³.

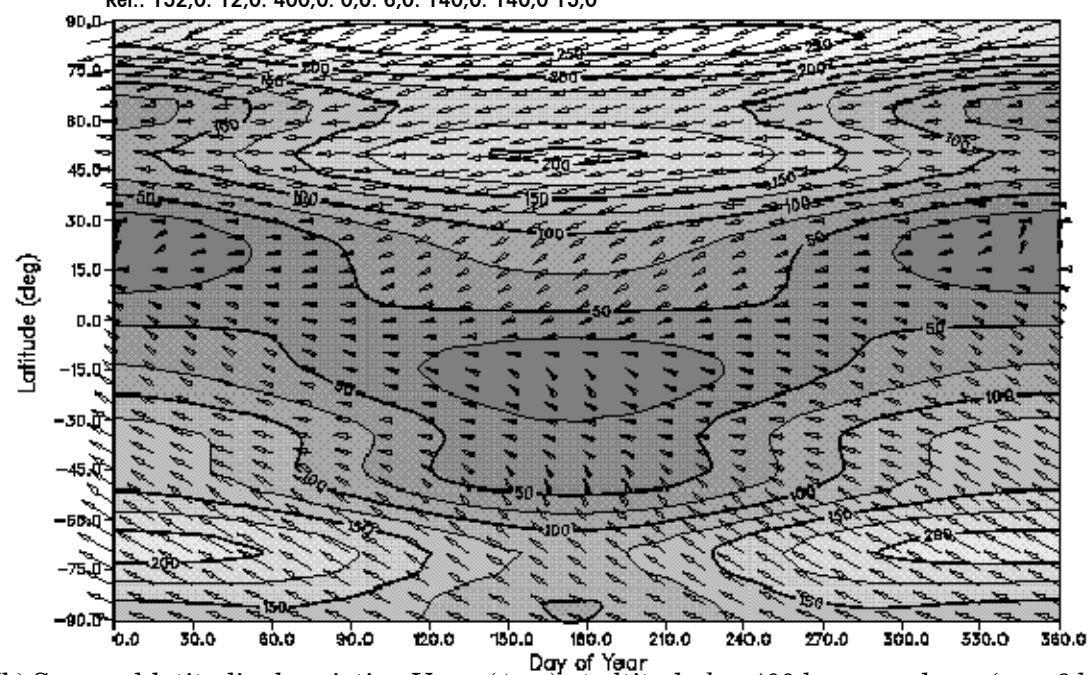
Figure 11: Diurnal (a) and seasonal latitudinal (b) variations of the MSISE-90 atomic oxygen concentration at altitude $h=400~\rm km$ for mean atmospheric conditions





(a) Diurnal variation \underline{V}_{wind} (ϕ , t_{ls}) at altitude h=400 km near summer solstice ($t_d=152$ d) for mean atmospheric conditions ($F_{10,7}=(F_{10,7})_{avg}=140$, $A_p=15$, $t_{ut}=12$ h). The level lines indicate horizontal wind magnitudes in m/s. They connect the footpoints of wind vectors of the same length. Wind directions are indicated by the orientation of the wind vectors (left = West, right = East, up = North, down = South).

V total (m/s) Results of Atmosphere Wind Model HWM-93 Ref.: 152,0. 12,0. 400,0. 0,0. 6,0. 140,0. 140,0 15,0



(b) Seasonal-latitudinal variation \underline{V}_{wind} (ϕ , t_d) at altitude h=400 km near dawn ($t_{ls}=6$ h) for mean atmospheric conditions ($F_{10,7}=(F_{10,7})_{avg}=140$, $A_p=15$, $t_{ut}=12$ h). The level lines indicate horizontal wind magnitudes in m/s. They connect the footpoints of wind vectors of the same length. Wind directions are indicated by the orientation of the wind vectors (left = West, right = East, up = North, down = South).

Figure 12: Diurnal (a) and seasonal-latitudinal (b) variations of wind magnitude and direction according to HWM-93 at altitude $h=400~\mathrm{km}$ for mean atmospheric conditions



7.12 References

- RD7.1 Hedin A.E., "Extension of the MSIS Thermosphere Model into the Middle and Lower Atmosphere" J. Geophys. Res., Vol. 96, No. A2, pp. 1159–1172, Feb.1, 1991.
- RD7.2 Hedin A.E., "MSIS-86 Thermospheric Model" J. Geophys. Res., Vol. 92, No. A5, pp 4649 4662, May 1, 1987.
- RD7.3 Hedin A.E. et al., "Revised Global Model of Thermosphere Winds Using Satellite and Ground-based Observations", J. Geophys. Res., Vol.96, No. A5, pp 7657–7688, May 1, 1991.
- RD7.4 Anon., "U.S. Standard Atmosphere, 1976", U.S. Government Printing Office, Washington/DC, 1976.
- RD7.5 Barnett J. and M. Corney, "Middle Atmosphere Reference Model Derived from Satellite Data Handbook MAP 16", Eds. K. Labitzke, J. Barnett, and B. Edwards, pp. 47 85, Sci. Comm. for Sol.-Terr. Phys. Secr., Univ. of Illinois/Urbana, 1985.
- RD7.6 Justus C.G., F.N. Alyea, D.M. Cunnold, R.S. Blocker and D.L. Johnson, "GRAM 88, Improvements to the Perturbation Simulation of the Global Reference Atmospheric Model", NASA MSFC memorandum ES-44-11-9-88.
- RD7.7 Didier C. and A. Maillard, "High Atmosphere Model" Final Report of ESA contract no. RFP/3 8126/F/FB, June 1996.
- RD7.8 Sagan C., Ed. Planetary Atmospheres, D. Reidel, Dordrecht, The Netherlands, 1971.
- RD7.9 Seiff A., B.D. Kirk, "Structure of the Atmosphere of Mars in Summer at Mid-Latitudes", J. Geophys. Res., Vol. 82, No. 28, pp. 4634, Sep. 30, 1997.
- RD7.10 Newburn R.L. and S. Gulkis, "A Survey of the Outer Planets Jupiter, Uranus, Neptune, Pluto, and their Satellites", Space Sci. Rev., Vol. 3, pp. 179, 1973.



 $(This\ page\ is\ intentionally\ left\ blank)$

8

Plasmas

8.1 Introduction

A plasma is a partly or wholly ionized gas whose particles exhibit a collective response to magnetic and electric fields. The collective motion is brought about by the electrostatic Coulomb force between charged particles. This causes the particles to rearrange themselves to counteract electric fields within a distance of the order of λ , the Debye length.

$$\lambda = \left(\frac{\varepsilon_0 k T_e}{ne^2}\right)^{1/2}$$

where

 λ is the Debye length expressed in m;

 T_e is electron temperature in expressed in K;

e is electron charge expressed in C;

n is density in expressed in, m⁻³;

k is the Boltzmann constant;

 ε_0 is the permittivity of free space.

On spatial scales larger than λ plasmas are electrically neutral.

Spacecraft in Earth orbit can experience a number of distinct plasma regimes:

- The ionosphere, the cold plasma regime at the top of the atmosphere.
- The magnetosphere, the area above the ionosphere dominated by the Earth magnetic field and bounded by the magnetopause. This can be usefully divided into the cold low altitude regime, or plasmasphere and the hot high altitude regime.
- The solar wind, surrounding the magnetosphere, originating on the Sun and blowing throughout interplanetary space.

Within the magnetosphere, plasma flows freely up and down magnetic field lines but only slowly across it. Hence, two spacecraft observe similar plasmas if they are on the same field line, even if far apart. These spacecraft share the same L-shell and magnetic local time.

The principal spacecraft engineering concerns caused by space plasmas are outlined in Table 16 (see annex F for further details).



Table 16: Main engineering concerns due to space plasmas

Scenario	Problem
High altitudes	Surface charging - possibly harmful electrostatic discharges.
High-voltage systems	Power leakage, possible discharges, high
at low altitudes	spacecraft ground potential, sputtering.
Large spacecraft at	Spacecraft wake creation.
low altitudes	
Polar orbiting	Surface charging - sputtering and possible
spacecraft	discharges.
All spacecraft	Ionospheric barrier to ground-space
	communications below a threshold frequency.
	Perturbation of signals at higher frequencies.
Radar/navigation	Ionospheric propagation delays to beams.
Electric propulsion	Interactions between generated plasma, ambient
	plasma, and the spacecraft.
Scientific spacecraft	Low level charging and photoelectrons which
	interfere with plasma measurements.
	Plasma entry into sensitive detectors.

8.2 The ionosphere

8.2.1 Description

The ionosphere is the ionized plasma at the top of the atmosphere, produced by the dissociation of atmospheric atoms, mainly by sunlight. A good general description of this environment can be found in NASA TM-4527 [RD8.1], page 4-3. Here a less detailed summary of ionospheric characteristics is given.

It is generally divided into layers D, E and F1 at low altitudes and F2 at higher altitude. The low altitude layers are significant only during daylight hours. F2 is permanent and the most dense, peaking at around 300 km altitude. Ion composition varies between the different layers but, for most space applications, it is the electron density which is the most important characteristic. Immediately above the F2 peak, density falls off nearly exponentially with height. At mid to low latitudes, the density fall- off slows down at higher altitudes as the magnetic field traps plasma to form the plasmasphere.

In the auroral region, between 60° and 70° latitude, ionospheric density can become irregular on the scale of metres to kilometres vertically and metres to hundreds of kilometres horizontally. This is caused through heating by energetic electrons and plasma drift due to electric fields in the magnetosphere. The energetic electrons have energies of 10s of keV and travel to the ionosphere from the outer magnetosphere along magnetic field lines. Plasma density in this region can suddenly increase by a factor of up to 100 during magnetically active periods.

In the Polar Cap, above 70°, density fluctuations are less severe but because of the tilt of the Earth, there is a strong winter-summer asymmetry. Strong drift motion occurs due to electric fields. In winter, density is maintained by this drift and by "polar rain", a weak electron flux from the solar wind with energy around 100 eV. When both these processes are depressed, ionospheric density in this region can become very low.

8.2.2 Effects

High plasma densities in the ionosphere cause reflection of radio beams below a critical frequency, as well as refraction and other effects. Hence the ionosphere acts as a barrier to satellite-ground communications and complicates satellite radar altimetry, satellite navigation systems and the radio tracking of satellites.



The high velocity of an orbiting spacecraft relative to ion velocity in this region leads to a plasma void in its immediate wake. In the auroral zone, where there are energetic electrons, this can permit surface charging to occur on wake surfaces.

For high potential surfaces, the abundance of cold ions and electrons allows current to flow through the plasma, because ions and electrons are drawn to negative and positive regions respectively. This acts as a current drain on high voltage systems, such as solar arrays and necessitates the covering of otherwise exposed surfaces. The greater mobility of electrons over ions means that a solar array tends to float with the positive end near space potential. If the negative end is selected to be spacecraft ground, this can result in the spacecraft body being significantly negative relative to space.

8.2.3 Models

The International Reference Ionosphere 1995 (IRI95) [RD8.2] shall be used for scoping studies of ionospheric parameters, although it should be stressed that it is not suitable for real-time calculations. This model calculates ionospheric plasma parameters below 60° latitude. It provides monthly mean plasma density, composition and temperature for magnetically quiet conditions in the altitude range 60km to 3000km. It is described in detail in RD8.2 and is obtainable from NSSDC via the Internet. See annex F for details.

IRI95 contains a number of options suitable for different applications. Recommended choices are indicated when the code is run. Error bars in the model at quiet times are a factor of 2 to 4 below the F2 peak. Above the F2 peak errors can be up to a factor 10 [RD8.1].

In the auroral zone, the USAF MIL-STD-1809 model [RD8.3] shall be used to represent precipitating electrons. However, a typographical error means it is printed incorrectly in RD8.3. For diffuse aurorae:

- Intensity distribution: Gaussian with full width at half maximum of 3°.
- Energy distribution:

Gaussian i.e.
$$Flux(E) = \left[\frac{Q}{2(E_m)^3}\right] E \exp\left(-\frac{E}{E_m}\right)$$

where

Flux(E) is expressed in cm⁻² s⁻¹ keV⁻¹;

E is the energy in keV;

 E_m is the characteristic energy in keV;

Q is the integral energy flux in ergs cm⁻² s⁻¹.

Table 17: Parameters for the USAF diffuse aurora model

	Minimum	Typical	Nominal	Maximum
Q	0,25	1,0	3,0	12,0
E_m	0,40	1,15	3,0	9,0

For discrete aurorae the USAF MIL-STD-1809 [RD8.3] model shall be used:

- Intensity distribution: Gaussian with full width at half maximum of 0,1°.
- Energy distribution: Gaussian.
- *Flux(E)* ten times higher than for the diffuse aurora, shown above.



8.2.4 Typical and worst case parameters

Table 18 shows an altitude profile of electron density, as calculated by IRI95, at 0° longitude and latitude, on 1st January, for a near-average sunspot number of 100, at 0 h and 12 h local time, using otherwise default options.

Table 18: Ionospheric electron density profiles derived from IRI95 [RD8.2]

Height (km)	Midnight electron density (cm ⁻³)	Noon electron density (cm ⁻³)
100	2900	157974
200	64987	204147
300	777138	469115
400	860340	1438307
500	465137	1212265
600	246060	554271
700	162271	296707
800	129393	212067
900	115569	181719
1000	109497	170067

For auroral charging assessment, the following worst-case electron distribution function shall be used. (This standard comes from RD8.3 and is based on work described in RD8.4. Unfortunately, it is printed in RD8.3 with a typographical error.)

For $E \le 17,44 \text{ keV}$:

$$f(E) = 3.9 \times 10^{-30}$$

For E > 17,44:

$$f(E) = \frac{\left[N_0(m_e)^{3/2} \exp[-(E-E_0)/kT_0]\right]}{(2\pi kT_0)^{3/2}}$$

where

f(E) is the distribution function in $\sec^3 \text{ cm}^{-6}$;

 N_0 is the density = 1,13 cm⁻³;

 kT_0 is the "temperature" = 3.96 keV;

 $E_0 = 17,44 \text{ keV};$

 $m_{\rm e}$ is the electron mass.

For auroral charging assessment, thermal ion density of 125 cm⁻³ shall be used to represent a severely low density ion population. This comes from a severe charging case seen on the DMSP spacecraft by RD8.5. Measuring ionospheric thermal ion density during a strong charging event is potentially prone to errors because of the way the charged satellite alters ion trajectories, so there is a degree of uncertainty in this measurement.

The above worst-case environment shall be used to predict spacecraft surface potential using the POLAR [RD8.6] charging code or an equivalent code or calculations, applicable to the low Earth orbit environment. POLAR accepts inputs as Maxwellian, Power Law or Gaussian distributions.



8.3 The plasmasphere

8.3.1 Description

The plasmasphere is a region of cold dense plasma originating in the ionosphere and trapped by the Earth magnetic field.

Two magnetospheric electric fields, the co-rotation and cross-tail fields, cause particles, spiralling up and down field lines, to undergo drift perpendicular to the magnetic field. At low L-shells, the co-rotation field dominates and drift trajectories form closed paths. This allows ions, escaping from the ionosphere, to accumulate to form the dense plasmasphere. At higher L-shells, the cross-tail field dominates and drift trajectories carry particles sunwards to the magnetopause, where they are lost from the magnetosphere. The boundary between closed and open drift paths is highly variable and the outer regions of the plasmasphere are continually being lost and refilled over a period of days. Typically, the plasmapause, the outer edge of the plasmasphere, lies at an L-shell of 3 to 6, with a bulge in the dusk region of magnetic local time.

8.3.2 Effects

Because the plasmasphere contains a dense plasma, it contributes to the radio propagation effects that affect ground-space communications with satellites at high altitude. However, densities here are far below ionospheric density, so the effect is not large.

Plasmaspheric ions play a moderating role in spacecraft charging because any strong negative potential attracts ions and is neutralized. Effectively, hazardous surface charging can be said not to occur in the plasmasphere.

8.3.3 Models

Because the plasmasphere is quite variable and yet does not present major engineering concerns, it has not been considered necessary to define a standard model for this region. Nevertheless, where a model is required for scoping studies of typical plasmasphere parameters, the empirical model of Carpenter and Anderson [RD8.7] is recommended. This model is particularly comprehensive and includes terms to describe solar cycle variation and annual and semi-annual variations. Density is described as:

$$\log(n_e) = (-0,34145L + 3,9043)$$

$$\begin{split} & + \left[\ 0,15 \bigg(\cos \bigg(\frac{2\pi (d\,+\,9)}{365} \bigg) - \ 0,5 \cos \bigg(\frac{4\pi (d\,+\,9)}{365} \bigg) \bigg) + \ 0,00127 \overline{R} - \ 0,0635 \ \right] \\ & \times \exp \bigg(- \frac{(L\,-\,2)}{1,5} \bigg) \end{split}$$

where

 n_e is the electron density in cm⁻³;

d is the day of year;

 \overline{R} is the 13-month average sunspot number, centred on day d.

For purposes such as estimating the likelihood of charging, the plasmaspheric density is not as important as the position of the plasmapause. In the Carpenter and Anderson model, the inner edge of the plasmapause is given as follows:

$$L_{\rm ppi}$$
 = 5,6 - 0,46 $K_{\rm pmax}$

where

 $L_{\rm ppi}$ is the inner plasmapause boundary in units of Earth-radii;



 $K_{p \max}$

is the maximum K_p in the preceding 24 h, except that for MLT intervals 06-09, 09-12 and 12-15, one, two and three immediately preceding K_p values are omitted.

8.3.4 Typical parameters

Typical ion and electron temperatures, throughout the plasmasphere are of the order of 1 eV and 0,5 eV, respectively. The electron temperature is thus far too low to produce hazardous charging effects.

Table 19: Electron density vs. *L*-shell for the Carpenter and Anderson [RD8.7] model, ignoring seasonal and solar cycle effects

L-Shell (Earth-radii)	Electron density (cm ⁻³)
2,5	1312
3,0	913
3,5	636
4,0	442
4,5	308
5,0	214

8.4 The outer magnetosphere

8.4.1 Description

Beyond the plasmapause and within the magnetopause, the magnetospheric plasma environment is characterized by high temperatures and low densities. Plasma here is principally of solar wind origin. It enters mainly through the magnetosphere's tail and drifts sunwards to the near-Earth region under the influence of the cross-tail electric field. Some plasma also enters on the day side when the solar wind and terrestrial magnetic field merge in a process called re-connection. As plasma moves sunwards from the tail, it is heated adiabatically because it moves to regions of higher magnetic field strength and onto shorter magnetic field lines. In addition, sudden re-connection events in the tail can transfer large amounts of magnetic energy to the plasma which is injected into the near-Earth region. These active periods are called substorms and are detectable on the ground as magnetic disturbances. Hence there is a strong link between hot plasma and high K_p and AE (Auroral Electrojet) indices. The injected plasma drifts from the region around midnight MLT, westwards (towards dusk) for the ions and eastwards (towards dawn) for the electrons.

Like the plasmapause, the magnetopause is a dynamic boundary. Its location is controlled by the balance between the ram pressure of the flowing solar wind and the magnetic pressure of the terrestrial magnetic field. Along the Earth-Sun line, the magnetopause is closest to the Earth and its position can be expressed approximately [RD8.8] as:

$$L_m = \left(rac{B_0^2}{\mu_0 n m V^2}
ight)^{1/6}$$

where

 L_m is the distance from the centre of the Earth to the magnetopause, at the subsolar point, in Earth-radii;

 B_0 is the strength of the terrestrial internal magnetic field, at surface of the Earth, on the equator = 3 \times 10 4 nT;



 μ_0 is the permeability of free space; n is the density of the solar wind; m is the mass of the proton; V is the velocity of the solar wind.

 L_m is typically 10 Earth-radii away from the subsolar point, the magnetopause flares out on the flanks and is effectively infinite in length in the anti-solar direction. This boundary is described in more detail in clause 5.

8.4.2 Effects

Magnetospheric electrons accumulate on exposed spacecraft surfaces, causing a net current which makes the surface charge negatively. Opposing currents exist which usually prevent significant charging levels, but if these are not sufficient, the spacecraft can charge to hundreds or thousands of volts. Different spacecraft surfaces can charge to different levels and so the possibility of damaging electrostatic discharges exists. A discussion of the factors contributing to charging is contained in annex F, along with typical charging levels associated with various materials. Because the intense, high-temperature electrons produced in substorms are usually required, conditions conducive to hazardous charging levels occur mainly in the midnight to dawn quadrant of local time and preferentially around the equinoxes. The regularity with which a spacecraft experiences charging depends on its electrical, geometric and surface composition characteristics. For the geostationary ATS-5 and -6 satellites, the probability of charging to greater than $-10~\mathrm{kV}$ during one pass from $00~\mathrm{LT}$ to $06~\mathrm{LT}$ was between 6~% and 12% [RD8.9]. NASA has defined a severe charging environment [RD8.10] based on the 90th percentile of severe environments. However, this is not the one adopted as the ECSS Standard. (See annex F for more details.)

Internal, or deep dielectric charging, is discussed in clause 9 since it is due to energetic electrons not normally considered as part of the plasma population.

8.4.3 **Models**

The injection of heated plasma during substorms makes the outer magnetosphere highly dynamic. There are no standard models to describe this region and the standard approach for most engineering purposes is to use worst-case environments.

Garret and DeForest [RD8.11] created a comprehensive model of electron and ion and electron plasma parameters for geostationary orbit. This is not a true empirical model because the source data were selected from periods of frequent substorm injection events but is useful for charging simulations. The model provides bi-Maxwellian descriptions of ions and electron distributions versus magnetic local time and A_p . This representation is convenient for input to a spacecraft charging code such as NASCAP [RD8.12].

The single Maxwellian distribution is:

$$f(v) = 4\pi n \left(\frac{m}{2\pi kT}\right)^{3/2} v^2 \exp(-v^2 m/2kT)$$

where

n is the density;v is the velocity;

k is the Boltzmann constant;

T is the temperature.

8.4.4 Typical and worst case parameters

Table 20 gives typical plasma parameters for the geostationary environment for quiet and substorm periods.



For assessment of surface charging, the following worst-case environment shall be used with the NASCAP [RD8.12] charging code or an equivalent code or calculations, applicable to the high altitude environment. It shall apply for all altitudes between the plasmapause and the magnetopause as defined in clause 5, i.e. between about L=4 Earth-radii and L=10 Earth-radii. This is listed in Table 21. This is a double-Maxwellian fit to an extremely severe event observed by the SCA-THA spacecraft on 24 April 1979 [RD8.13], when the spacecraft charged to -8 kV in sunlight. It should be noted that although the listed ion and electron densities are not equal, electrical neutrality is maintained by less energetic plasma which is not involved in the charging process and so not listed.

Table 20: Typical plasma parameters at geostationary orbit

	Density (cm ⁻³)	Ion temperature	Electron temperature	λ (m)
Quiet	10	1 eV-1 keV	1 eV-1 keV	50
Substorm	1	10 keV	$10~{ m keV}$	500

Table 21: Standard worst-case bi-Maxwellian environment

	Electron density (cm ⁻³⁾	Electron temperature (keV)	Ion density (cm ⁻³)	Ion temperature (keV)
Population 1	0,2	0,4	0,6	0,2
Population 2	1,2	27,5	1,3	28,0

8.5 The solar wind

8.5.1 Description

The solar wind is part of the Corona, the Sun's outer atmosphere. The high temperature of the plasma near the Sun causes it to expand outwards against gravity, carrying the solar magnetic field along with it. The solar wind starts at the Sun as a hot, dense, slowly moving plasma but accelerates outwards to become cool, rare and supersonic near the Earth. Most of the solar wind's acceleration takes place near the Sun and so Earth-orbiting satellites do not observe noticeable differences in velocity as their distance from the Sun varies.

The solar wind velocity typically lies in the range 300 km/s-800 km/s. It is most commonly around 400 km/s but there are frequent high-speed streams with velocities around 700 km/s. These streams are believed to originate from open magnetic field regions on the Sun, called coronal holes and are more commonly observed around solar minimum. They recur generally with a 27-day period as the coronal hole co-rotates with the solar surface. The strong variability of the solar wind is the driving force putting energy into the magnetosphere and ultimately causing surface charging and radiation effects. More severe but less frequent disturbances in the solar wind can be caused by coronal mass ejections.

At the Earth the presence of the magnetopause causes the supersonic solar wind to decelerate abruptly i.e. a shock wave is formed. At this "bow shock" the solar wind is slowed, compressed, heated and deflected. This shock typically lies 3 Earth-radii upstream of the magnetopause on the Earth-Sun line.

8.5.2 Effects

Although solar wind plasma is cold, the ions carry considerable kinetic energy, typically \sim 1 keV for protons and \sim 4 keV for He⁺⁺. This can result in sputtering



from surface materials. In the magnetosheath kinetic energy is lower, but temperature is higher, so sputtering still occurs. Because solar wind flow is highly directional, it acts as a very small non-gravitational perturbation to spacecraft trajectories but this effect is negligible compared to photon radiation pressure.

8.5.3 **Models**

Because the solar wind flows past the Earth with negligible modification, unless it encounters the bow shock, it can be considered spatially uniform in the vicinity of the Earth. For scoping studies of solar wind parameters, a flowing Maxwellian distribution shall be used, with density and temperature given in Table 22.

Table 22: Solar wind parameters (from RD8.14)

Parameter	Mean	5-95 % Range
Speed (km s ⁻¹)	468	320 - 710
Density (cm ⁻³)	8,7	3,2 - 20
T_{p} (K)	$1,2 imes 10^5$	$1 imes10^4$ – $3 imes10^5$
$T_{\rm e}$ (K)	$1.0 imes 10^5$	$9 imes10^4$ – $2 imes10^5$
N_{alpha}/N_{proton}	0,047	0,017 - 0,078

Average and extreme solar wind parameters are shown in Table 22.

Magnetosheath plasma parameters differ according to the latitude and local time of the observation. The highest density and temperature and the steepest velocity drop are observed at the subsolar point i.e. zero degrees latitude at local noon. Typical values for this region are given in Table 23.

Table 23: Typical magnetosheath plasma parameters (from RD8.14)

Local time	Speed (km/s)	<i>T</i> _p (K)	<i>T</i> _e (K)	Density (cm ⁻³)
12 noon	50	$2 imes10^6$	$2 imes 10^6$	35
06 hours	350	$1 imes 10^6$	$1 imes 10^6$	20

8.6 Induced environments

8.6.1 Description

The natural plasma environment can be augmented by a number of sources inside or on the satellite surface.

Under the influence of photoelectrons and secondary electrons, emitted due to impacting photons, electrons and, to a lesser extent, ions, many satellites charge a few volts positive. In this situation, the emitted electrons form a low-energy cloud which surrounds the spacecraft to a distance determined by the Debye length. The temperature of this population is determined by the secondary and photoemission spectra and is typically 2 eV to 5 eV. The density is determined by the spacecraft potential. This population can obscure measurement of the natural low-energy electron population. Instruments looking at this population should be placed on booms.

High-energy electron and ion populations can be generated by active experiments, i.e. electron and ion guns. These can be used to control surface charging or as a probe of the magnetic field. An ion thruster is a particularly high-flux ion gun.



Low-energy ion populations can be generated by ionization of contaminant gasses i.e. those released from the spacecraft by "outgassing", emitted by thrusters, including ion thrusters and sputtered off the surface due to ion impacts. These contamination processes are described in clause 11.

8.6.2 Effects

Once outside the spacecraft, neutral atoms produced by outgassing and sputtering can be ionized by sunlight or charge-exchange with other ions, to create a low-energy (<10 eV) ion population. These ions can be drawn to negatively charged surfaces and can adhere. This coating can alter optical properties e.g. of mirrors or solar panel covers, or change the secondary and photoemission yields and the susceptibility to surface charging. Within the spacecraft. e.g. in electronics boxes, residual gasses can facilitate electrostatic discharges from high voltage components.

8.6.3 **Models**

8.6.3.1 Photo- and secondary electrons

The electron density at the spacecraft surface shall be determined from the incident UV and primary electron fluxes, multiplied by the yield for the surface in question. Away from the emitting surface the density shall be calculated from the following [RD8.15]:

$$rac{N}{N_0} = \left(1 + rac{z}{\sqrt{2}\lambda_0}
ight)^{-2}$$

where

N is the density (cm⁻³);

 N_0 is the density at emitter (cm⁻³); z is the distance from surface;

 λ_0 is the shielding distance, calculated as the Debye length due to the

emitted electrons.

8.6.3.2 Ionization of Contaminant Gasses

Once neutral gas is released into space by whatever mechanism, it becomes subject to photoionization and dissociation by solar UV and ionization by charge exchange with solar wind ions. Production of new ions can be calculated from the appropriate photoionization rates and charge exchange cross-sections.

$$Q = N_i(\nu + \sigma n_{SW} \nu_{SW})$$

from RD8.16 where

Q is the production rate, ions s⁻¹;

 N_i is the ion density;

v is the photoionization rate coefficient;

 n_{sw} and v_{sw} are the solar wind density and velocity;

 σ is the charge exchange coefficient.

Photoionisation rates depends on the atom or molecule concerned, and UV intensity and spectrum. Huebner and Giguere [RD8.17] have tabulated a number of rate coefficients for different species, for sunlight at 1 AU. As an example, some photoionization rates for common gasses are listed in Table 24.



Table 24: Some solar UV photoionization rates at 1 AU (from RD8.17)

Species	Photoionization rate (s ⁻¹)
H ₂ O	$3,34 imes 10^{-7}$
O_2	$5{,}13 imes 10^{-7}$
N_2	$3,\!52 imes 10^{-7}$

For H_2O , where sigma is around $2.1 \times 10^{-19}\,\text{m}^{-2}$ [RD8.16], photoionization and charge exchange are comparable processes. However, all species and dissociation products shall be considered to calculate the total production of emitted ions.

8.6.4 Typical parameters

Table 25 gives typical photoelectron sheath parameters [RD8.18].

Table 25: Photoelectron sheath parameters

Temperature (eV)	Photoelectron current (A m ⁻²)	Surface electron density (m ⁻³)
3	$1 imes 10^{-5}$	$1 imes 10^8$

8.7 Tailoring guidelines

Tailoring of this Standard to apply to specific missions shall be done by consideration of the different regions of space traversed by the spacecraft under consideration. Induced plasma can be seen in all orbits but the natural plasma populations depend strongly on orbit. Some typical examples of plasma regimes to be considered, are given in Table 26.

Table 26: Examples of appropriate plasma environments for different missions

	11115510115	
Orbit	Regions encountered	Problems to be addressed
LEO e.g. Mir	Ionosphere excluding auroral zone.	Power leakage, high spacecraft
and Space		"ground" potential, ram/wake
station		effects.
Polar LEO	Ionosphere including auroral zone.	Power leakage, high spacecraft
		"ground" potential, ram/wake
		effects, surface charging.
Geostationary	Outer magnetosphere, with rare	Surface charging.
orbit	occasions when the plasmasphere,	
	magnetosheath and even solar wind	
	are encountered.	
Geostationary	Ionosphere, excluding auroral zone,	Power leakage, high spacecraft
transfer orbit	plasmasphere, outer magnetosphere,	"ground" potential, ram/wake
	with rare occasions when	effects, surface charging.
	magnetosheath and even solar wind	
	are encountered.	
High altitude	All regions can be encountered,	Power leakage, high spacecraft
elliptical orbit	depending on orbit.	"ground" potential, ram/wake
		effects, surface charging.



8.8 References

- RD8.1 NASA TM 4527, "Natural Orbital Environmental Guidelines for Use in Aerospace Vehicle Development", Eds. B.J. Anderson and R.E. Smith, 1994.
- RD8.2 Bilitza D, "International reference ionosphere status 1995/96", Advances in Space Research, 20, 9, pp.1751–1754.
- RD8.3 "Space Environment for USAF Space Vehicles", MIL-STD-1809 (USAF), 15 Feb 1991.
- RD8.4 Yeh H.-C. and M.S. Gussenhoven, "The statistical Electron Environment for Defense Meteorological Satellite Program Eclipse Charging", J. Geophys. Res., pp.7705-7715, 1987.
- RD8.5 Gussenhoven M.S, D.A. Hardy, F. Rich, W.J. Burke and H.-C. Yeh, "High-Level Spacecraft Charging in the Low-Altitude Polar Auroral Environment", J. Geophys. Res., pp.11009-11023, 1985.
- RD8.6 Lilley J.R., D.L. Cooke, G.A. Jongeward and I. Katz, "POLAR User's Manual", AFGL-TR-85-0246.
- RD8.7 Carpenter D.L. and R.R. Anderson, "An ISEE/Whistler Model of Equatorial Electron Density in the Magnetosphere", J. Geophys. Res., 97, p.1097, 1992.
- RD8.8 Burke W.J., D.A. Hardy and R.P. Vancour, "Magnetospheric and High Latitude Ionospheric Electrodynamics", Chapter 8 of "Handbook of Geophysics and the Space Environment", Ed. A. Uram, USAF, 1985.
- RD8.9 Grard R., K. Knott and A. Pedersen, "Spacecraft Charging Effects", Space Sci. Rev., 34, p.289, 1983.
- RD8.10 Purvis C.K, H.B. Garrett, A.C. Whittlesey and N.J. Stevens, "Design Guidelines for Assessing and Controlling Spacecraft Charging Effects", NASA TP-2361, 1984.
- RD8.11 Garrett H.B. and S.E. DeForest, "An Analytical Simulation of the Geosynchronous Plasma Environment", Planet. Space Sci., 27, p.1101, 1979.
- RD8.12 Katz I., J.J. Cassidy, M.J. Mandell, G.W. Schnuelle, P.G. Steen and J.C. Roche, "The Capabilities of the NASA Charging Analyzer Program", in "Spacecraft Charging Technology 1978", Eds. R.C. Finke and C.P. Pike, NASA CP–2071/AFGL TR–79–0082, ADA045459, p.101, 1979.
- RD8.13 Gussenhoven M.S and E.G. Mullen, "Geosynchronous Environment for Severe Spacecraft Charging", J. Spacecraft and Rockets 20, p.26, 1988.
- RD8.14 Feynman J, "Solar Wind", Chapter 3 of "Handbook of Geophysics and the Space Environment", Ed. A.Juram, USAF, 1985.
- RD8.15 Grard R.J.L. and J.K.E. Tunaley, "Photo Electron Sheath Near a planar Probe in Interplanetary Space", J. Geophys. Res., 76, p.2498, 1971.
- RD8.16 Huddleston D.E., A.D. Johnstone and A.J. Coates, "Determination of Comet Halley Gas Emission Characteristics from Mass Loading of the Solar Wind", J. Geophys. Res., 95, p.21, 1990.
- RD8.17 Huebner W.F. and P.T. Giguere, "A Model of Comet Comae II. Effects of Solar Photodissociative Ionization", Astrophys. J., 238, p.753, 1980.
- RD8.18 Scialdone J.J., "An Estimate of the Outgassing of Space Payloads and Its Gaseous Influence on the Environment", J. Spacecraft and Rockets, 23, p.373, 1986.



Energetic particle radiation

9.1 Introduction – Overview of energetic particle radiation environment and effects

9.1.1 General

Radiation environments and effects shall be considered early in the design cycle. Energetic charged particles with energies in the MeV range are encountered throughout the Earth magnetosphere, in inter-planetary space, and in the magnetospheres of other planets. At pre-phase A, radiation environments are an element in trade-offs for orbit selection. Effects on both the payload and on the spacecraft carrier shall be considered. A radiation environment specification for a mission shall be established wherein all types of radiation shall be considered, reflecting general and mission-specific radiation susceptibilities.

9.1.2 Environments

9.1.2.1 Radiation belts

Energetic electrons and ions are magnetically trapped around the Earth forming the radiation belts, also known as the Van Allen belts. The radiation belts are crossed by low altitude orbits as well as high altitude orbits (geostationary and beyond). The radiation belts consist principally of electrons of up to a few MeV energy and protons of up to several hundred MeV energy. The so-called South Atlantic anomaly is the inner edge of the inner radiation belt encountered in low altitude orbits. The offset, tilted geomagnetic field brings the inner belt to its lowest altitudes in the South Atlantic region. More information can be found in references RD9.1. and RD9.2.

9.1.2.2 Solar energetic particles

Energetic solar eruptions (Solar Particle Events, SPEs) produce large fluxes of Solar Energetic Particles (SEPs) which are encountered in interplanetary space and close to the Earth. The Earth magnetic field provides a varying degree of geomagnetic shielding of near-Earth locations from these particles.



9.1.2.3 Galactic cosmic rays

There is a continuous flux of Galactic Cosmic Ray (GCR) ions. Although the flux is low (a few particles /cm²/sec), GCRs include energetic heavy ions which can deposit significant amounts of energy in sensitive volumes and so cause problems.

9.1.2.4 Other planets

The above environments are common to planets other than the Earth. Jupiter and Saturn, in particular, have severe radiation environments. Mercury also has a small magnetosphere.

9.1.2.5 Secondary radiation

Secondary radiation is generated by the interaction of the above environmental components with materials of the spacecraft. A wide variety of secondary radiations are possible, of varying importance.

9.1.2.6 Other radiation sources

Other sources of radiation include neutrons resulting from energetic particle interactions with the upper atmosphere and emissions from on-board radioactive sources such as in Radioisotope Thermo-electric Generator (RTG) electrical power systems.

9.1.3 Effects survey

The above radiation environments represent important hazards to space missions. Energetic particles, particularly from the radiation belts and from solar particle events cause radiation damage to electronic components, solar cells and materials. They can easily penetrate typical spacecraft walls and deposit doses of hundreds of kilorads during missions in certain orbits.

Radiation is a concern for manned missions. Astronauts shall operate within defined limits of dose equivalent [RD9.3], determined to ensure as low as reasonably achievable long-term risk. There are many possible radiation effects to humans, beyond the scope of this document. These are described in RD9.4. To account for dependence of effects on particle species, energy and LET, dose is expressed as dose equivalent where energy, LET and species dependent factors are used to scale absorbed dose contributions. For example, heavy ions and neutrons are known to cause severe biological damage, and therefore these contributions receive a heavier weighting than gamma radiation. The "quality factors", as they are called, are established by the International Commission on Radiological Protection [RD9.5].

Energetic ions, primarily from cosmic rays and solar particle events, lose energy rapidly in materials, mainly through ionization. This energy transfer can disrupt or damage targets such as a living cell, or a memory element, leading to Single-event Upset (SEU) of a component, or an element of a detector (radiation background).

SEUs and biological effects can also arise from nuclear interactions between very energetic trapped protons and materials (sensitive parts of components, biological experiments, detectors). Here, the proton breaks the nucleus apart and the fragments cause highly-localized ionization.

Energetic particles also interfere with payloads, most notably with detectors on astronomy and observation missions where they produce a "background" signal which are not distinguishable from the photon signal being counted, or which can overload the detector system.

Energetic electrons can penetrate thin shields and build up static charge in internal dielectric materials such as cable and other insulation, circuit boards, and on ungrounded metallic parts. These can subsequently discharge, generating electromagnetic interference.



Apart from ionizing dose, particles can lose energy through non-ionizing interactions with materials, particularly through "displacement damage", or "bulk damage", where atoms are displaced from their original sites. This can alter the electrical, mechanical or optical properties of materials and is an important damage mechanism for electro-optical components (e.g. solar cells and opto-couplers) and for detectors, such as CCDs.

9.2 Quantification of effects and related environments

Models of the radiation environment are needed to assist in orbit selection, component selection and shielding optimization. In engineering a space system to operate in the space environment, it is necessary to relate the environment to system degradation quantitatively. This also involves questions of testing systems and their components for verification that they meet the performance requirements in the presence of the space environment.

For example, testing with calibrated radioactive sources can establish the threshold for functional failure or degradation of an electronic component in terms of *total absorbed dose* (often referred to simply as "total dose", or just "dose"). Radiation environment models, used together with mission orbital specifications can predict the dose and enable correct performance to be verified.

Table 27 gives the parameters which shall be used for quantification of the various radiation effects.

Although some of these parameters are readily derivable from a specification of the environment, others either need explicit consideration of test data (for example, SEU calculation) or the detailed consideration of interaction geometry and mechanisms (e.g. radiation background estimation).

In the following subclauses, the basic data on the environment are presented, along with models to be employed for deriving data beyond those presented. Effects and the specific methods for derivation of engineering quantities are presented.

Table 27: Parameters for quantification of radiation effects

Radiation effect	Parameter
Electronic component degradation	Total ionizing dose.
Material degradation	Total ionizing dose.
Material degradation (bulk	Non-ionizing dose (NIEL).
damage)	
CCD and sensor degradation	NIEL.
Solar cell degradation	NIEL and equivalent fluence.
SEU and latch-up	LET spectra (ions);
	proton energy spectra;
	explicit SEU/SEL rate of devices.
Sensor interference (background	Flux above above energy threshold
signals)	or flux threshold;
	explicit background rate.
Internal electrostatic charging	Electron flux and fluence;
	dielectric E-field.



9.3 Energetic particle radiation environment reference data, models and analysis methods

Figure 13 shows the ranges of electrons and protons in aluminium.

9.3.1 Trapped radiation belts

9.3.1.1 Basic data

Trapped radiation belt charged energetic particles gyrate in the geomagnetic field with a gyration period $t_c = 2\pi m/(eB)$ and a radius of gyration of $R_c = mv^2/(eB)$. Table 28 gives typical characteristics of energetic particles.

Table 28: Characteristics of typical radiation belt particles

	Par	Particle		
	1 MeV Electron	10 MeV Proton		
Range in aluminium (mm)	2	0,4		
Peak equatorial omni-directional flux (cm ⁻² s ⁻¹)*	4×10^6	$3,4 \times 10^{5}$		
Radial location (L) of peak flux $(Earth\text{-radii})^*$	4,4	1,7		
Radius of gyration (km)				
@ 500 km	0,6	50		
@ 20000 km	10	880		
Gyration period (s)				
@ 500 km	10 ⁻⁵	7×10^{-3}		
@ 20000 km	2×10^{-4}	0,13		
Bounce period (s)				
@ 500 km	0,1	0,65		
@ 20000 km	0,3	1,7		
Longitudinal drift period (min)				
@ 500 km	10	3		
@ 20000 km	3,5	1,1		

^{*} derived from the models of subclause 9.3.1.2

9.3.1.2 Standard models

For trapped radiation, the standard models of radiation belt energetic particle shall be the AE–8 and AP–8 models for electrons [RD9.6] and protons [RD9.7], respectively. They were developed at the NSSDC at NASA/GSFC based on data from satellites flown in the 1960s and early 1970s. The models give omni-directional fluxes as functions of idealized geomagnetic dipole coordinates B/B_0 and L (see clause 5). This means that they shall be used together with an orbit generator and geomagnetic field computation to give instantaneous or orbit-averaged fluxes. The user shall define an orbit, generate a trajectory, transform it to geomagnetic coordinates and access the radiation belt models to compute flux spectra. Apart from separate versions for solar maximum and solar minimum, there is no description of the temporal behaviour of fluxes. At high altitudes in particular (e.g. around geostationary orbit) fluxes vary by orders of magnitude over short times and exhibit significant diurnal variations; the models do not describe these. In addition, the models do not contain any explicit flux directionality.



At low altitudes, on the inner edge of the radiation belts, particle fluxes rise very steeply with altitude and small errors in computing locations can give rise to large errors in particle fluxes. This is a problem since the geomagnetic field is shifting and decaying so that the situation is no longer the same as when the model data were acquired. Use of a geomagnetic field model other than the one used in generating the model can result in large flux errors at low altitude. The models shall only be used together with the geomagnetic field models shown in Table 29.

Table 29: Standard field models to be used with radiation-belt models

Radiation-belt model	Geomagnetic field model
AE-8-MIN	Jensen-Cain 1960
AE-8-MAX	Jensen-Cain 1960
AP-8-MIN	Jensen-Cain 1960
AP-8-MAX	GSFC 12/66 extrapolated to 1970

Although use of an old field model and epoch can reduce errors in the magnitudes of fluxes, it should be noted that it does not model the spatial locations of radiation-belt features (e.g. the position of the South Atlantic anomaly), or particle fluxes, as they are today.

The particle ranges shown in Figure 13 show that in order to penetrate typical spacecraft shielding of the order of millimetres, protons need tens of MeV energies and electrons need in excess of about 0,5 MeV. The AP-8 model for protons gives proton fluxes from 0,1 to 400 MeV while the AE-8 model for electrons covers electrons from 0,04 to 7 MeV. Figure 14 shows contour plots of AE-8 and AP-8 model omnidirectional, integral fluxes for energies above 1 MeV and 10 MeV, respectively, in idealized dipole space.

Figure 15 shows values of energetic electron and proton particle fluxes as stored in these models, for positions on the geomagnetic equator $(B=B_0)$, as functions of L for both solar maximum and solar minimum. This shows that as far as the models are concerned, the solar activity only affects electron fluxes in the mid-L range and protons at low altitude where the higher neutral atmospheric density at solar maximum leads to reduced proton fluxes because of enhanced loss. Solar cycle effects on electrons appear to differ from this behaviour in reality [RD9.8].

9.3.1.3 The South Atlantic anomaly

The South Atlantic anomaly (see subclause 9.1.2.1) produces an "island" of radiation and provides the only significant radiation encountered on low Earth orbits with altitudes below about 800 km and inclinations below about 40°. Figure 16 shows the South Atlantic Anomaly at 400 km.

Anisotropy (the "East-West effect")

Because of the inclination of geomagnetic field-lines with respect to the atmosphere here, particles reaching a point from the West have gyrated from higher altitude while those arriving from the East have gyrated from lower altitude. There are fewer coming from below because of atmospheric absorption and therefore an asymmetry in the fluxes results. This can be important in certain cases, including the International Space Station. The current standard AP-8 model does not treat this effect but models have been developed by NASA [RD9.9] and BIRA [RD9.10]. Figure 17, from the BIRA ANISO model, shows the integral orbit-averaged flux of 100 MeV protons in the horizontal plane as a function of look-direction relative to North. The East and West "lobes" are clear. The ratio of the East and West peak fluxes is about 4,6. Measurements from MIR are also available which are consistent with this ratio [RD9.11].



Location of the South Atlantic anomaly

The slow movement of the South Atlantic anomaly as a result of shifts in the geomagnetic field has been clearly observed and agrees with expectation. This shift is essentially westward at a rate of 0.3° per year ($\sim 10^{\circ}$ since the models were created) and account shall be taken of this figure for low Earth orbits when planning operations which involve a sensitivity to radiation (payload radiation background, astronaut EVA). Models including this shift capability are available [RD9.12].

9.3.1.4 Dynamics of the outer radiation belt

The dynamic nature of the outer electron radiation belt, together with its diurnal variations mean that unless one is interested in long-term averages (such as provided by AE-8), some statistical description is desirable. This is especially true when deep dielectric charging and radiation background are of concern. No standard models for the variability are yet available, but for engineering purposes the CRRESELE model may be used [RD9.13]. An older version of the AE-8 electron model, AE-4 [RD9.14], included a statistical model giving standard deviations of the logarithm of electron fluxes (assumed to be normally-distributed). It also included a model for local time flux modulation. This was a sinusoidal model providing amplitudes of the variation, with a fixed maximum at 11:00 hours local time. These have been extended and applied to the AE-8 model [RD9.15], although this extension is unvalidated.

9.3.2 Solar particle event models

9.3.2.1 Standard model for mission-integrated fluences

During energetic events on the Sun, large fluxes of energetic protons are produced which can reach the Earth. Solar particle events, because of their unpredictability and large variability in magnitude, duration and spectral characteristics, have to be treated statistically. However, large events are confined to a 7-year period defined as solar maximum. Although large events are absent during the remaining 4 solar minimum years of the 11-year solar cycle (see clause 6) the occasional small event can still occur.

Figure 18, based on data from RD9.16, shows reference data for solar maximum solar proton fluences at various energy levels based on the JPL-1991 model. The data are also tabulated in Table 30.

This statistical model is based on data from 3 solar cycles. This shall be the standard model used for engineering consideration of time-integrated effects. Since this is a statistical model, a probability level shall be entered. On the basis of analysis of worst-case periods [RD9.17], the probability levels in Table 31 are recommended.

The JPL model provides data up to 60 MeV. For fluences at energies above this, an exponential fit to the rigidity spectrum shall be used, where rigidity is defined as:

$$P = \left(\frac{A}{Z}\right) \frac{(E^2 + 1862 E)^{1/2}}{10^3}$$

where

P is the rigidity, expressed in GV;E is the energy, expressed in MeV.



Table 30: Fluence levels for energy, mission duration and confidence levels from the JPL-1991 model

Energy (MeV)	Probability (confidence) level (%)	1 year (/cm ²)	2 years (/cm ²)	$3 ext{ years}$ $(/cm^2)$	5 years $(/cm^2)$	7 years (/cm ²)
>1	50	$5,92 \times 10^{10}$	$1,16 \times 10^{11}$	$1,72 \times 10^{11}$	$3,15 \times 10^{11}$	$3,99 \times 10^{11}$
>1	75	$8,76 \times 10^{10}$	$1,74 \times 10^{11}$	$2,42 \times 10^{11}$	$3,87 \times 10^{11}$	$4,77 \times 10^{11}$
>1	90	$1,26 \times 10^{11}$	$2{,}39\times10^{11}$	$3,25 \times 10^{11}$	$4,79 \times 10^{11}$	$5,89 \times 10^{11}$
>1	95	$1,64 \times 10^{11}$	$2,92 \times 10^{11}$	$3,96 \times 10^{11}$	$5,55 \times 10^{11}$	$6,95 \times 10^{11}$
>1	99	$2,91 \times 10^{11}$	$4,52 \times 10^{11}$	$5,89 \times 10^{11}$	$7,68 \times 10^{11}$	$1,00 \times 10^{12}$
>4	50	$8,00 \times 10^9$	$2,02 \times 10^{10}$	$3,33 \times 10^{10}$	$5,75 \times 10^{10}$	$8,84 \times 10^{10}$
>4	75	$1,69 \times 10^{10}$	$3,58 \times 10^{10}$	$5,74 \times 10^{10}$	$9,28 \times 10^{10}$	$1,27 \times 10^{11}$
>4	90	$3,46 \times 10^{10}$	$6,42 \times 10^{10}$	$9,81 \times 10^{10}$	$1,49 \times 10^{11}$	$1,96 \times 10^{11}$
>4	95	$5,49 \times 10^{10}$	$9,54 \times 10^{10}$	$1,40 \times 10^{11}$	$2,09 \times 10^{11}$	$2,70 \times 10^{11}$
>4	99	$1,50 \times 10^{11}$	$2,28 \times 10^{11}$	$3,10 \times 10^{11}$	$4,45 \times 10^{11}$	$5,63 \times 10^{11}$
>10	50	$2,11 \times 10^{9}$	$5,59 \times 10^{9}$	$9,83 \times 10^{9}$	$1,79 \times 10^{10}$	$2,78 \times 10^{10}$
>10	75	$5,34 \times 10^{9}$	$1,18 \times 10^{10}$	$1,85 \times 10^{10}$	$3,16 \times 10^{10}$	$4,70 \times 10^{10}$
>10	90	$1,\!25\times10^{10}$	$2,\!42\times10^{10}$	$3,41 \times 10^{10}$	$5,28 \times 10^{10}$	$7,55 \times 10^{10}$
>10	95	$2{,}12\times10^{10}$	$3,79\times10^{10}$	$5,19 \times 10^{10}$	$7,51 \times 10^{10}$	$1,05 \times 10^{11}$
>10	99	$5,88 \times 10^{10}$	$1,02 \times 10^{11}$	$1,31 \times 10^{11}$	$1,86 \times 10^{11}$	$2,36 \times 10^{11}$
>30	50	$4,50 \times 10^{8}$	$1,28 \times 10^{9}$	$2,22 \times 10^9$	$4,56 \times 10^{9}$	$6,61 \times 10^9$
>30	75	$1,23 \times 10^{9}$	$2,94 \times 10^{9}$	$4,67 \times 10^{9}$	$8,33 \times 10^{9}$	$1,16 \times 10^{10}$
>30	90	$3,19 \times 10^{9}$	$6,71 \times 10^9$	$1,00 \times 10^{10}$	$1,66 \times 10^{10}$	$2,24 \times 10^{10}$
>30	95	$5,81 \times 10^9$	$1,13 \times 10^{10}$	$1,66 \times 10^{10}$	$2,63 \times 10^{10}$	$3,52 \times 10^{10}$
>30	99	$1,93 \times 10^{10}$	$3,49 \times 10^{10}$	$4,83 \times 10^{10}$	$6,96 \times 10^{10}$	$9,04 \times 10^{10}$
>60	50	$1,67 \times 10^{8}$	$4,92 \times 10^{8}$	$9,18 \times 10^{8}$	$1,73 \times 10^{9}$	$2,85 \times 10^{9}$
>60	75	$4,93 \times 10^{8}$	$1,24 \times 10^{9}$	$2,11 \times 10^{9}$	$3,52 \times 10^{9}$	$5,26 \times 10^{9}$
>60	90	$1,37 \times 10^{9}$	$2,83 \times 10^{9}$	$4,39 \times 10^{9}$	$7,00 \times 10^{9}$	$1,01 \times 10^{10}$
>60	95	$2,61 \times 10^{9}$	$4,92 \times 10^{9}$	$7,36 \times 10^{9}$	$1,12 \times 10^{10}$	$1,53 \times 10^{10}$
>60	99	$9,20 \times 10^{9}$	$1,62 \times 10^{10}$	$2,\!26\times10^{10}$	$3,27 \times 10^{10}$	$4,\!25\times10^{10}$

Table 31: Standard probability (confidence) levels to be applied for various mission durations

Number of years of exposure	Probability level (%)
1	97
2	95
3	95
4	90
5	90
6	90
7	90



9.3.2.2 Spectrum of individual events

The August 1972 event produced a peak flux near the Earth in excess of 10^6 protons cm⁻² s⁻¹ above 10 MeV energy, while the October 1989 event produced a peak flux of about 10^5 protons cm⁻² s⁻¹. A fluence spectrum which is often used to represent a worst case flare, classified as "anomalously large" is based on the very large August 1972 event:

$$J(E) = 7,9 \times 10^{9} \exp\left\{\frac{30 - E}{26, 5}\right\}$$

with energy E in MeV and fluence J in protons cm⁻². The October 1989 event was the largest seen since August 1972 but had lower fluences at the medium energies. A fit to its differential fluence spectrum is given by a three-part power law:

$$J(E) = 1,2 \times 10^{11} \, E^{-1,7}$$
 for $E < 30 {\rm MeV}$
 $4,5 \times 10^{12} \, E^{-2,8}$ for $30 {\rm MeV} < E < 150 {\rm MeV}$
 $5,5 \times 10^9 \, E^{-1,45}$ for $E > 150 {\rm MeV}$

where E is in MeV and J is in protons cm⁻² MeV⁻¹.

Comparison of these two spectra reveals important points. Since flare spectra are variable, the worst-case event at one energy is not necessarily worst-case at another. The August 1972 event yield worst-case doses at most typical spacecraft shielding (1–10 mm) where particles of energy 10–70 MeV are most important. The October 1989 flare is apparently more severe at lower and higher energies. Lower energies are important for surface material and solar cell effects and the higher energies more important for nuclear interactions giving rise to certain types of background and SEUs. So the term "worst-case" is application dependent.

9.3.2.3 Event probabilities

Burrell, as reported in RD9.18, developed a modified Poisson statistic to describe the probability p of a number of events n occurring during a time t, based on a previously observed frequency of N during time T:

$$p(n,t; N,T) = \frac{\left\{ (n+N)! \left(t/T \right)^n \right\}}{\left\{ n!N! \left(1+t/T \right)^{N+n+1} \right\}}$$

In this equation, N=1 and T=7 for the anomalous class of flare, while for ordinary flares, N=24 and T=7. This is sometimes useful in considering numbers of events in contrast to the total fluence. Simple application of Poisson statistics is also useful.

9.3.2.4 Analysis of event records

The JPL-91 model provides data only for integrated effects analysis (e.g. dose, long-term degradation, total upset count). It is often necessary to consider instantaneous fluxes. For radiation background estimation for example, the fluxes are required above an energy threshold determined by sensor shielding and sensor sensitivity, and above a flux threshold determined by sensor signal-to-noise characteristics. Two reference environment data resources are available: the NASA OMNIWEB database [RD9.19], and the NOAA GOES [RD9.20] database. With these databases, the durations and magnitudes of events above energy and flux thresholds can be analysed. Both databases are available on the WWW and provide a comprehensive long-term database of measurements of the interplanetary environment. OMNIWEB contains a complete database of energetic proton data from the IMP series of spacecraft. The NOAA GOES satellites have returned energetic proton and electron data from geostationary orbit since January 1986. Further information is provided in annex G.



9.3.2.5 Solar particle event ions

For analysing single event upset rates during Solar Particle Events (SPEs), the CREME96 model shall be used. It can also be used for other applications where data on severe SPE conditions are needed, such as background estimation. CREME96 is described further in subclause 9.3.3. While the older CREME model contained models for the peak flux for various types of events, CREME96 contains models based on the October 1989 event. It provides models of energy spectrum, composition and LET spectrum for the worst week, worst day and peak 5 minutes. The older CREME model provided more choice of peak environments. However, some of the more severe options were unrealistic.

9.3.2.6 Other models

Other model developments, which can lead to updates of this Standard, are discussed in annex G. These developments relate to alternative statistical approaches and models for peak fluxes.

9.3.2.7 Directionality

Fluxes and fluences of solar energetic particles shall be assumed to be isotropic in interplanetary space. This is generally not true in near-Earth space due to geomagnetic shielding (see subclause 9.3.4).

9.3.3 Cosmic ray environment and effects models

9.3.3.1 General

Cosmic ray environment and effects models were originally created by Adams and co-workers at the U.S. Naval Research Laboratory [RD9.21], under the name CREME. They provided a comprehensive set of cosmic ray and flare ion LET and energy spectra, including treatment of geomagnetic shielding and material shielding. CREME also included upset rate computation based on the path-length distribution in a sensitive volume and also treated in a simple manner trapped proton-induced SEUs. CREME has been superseded by CREME96 [RD9.22]. The major differences are in the inclusion of a model of the cosmic ray environment and its solar-cycle modulation due to Nymmik et al. [RD9.23], improved geomagnetic shielding calculation, improved material shielding calculation and more realistic Solar Energetic Particle Event (SEPE) ion environments (see subclause 9.3.2.5). Cosmic ray fluxes are anti-correlated with solar activity so the highest cosmic ray fluxes occur at solar minimum. CREME96 shall be the standard model for cosmic ray environment assessment. It shall also be the standard for evaluation of single event effects from cosmic rays, from solar energetic particles and from energetic protons.

Figure 19 shows composite LET spectra for three CREME96 environments: the nominal solar minimum cosmic ray flux; the average flux for a "worst week" of a large SEPE; and the peak flux from a large SEPE. Three orbital situations, with different geomagnetic shielding, are shown: geostationary (which also applies to high altitudes and interplanetary), a polar orbit (900 km) and LEO (28°, 450 km). Ions from Z = 1 to Z = 92 shall be included and, in the absence of a reason to use another value, shielding of 1 g/cm² aluminium shall be assumed.

9.3.3.2 Directionality

Fluxes and fluences of solar energetic particles shall be assumed to be isotropic in interplanetary space. This is not true in near-Earth space due to geomagnetic shielding (see subclause 9.3.4).

9.3.4 Geomagnetic shielding

The Earth magnetic field partially shields near-Earth space from solar energetic particles and cosmic rays, an effect known as geomagnetic shielding. However, these particles can easily reach polar regions and high altitudes such as the geo-



stationary orbit. Geomagnetic shielding of protons is computed on the basis of the trajectory in geomagnetic B, L space (see clause 5).

At a given location in the field there are minimum cut-off energies necessary for ions to penetrate to that point. Størmer's theory gives a cut-off rigidity, P_c , for particle arrival at a point, depending on the point's geomagnetic R, λ coordinates and the angle of ion arrival from east, γ [RD9.24]:

$$P_c = \frac{\{M\cos^4\lambda\}}{\{R^2[1 + (1 - \cos^3(\lambda)\cos(\gamma))^{1/2}]^2\}}$$

M is the normalized dipole moment of the Earth. From this equation, it can be seen that cosmic rays penetrate the geomagnetic field more easily from the west ($\gamma=180^{\circ}$) than from the east ($\gamma=0$). The R, λ coordinates can be computed from B and L according to the method of Roberts [RD9.25]. For vertical arrival, the expression simplifies to:

$$P_c \sim$$
 = $\frac{16\cos^4(\lambda)}{R^2}$ = $\frac{16}{L^2}$ GV, since γ =90° and R = $L\cos^2{(\lambda)}$

An approximate value of 16 for the constant M/4 is used to fit with observed effective cut-offs. Magnetospheric disturbances, which often follow solar-flares or CMEs, can result in a lowering of cut-off; this has been described by Adams et al. [RD9.24] as:

$$\frac{\varDelta P_c}{P_c} = 0,54 \exp\!\left(-\frac{P_c}{2,9}\right)$$
 with P_c in units of GV.

Stassinopoulos and King [RD9.26] developed a model which has total cut-off at L=5. It assumes that no protons can penetrate to lower values. It can be shown that this model corresponds to a quiet magnetosphere vertical cut-off model excluding protons of E<200 MeV from L<5 Earth-radii. This model is adequate for most cases. However, in reality protons of lower energy can penetrate below L=5 with non-vertical arrival directions, especially in a disturbed magnetosphere where the geomagnetic shielding is weakened. For westward arrival at the L=5 geomagnetic equator in a disturbed magnetosphere, the energy cut-off can be as low 30 MeV.

For engineering purposes, geomagnetic cut-off shall not be applied to orbits spending more than 50 % of the orbit period above L = 5. Geomagnetic cut-off shall always be applied to orbits spending more than 75 % of their time below L = 5.

9.3.5 Spacecraft secondary radiation

For engineering purposes it is often only electron-induced bremsstrahlung radiation that is considered as a significant secondary source. In special cases other secondaries shall be considered.

In evaluating the radiation background effects in detector systems, it is often secondary radiation that is important. Because of heavy shielding removing primaries, veto systems which actively protect against counting primary-induced signals, or secondary radiation generated within the sensing band of an instrument. Most secondary radiation is emitted at the instant of interaction ("prompt") while some is emitted some time after a nucleus has been excited by an incoming particle (induced radioactivity).

In manned missions, secondary neutrons and other products can be important contributors to the radiological hazard.

By its nature, secondary radiation shall be analysed on a case-by-case basis, possibly through Monte-Carlo simulation. For engineering estimates of bremsstrahlung, the SHIELDOSE model shall be used (see subclause 9.4.2).



9.3.6 Neutrons

A low-level flux of neutrons of between $0.5~\rm cm^2~s^{-1}$ and $4~\rm cm^{-2}~s^{-1}$ is present at low altitudes due to cosmic ray interactions with the atmosphere. Neutrons are also generated by energetic particles undergoing nuclear interactions with the material of spacecraft. These neutrons shall be considered for manned missions. They also play a role in generating background in sensitive detector systems.

9.4 Analysis methods for derived quantities

9.4.1 **General**

The following analysis methods shall be used.

The environment models specified in 9.3 shall be used to generate the primary data described in subclause 9.2. The secondary data shall be derived as specified below:

9.4.2 Ionizing dose

The ionizing dose environment is represented by the dose-depth curve. This can provide dose as a function of shield thickness in planar geometry or as a function of spherical shielding about a point. The planar model is appropriate for surface materials or for locations near to a planar surface. In general, electronic components are not in such locations and a spherical model is recommended for general specification.

The SHIELDOSE model shall be used [RD9.27] for ionizing doses. Alternatively, a method which has been validated with respect to SHIELDOSE may be used. This method uses a pre-computed dataset of doses from electrons, electron-induced bremsstrahlung and protons, as derived from Monte-Carlo analysis. The doses are provided as functions of material shielding and incident electron and proton energy. The actual spectrum is folded with this data-set to yield the dose at a given depth, d:

$$D(d) = \sum_{E} f(E) D(E, d) \Delta E$$

Figure 20 shows this data-set. A computerized version of this procedure is available as described in annex G.

The reference geometrical configuration for the dose-depth curve shall be a solid aluminium sphere. The SHIELDOSE dataset represents a planar medium and the conversion is performed as follows [RD9.27]:

$$D_{sphere} = 2D_{plane} \Biggl\{ 1 - rac{d(\log D_{plane})}{d(\log (d))} \Biggr\}$$

This conversion is included in the computer version.

In cases where more careful analysis of the shielding of a component or other sensitive location is necessary, a sectoring calculation is often performed. This can be necessary if the doses computed from simple spherical shielding are incompatible with the specification of the allowable radiation dose. The sectoring method traces rays through the shielding in a large number of directions. Along each direction the derived shielding, together with the data on dose as a function of shielding depth, d, is used to find the omnidirectional 4π dose contribution, $D_i(d)$, from each direction, i. The contributions, weighted by the solid angle increment around the rays, Ω_i , are then summed:

$$D_{tot} = \sum_{i} \left(\frac{\Omega_{i}}{4\pi}\right) D_{i}(d)$$

If this procedure is used, it shall employ the spherical model for the dose-depth curve.



In some cases, it is efficient to derive a shielding distribution. This is the result of the ray-tracing described above and provides the distribution of encountered shielding p(d). This distribution can be folded with the dose depth curve to derive the total dose. The advantage of this method is that various dose calculations can be efficiently performed for one geometry as represented by the shielding distribution.

It is important to recognize that a shielding analysis in the presence of significant anisotropies (e.g. as in 9.3.1.3) in the environment can result in serious error if the environment is assumed to be isotropic. This assumption is implicit in the sectoring method defined above since all directional contributions are derived from a common "omnidirectional" dose-depth curve.

9.4.3 Reference orbital dose data

Figure 21 shows a summary of expected doses on circular equatorial orbits as a function of the orbit altitude, based on the standard models described in subclause 9.3. A spherical shield of 4 mm aluminium is assumed.

Figure 22 shows a summary of the doses expected for a selection of common orbit types, based on the standard models. A 1-year mission and spherical aluminium shielding of 4 mm radius is assumed. Dose from one years' accumulated solar energetic protons is also shown, with a confidence level of 95 % that a higher dose is not seen. More details of the doses are given in Figure 23 in the form of doses as functions of the radius of the aluminium shielding.

9.4.4 Single-event upset rate

The CREME/CREME96 method shall be used [RD9.21, RD9.22]. It is possible to make upset rate predictions only when details of the device under consideration are known, particularly the critical charge and the sensitive volume dimensions. If a device is uncharacterized, tests shall be performed.

The test data shall show the normalized upset rate as a function of ion LET in the range 1 MeV cm²/mg to 100 MeV cm²/mg and as a function of proton energy in the range 20–100 MeV. These data shall be used to make an estimate of the upset rate from trapped protons and solar protons using the two-parameter Bendel method [RD9.28], and of upsets due to galactic and solar ions using the method of CREME/CREME96. This latter shall be modified to account for the non-ideal upset rate as a function of ion LET derived from component test data [RD9.29] (the so-called "IRPP" method) as described below. This method has been implemented in CREME96. CREME96 also includes the two-parameter Bendel method. Alternative methods which have been thoroughly validated with respect to these methods may be applied.

To compute an upset rate for an electronic device or a detector from the predicted fluxes, device characteristics shall be specified, particularly the size of the sensitive volume and the critical charge, or equivalently, critical energy E_c , in the volume which results in upset or registers as a "count".

For SEUs resulting from direct ionization the rate is found by integrating over the composite differential ion LET (L) spectrum, f(L), and the distribution of pathlengths (l) for the sensitive volume, p(l) [RD9.21, RD9.29]:

$$U = rac{S}{4} \int\limits_{E_c/L_{max}}^{l_{max}} p(l) \int\limits_{E_c/l}^{L_{max}} f(L) \ dL \ dl$$

which approaches FS/4 in a very sensitive detector (where E_c is very small, so all particles cause upset). S is the total surface area of the sensitive volume and F is the integral omnidirectional flux. Normally, for electronic components, the limiting solution does not apply and the integral shall be evaluated. The integration limits are set by the sensitive volume dimensions and the critical energy E_c ; E_c/L_{max} is the shortest path capable of supporting upset, l_{max} is the maximum



path length, E_c/l is the minimum particle LET necessary to cause upset on a path length l and L_{max} is the maximum LET of the spectrum. Predicted upset rates are very sensitive to the integration limits which are established through testing. This sensitivity is a result of the fact that particle fluxes in the environment are strong functions of LET. This form for the upset calculation assumes that above a unique critical charge, all bits, of equal size, are upset. Testing shows that in general the upset cross-section (σ , rate × fluence) rises more gradually to a saturation cross-section, σ_0 , and a method of calculation accounting for this is to sum a step-wise set of differential upset-rate calculations:

$$U = \sum_{i} \left(\frac{\sigma_{i}}{\sigma_{0}} \right) \left(\frac{\Delta U}{\Delta L} \right)_{i} \quad \Delta L = \sum_{i} \left(\frac{\sigma_{i}}{\sigma_{0}} \right) \Delta U_{i}$$

where each U_i is calculated using the respective (σ_i and L_i).

An estimate of the upset rate from nuclear interactions of energetic protons can be obtained by integration of the product of the measured proton-induced upset cross section $\sigma(E)$ and the differential proton flux f(E) over all energies. $\sigma(E)$ can be derived directly from the test data, or the two-parameter Bendel fit can be used. Simulations of proton nuclear interactions can also be used to derive $\sigma(E)$, when data from heavy-ion testing is available to provide the critical charge and sensitive volume dimensions [RD9.28].

9.4.5 Solar cell degradation

The EQFRUX-Si or EQFRUX-Ga models shall be used for silicon and gallium arsenide solar cell degradation calculations, respectively [RD9.30]. In the absence of other test data, it shall be assumed that 10 MeV protons cause equivalent damage to 3000 1 MeV electrons in silicon cells. Similarly it shall be assumed for gallium arsenide cells that the damage equivalence of a 10 MeV proton is 400, 1000 and 1400 1 MeV electrons for short-circuit current, maximum power and open-circuit voltage degradation, respectively. Since the default in these models is the assumption of infinite rear-side shielding of cells, this shall be the standard way of reporting results. However, account shall then be explicitly taken of radiation penetration though the rear-side of solar arrays.

9.4.6 Internal electrostatic charging

Engineering methods for specifying derived parameters related to internal electrostatic charging are currently under development and are described in annex G. The flux of energetic electrons is clearly important, as are the energy spectrum and the duration of high-flux conditions. In addition, the "target" material plays a role and shielding of the target material obviously has a large effect.

9.4.7 Dose-equivalent

Dose equivalent calculation, for astronaut hazard estimation shall employ the quality factors defined in document RD9.5. For ions, the quality factor, Q, depends on the ion LET, L, as shown in Figure 24. Dose-equivalent is derived from:

$$D_{eq} = \sum D \ Q(L)$$

where the sum is over all energies and radiation types. Electrons and gammarays have Q of 1. Protons have a Q of between 1 and 5 (the latter because of the nuclear interaction effects). Neutrons have Q between 5 and 20, depending on energy [RD9.5].



9.4.8 Non-ionizing dose

Damage to CCDs and other electro-optical components susceptible to displacement damage shall employ the NIEL function, N(E) [RD9.31], shown in Figure 25, to derive a 10 MeV equivalent proton damage fluence F_D :

$$F_D = \sum_E f(E) \, N_{10}(E) \, \Delta E$$

or a non-ionizing dose, D_N :

$$D_N = \sum_E f(E) N(E) \Delta E$$

where

f(E) is the differential fluence spectrum;

N(E) is the NIEL function;

 $N_{10}(E)$ is the NIEL function normalized to 10 MeV;

 ΔE is the energy step of the sum.

9.5 Tailoring guidelines: Orbital and mission regimes

9.5.1 General

In the following subclauses, attention is drawn to special considerations for various orbit types.

9.5.2 Geostationary orbit

Geostationary orbit is a circular orbit usually encountering an environment dominated by energetic electrons. This environment is characterized by strong time variations with many extended quiet periods of low radiation levels and many episodes of intense injections of energetic electrons which increase e.g. dose, sensor interference and electrostatic charging. Solar protons and cosmic rays have unrestricted access to this orbit. Solar particles make short-lived but important contributions to the total dose, interference and single event effects. They do not directly participate in charging processes. Cosmic rays provide a continuous source of single-event effects and sensor interference.

9.5.3 MEO, HEO

These orbits encounter the electron-dominated environment mentioned above, but in addition, encounter the inner, proton radiation belt. In such orbits, single-event effects from protons and proton non-ionizing damage need to be considered. These orbits often encounter more severe electron environments, near the peak of the electron belt (the location of which is also variable) than geostationary orbit and so electrostatic charging can be a more serious threat.

9.5.4 LEO

Current technology limits manned activities to low (< 550 km) and medium-inclination (~ 55°) orbits, however, this can improve in the future. We refer to these orbital regimes as LEO. Missions in these orbits encounter the inner edge of the radiation belt. This region is dominated by the South Atlantic anomaly. Also important is the strong asymmetry in fluxes from East and West. The low-altitude environment is characterized by high-energy radiation-belt trapped protons. The deflection of charged particles from outside the magnetosphere by the Earth magnetic field (geomagnetic shielding) reduces the fluxes of cosmic rays and solar energetic particles, but the shielding is not total. Like polar orbits, LEO orbits also encounter outer-belt trapped electrons at high-latitudes.



9.5.5 Polar

Polar orbits are generally of less than 1000 km altitude with inclinations above 80°. They encounter the inner proton and electron belts in the form of the South Atlantic anomaly and also the outer electron belt where the geomagnetic field lines bring it to low altitudes at "auroral" latitudes above about 50°. On the high-latitude parts of the orbit a spacecraft is exposed to almost unattenuated fluxes of cosmic rays and solar energetic particles. At low latitudes, geomagnetic shielding considerably reduces these fluxes.

9.5.6 Interplanetary and planetary environments

The interplanetary environment is characterized by cosmic rays and occasional solar energetic particle events. The variations in particle intensities with heliocentric radius and solar cycle modulation shall be considered. Missions to the giant planets shall consider their intense magnetospheres. Mercury also has a small magnetosphere. Science missions also take place at the Lagrangian points of the Sun-Earth system or Earth-Moon system. These locations can also be considered interplanetary from the point of view of the radiation environment.

9.6 Preparation of a radiation environment specification

A specification of the expected radiation environment of a space system shall be established at Phase A. The specification shall include:

- a. Unshielded mission-average proton and electron energy spectra from trapped radiation.
- b. The unshielded fluence spectrum of solar protons for the complete mission. Appropriate geomagnetic shielding shall be applied.
- c. Unshielded worst-case instantaneous energy spectra of trapped electrons, trapped protons and solar energetic protons (geomagnetically shielded) for the mission, for internal charging and sensor interference analysis.
- d. The ion LET spectrum for the appropriate solar cycle phase, together with a 10 % worst-case LET spectrum. A LET spectrum from a 10 % worst-case solar particle event with mean composition shall be included. The LET spectra shall include contributions from all ions from Z=1 to Z=92. Appropriate geomagnetic shielding shall be applied. Appropriate material shielding shall be applied. If no justification is available for another value, $1~\rm g/cm^2$ of aluminium shielding shall be used.
- e. A mission dose vs. shielding depth curve or table for dose at the centre of a solid aluminium sphere, including contributions from trapped electrons and protons, solar energetic protons and electron-induced bremsstrahlung.
- f. For manned missions, the above environment shall also be transformed into dose-equivalent.
- g. Damage-equivalent fluences of 1 MeV electrons and 10 MeV protons for solar cell damage estimates; this is generally possible for silicon and gallium arsenide cells as a function of cover-glass thickness, but should be revised for other technologies as a result of cell selection.
- h. NIEL (non-ionizing energy loss) 10 MeV equivalent fluences for CCD, optoelectronic and optical components as a function of spherical shielding depth.
- Orbital time-behaviour of radiation-belt, cosmic ray and solar energetic particle fluxes if the mission has a susceptibility to radiation background in sensors.
- j. Additions to the above environments from on-board nuclear sources.

The specification shall take account of the evolution of the mission orbit, either naturally or deliberately. This can have significant effects on radiation-belt exposure (e.g. due to natural perigee rise and apogee fall).



Operations which result in geo-synchronization of the orbit shall be considered (e.g. geostationary, apogee longitude maintenance of near-synchronous HEO orbits). In such missions radiation belt exposures are not averaged out.

9.7 Figures

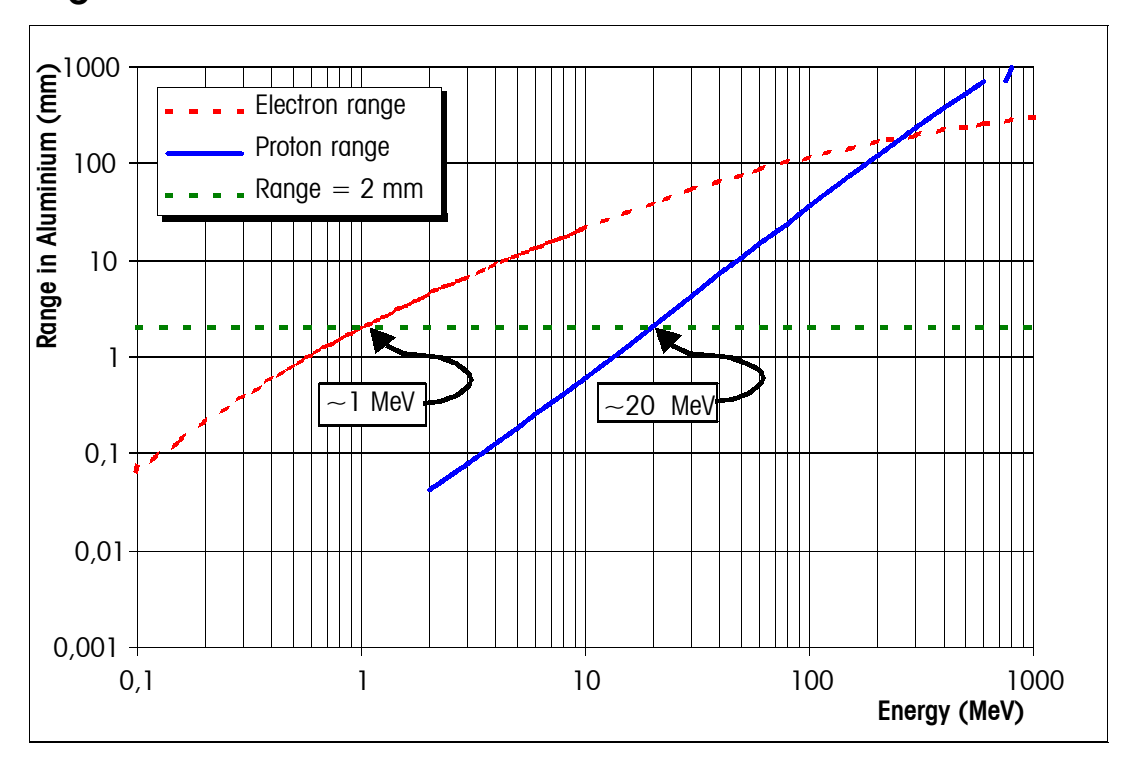
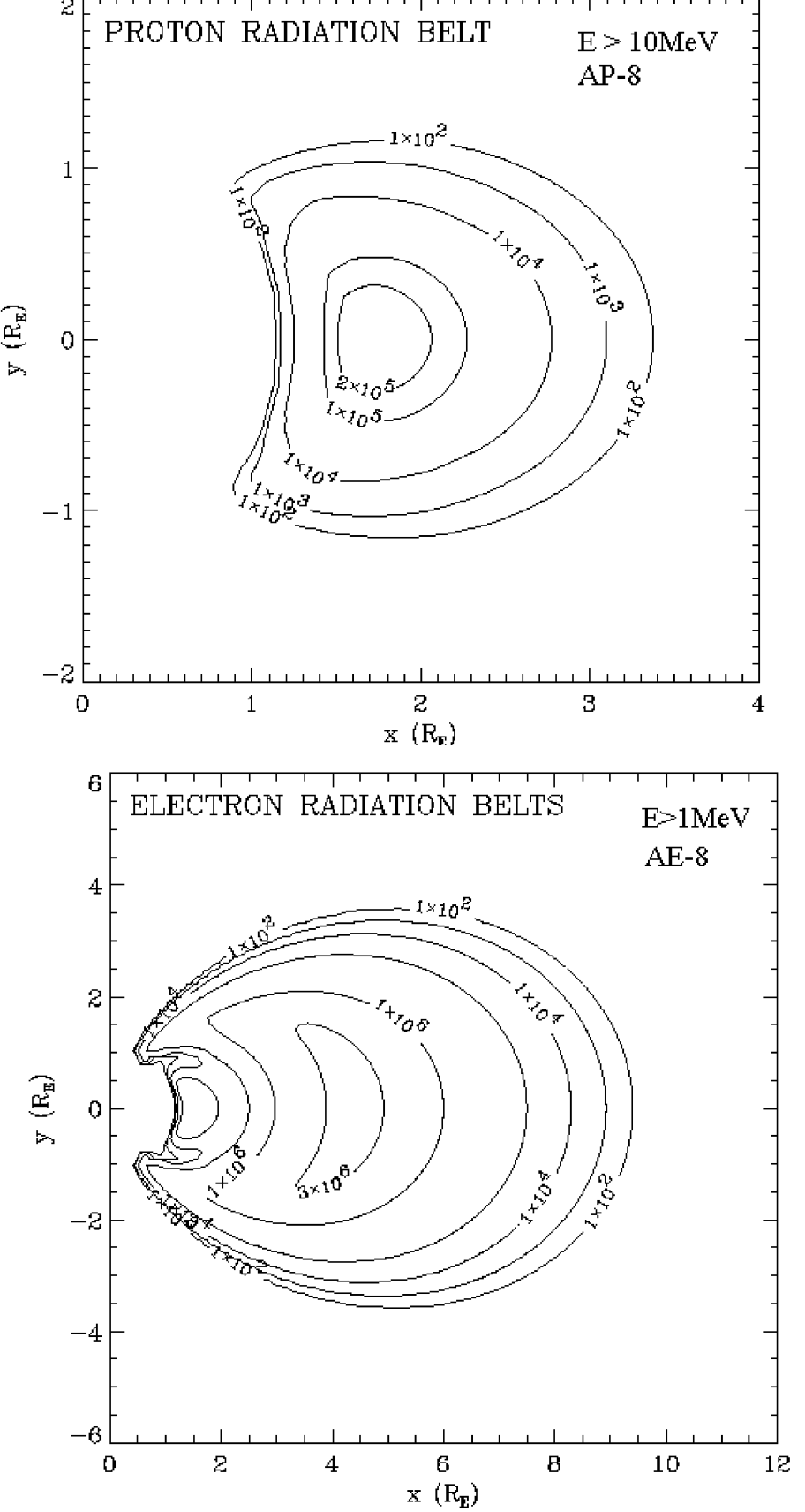


Figure 13: Mean ranges of protons and electrons in aluminium



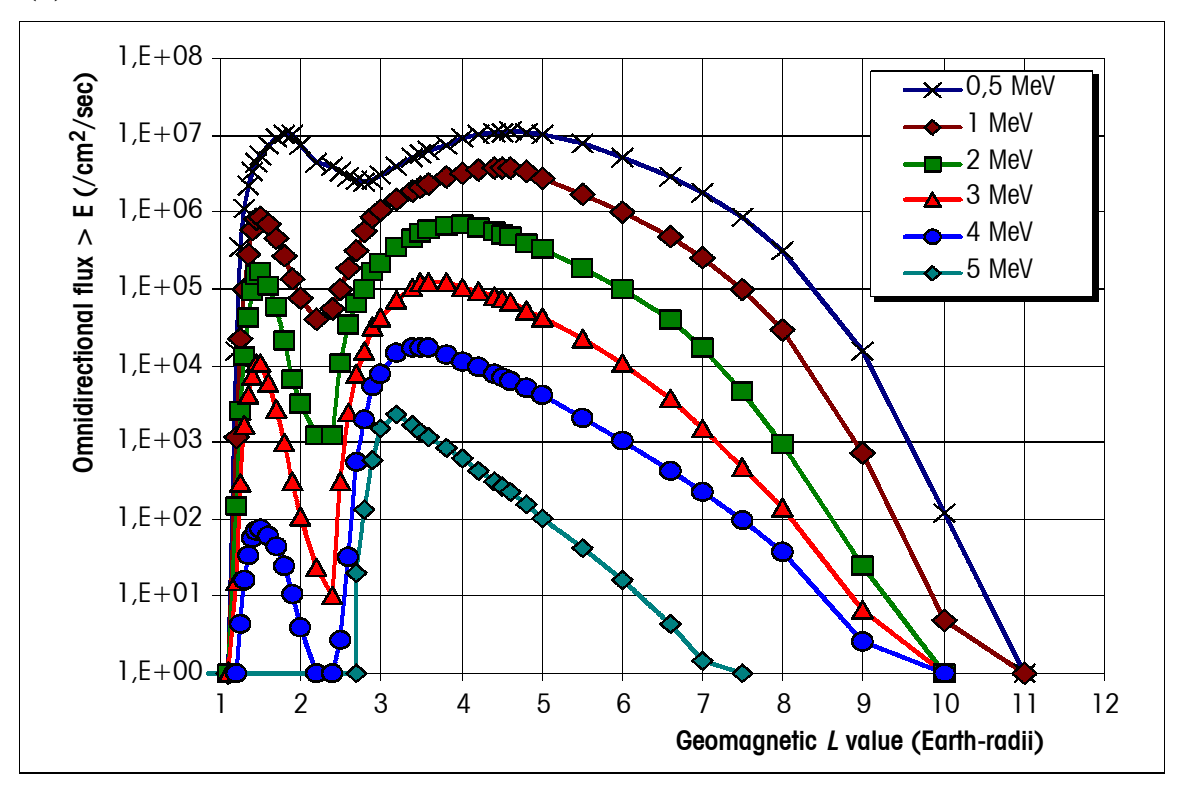


Omnidirectional fluxes are for particles >1 MeV and >10 MeV, respectively. The data are derived from the AE-8 and AP-8 models, respectively, and are shown in an ideal dipole representation of the Earth field.

Figure 14: Contour plots of the electron and proton radiation belts



(a) Electron



(b) Proton

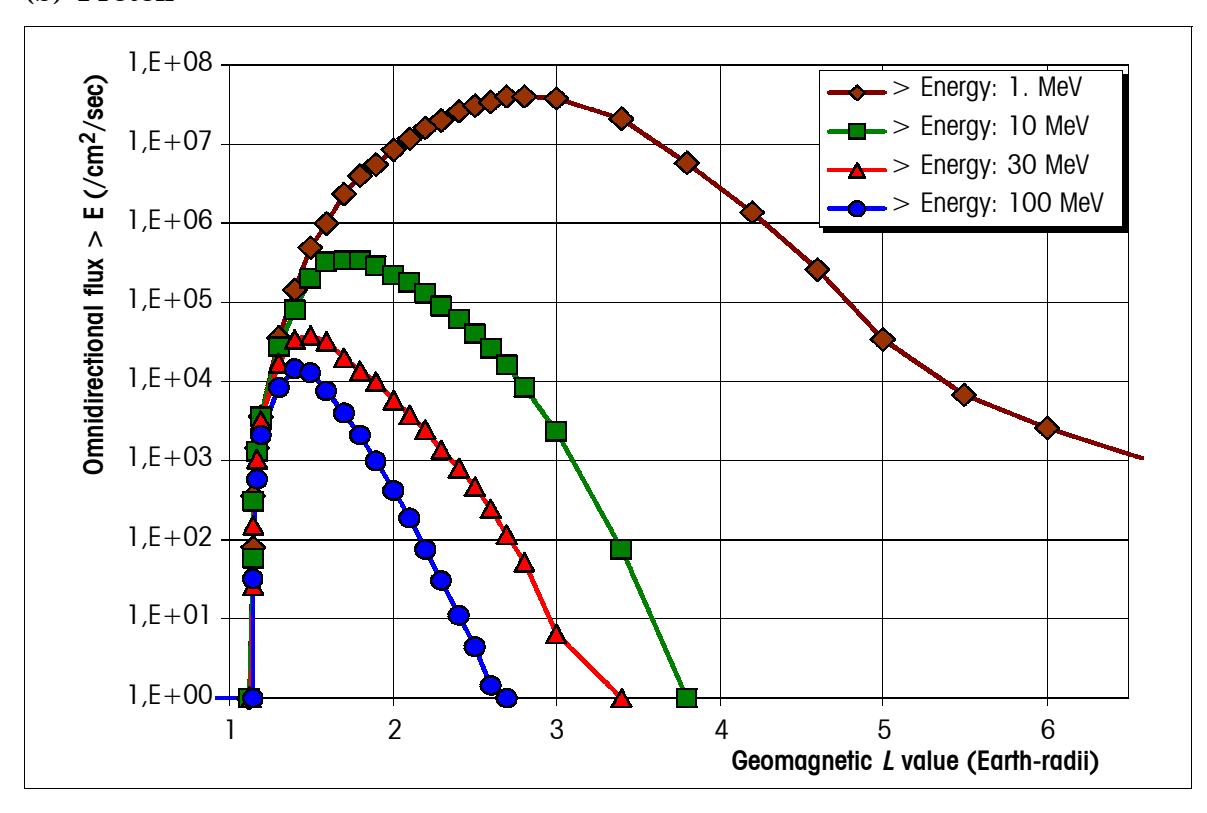


Figure 15: Electron (a) and proton (b) omnidirectional fluxes, integral in energy, on the geomagnetic equator for various energy thresholds



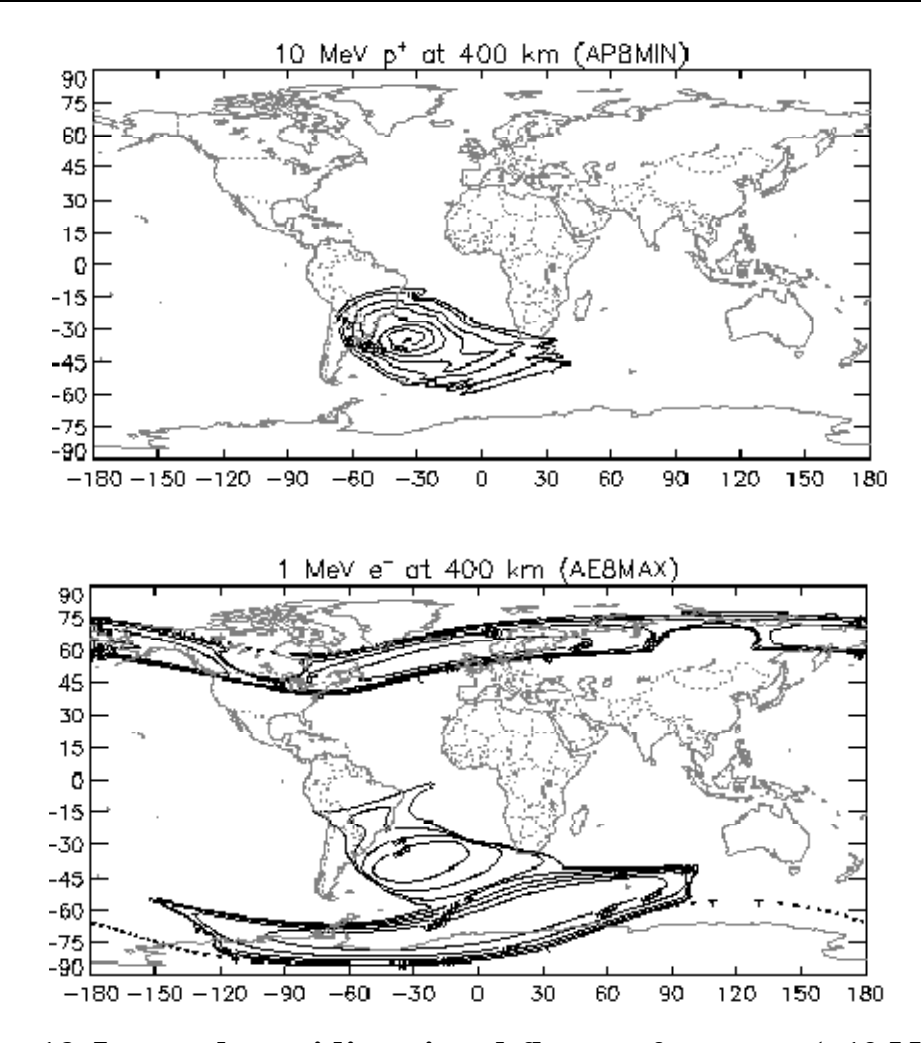
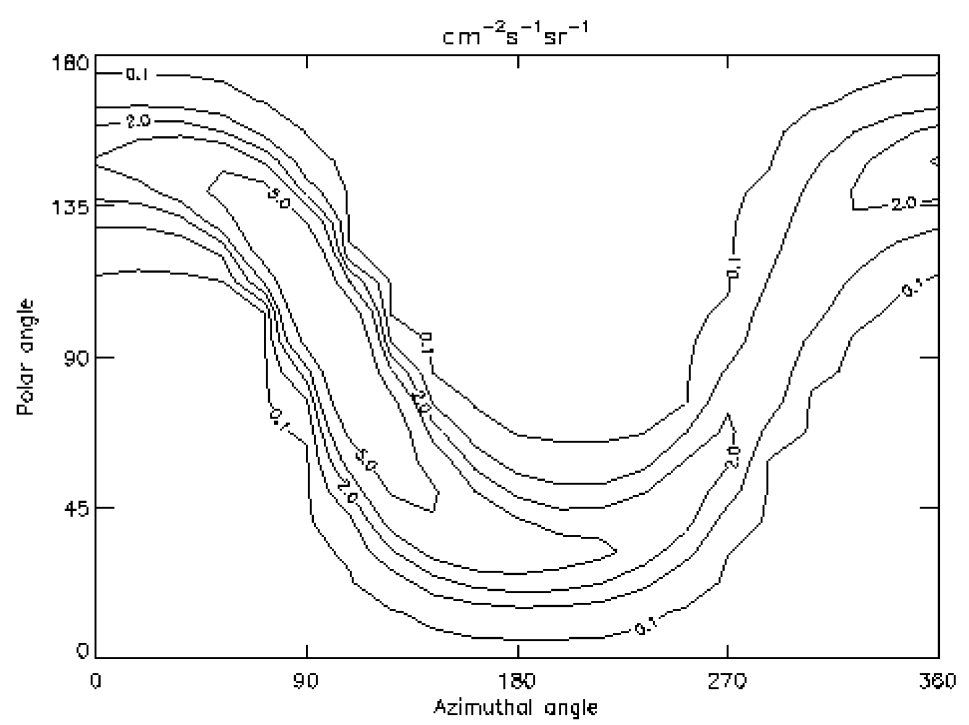


Figure 16: Integral omnidirectional fluxes of protons (>10 MeV) and electrons (>1 MeV) at 400 km altitude showing the inner radiation belt's "South Atlantic anomaly" and, in the case of electrons, the outer radiation belt encountered at high latitudes





Polar and azimuthal angles are with respect to Zenith and North respectively. (Therefore the horizontal plane has polar angle 90° , and westward viewing has azimuthal angle 90° .)

Figure 17: The flux anisotropy in low Earth orbit averaged over an orbit of the space station for protons >100 MeV energy



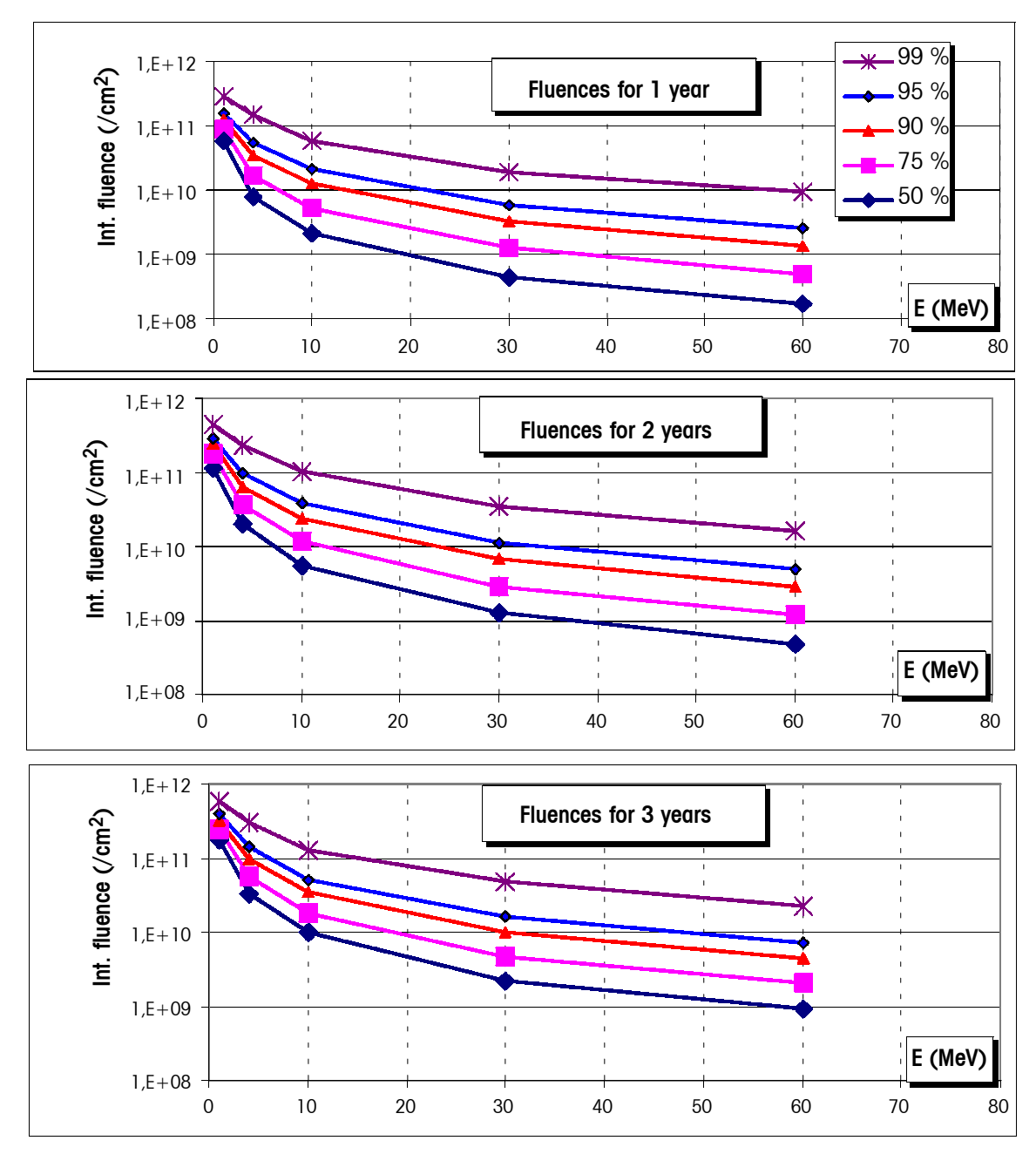


Figure 18: Solar proton fluence spectra for various statistical confidence levels (99 %, 95 %, 90 %, 75 % and 50 %, from top to bottom in each panel) for various mission durations (data from JPL-1991 Model)



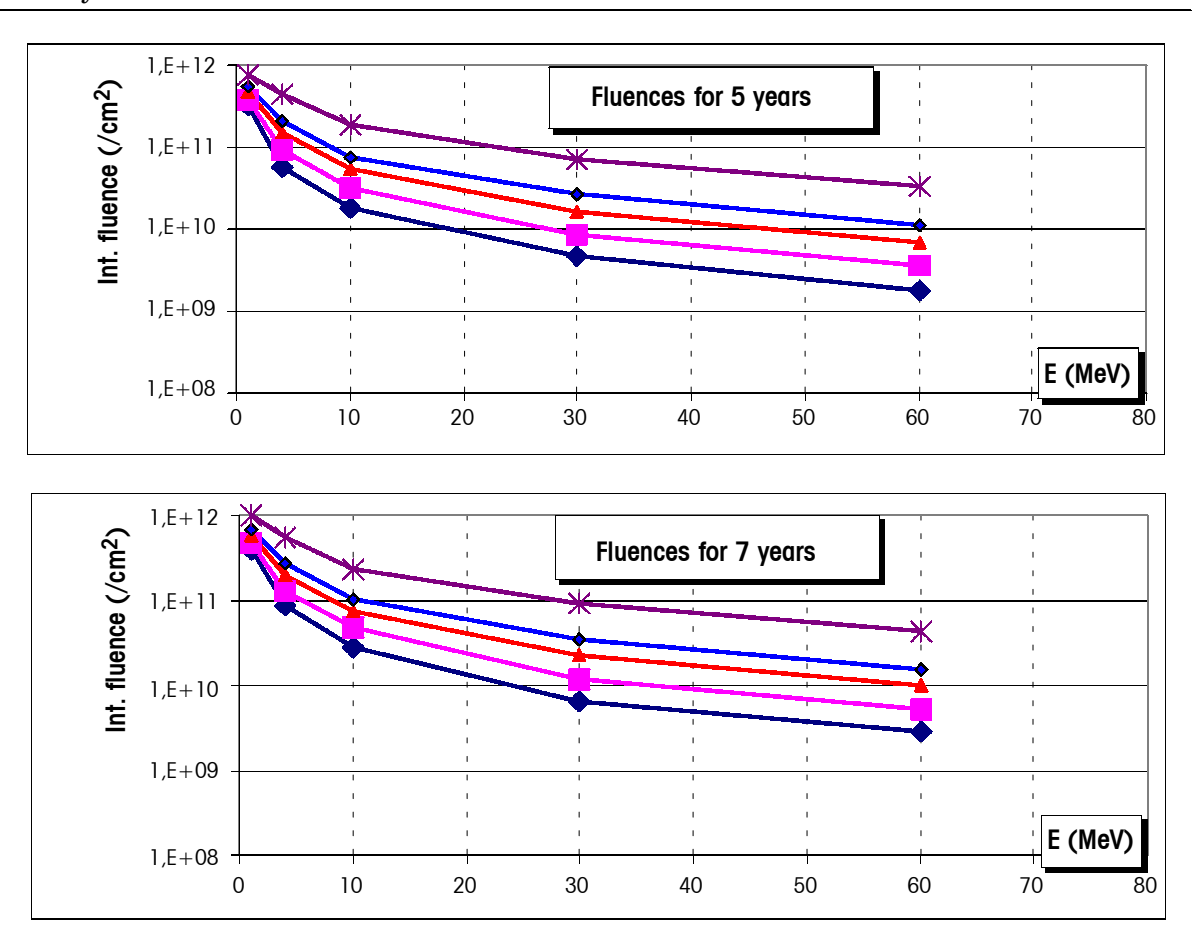


Figure 18: Solar proton fluence spectra for various statistical confidence levels (99 %, 95 %, 90 %, 75 % and 50 %, from top to bottom in each panel) for various mission durations (data from JPL-1991 Model) (continued)